
Multi-decadal climatology of Polar Lows over the North Pacific
by regional climate model

Dissertation zur Erlangung des Doktorgrades der Naturwissenschaften im Fachbereich
Geowissenschaften der Universität Hamburg

vorgelegt von

Fei Chen

Aus

Hanzhong China

Hamburg

2013

Als-Dissertation angenommen vom Fachbereich Geowissenschaften der Universität Hamburg

Auf Grund der Gutachten von Prof. Dr. Dr. h.c. Hans von Storch

und Dr. Matthias Zahn

Hamburg, den 21.11.2012

(Sprecher des Fachbereichs Geowissenschaften)

Abstract

The North Pacific is an area where frequently sub-synoptic Polar Lows form in the cold season, especially over the Japan Sea, Bering Sea and Gulf of Alaska. So far, a multi-decadal climatology of such Polar Lows based on individual cases has not been assembled. Here, we consider for this task a dynamical downscaling method for constructing realistically the formation and life cycles during the past decades without exploiting sub-synoptic information in initial fields. A regional climate model is conditioned by large-scale information of NCEP re-analyses.

Firstly, we tested the approach by examining its skill in simulating ten known cases of North Pacific Polar Lows. Three of these are discussed in some detail. The signatures of all storms emerge in the simulations with additional sub-synoptic details. The tracks of the simulated Polar Lows follow closely the tracks derived from satellite imagery. We conclude that the suggested method is suitable for constructing multi-decade climatologies, including trends and variability, of Polar Lows in the North Pacific by dynamically downscaling NCEP re-analyses.

Secondly, the 6-hourly 1948-2010 NCEP 1 re-analyses have been dynamically downscaled for the region of the North Pacific. With a detecting-and-tracking algorithm a climatology of North Pacific Polar Lows has been constructed. This derived climatology is consistent with the limited observational evidence in terms of frequency and spatial distribution. The climatology exhibits strong year-to-year variability but weak decadal variability and a small positive trend. A Canonical Correlation Analysis describes the conditioning of the formation of Polar Lows by characteristic seasonal mean flow regimes, which favor, or limit, cold air outbreaks and upper air troughs. Associated Correlation Pattern is introduced to describe the relationship between time series of Polar Low occurrence and the geo-potential height from sea level to the upper troposphere and the lower stratosphere. The results indicate that the relationship between the atmosphere circulation and Polar Low occurrence is mostly barotropic. Similar analysis is applied for the sea surface temperature. We conclude that the formation of anomalous SST as well as the formation of more, or less Polar Lows are steered by the same large-scale atmospheric circulation patterns. Two major patterns of Polar Low occurrence are related with the variations described by the large-scale climate change indices of PDO, PNA and, to a lesser extent, ENSO.

Thirdly, global climate model products for three different scenarios from IPCC are introduced to investigate the possibility of Polar Low trend over next century. With more greenhouse gas emission, global warming and the air temperature rising, the Polar Low frequency shows a decreasing trend. With sea ice melting, the distribution of Polar Low cyclo-genesis shows a northward shift.



Contents

List of Abbreviation.....	VII
List of Figures.....	VIII
List of Tables.....	XIV
Chapter 1 Introduction.....	1
1.1 Definition of Polar Low	2
1.2 Climatology background of North Pacific	3
1.3 Main achievements of Polar Low study over North Pacific	6
1.4 Research Plan.....	7
Chapter 2 Data and methods	9
2.1 Data Introduction.....	9
2.2 General information on the regional climate model	12
2.3 Downscaling method	14
2.4 Spectral nudging	16
2.5 Detection and Tracking algorithm.....	17
2.6 Empirical Orthogonal Functions	20
2.7 Canonical Correlation Analysis	21
2.8 Associate Correlation Pattern	23
Chapter 3 Case Studies.....	25
3.1 Validation of case simulations	26
3.2 A Case from Bering Sea.....	29

3.3	A Case from Gulf of Alaska.....	35
3.4	A Case from Japan Sea.....	40
3.5	Conclusion	45
Chapter 4	Multi-decadal Climatology.....	47
4.1	General Characteristic of Climatology	48
4.2	EOF analysis of mean sea level pressure field.....	56
4.3	Linkage of Polar Low distribution with large-scale sea level pressure pattern	59
4.4	Linkage of Polar Low occurrence with upper layer and sea surface	65
4.5	Long term correlation analysis.....	67
4.5.1	Pacific Decadal Oscillation	67
4.5.2	Pacific – North American tele-connection.....	69
4.5.3	El Niño-Southern Oscillation	71
4.5.4	Discussion.....	72
Chapter 5	Projection under different scenarios	77
5.1	General information of scenarios and data prepared.....	78
5.2	Simulation and tracking result	80
5.3	Conclusion	87
Chapter 6	Conclusion and outlook	89
	Acknowledgments.....	92
	Reference.....	93
	Erklärung.....	101

List of Abbreviation

ACP	Associated Correlation Pattern
CCA	Canonical Correspondence Analysis
COSMO-CLM	COntortium for SMOll scale Modelling in CLmate Model
ECHAM5/MPI-OM1	European Centre Hamburg Version 5/Max-Planck-Institute – Ocean Model Version 1
ENSO	El Niño/La Niña–Southern Oscillation
EOF	Empirical orthogonal functions
GMS 5	Geostationary Meteorological Satellite-5
IPCC	Intergovernmental Panel on Climate Change
NCEP/NCAR	National Centers for Atmospheric Prediction and National Center for Atmospheric Research
NOAA 5	National Oceanic and Atmospheric Administration National Environmental Satellite-5
PDO	Pacific Decadal Oscillation
PLS	Polar Low Season
PMSL	mean sea level pressure
PNA	Pacific/North American tele-connection pattern
SST	sea surface temperature
TBB	cloud-top temperature of equivalent blackbody data estimated from GMS-5 infrared data of the Japan Meteorological Agency

List of Figures

Figure 1.1 Mean wind field at the 500 hPa level during PLS over 1948/1949 – 2009/2010 from NCEP 1. (Unit: m/s)	4
Figure 1.2 Averaged PMSL field during PLS over 1948/1949 – 2009/2010 over the North Pacific from NCEP 1. (Unit: hPa).....	4
Figure 1.3 Mean surface temperature field during PLS averaged across 1948/1949 – 2009/2010 over the North Pacific from NCEP 1. Over the ocean, in case of no ice it indicates the SST, else it indicates the ice surface temperature. (Unit: K).....	5
Figure 2.1 Simulation area and model grid used for this study. Darker grid boxes at the border represent the sponge zone.	13
Figure 2.2 PMSL field from NCEP 1 at 06:00, 12:00, 18:00UTC 6 th and 00:00UTC 7 th March 1977. (Units: hPa) The red circles indicate the location where a Polar Low should be.	15
Figure 2.3 PMSL field of simulation output on 15:00UTC 22 th March 1975. The red circle indicates the location Polar Low should be. (Units: hPa).....	18
Figure 2.4 Filtered PMSL field on 15:00 22 th March 1975. (Units: hPa) The red circle indicates the location where the low should be.	18
Figure 3.1 The traces of all the 9 detected Polar Lows. The black points represent the locations where the Polar Lows were first detected and recorded.....	29
Figure 3.2 NOAA-5 infrared satellite image at 09:58UTC 7 th March 1977 (taken from (Bresch et al. 1997)); “P” marks the cloud pattern of the Polar Low in COSMO-CLM simulation and “D” is the Polar Low described by Bresch et al., (1997).....	30
Figure 3.3 PMSL of COSMO-CLM simulation results from 06:00UTC 6 th to 10:00UTC 7 th March 1977, P represents the Polar Low, S represents the synoptic low and D represents the Polar Low in Bresch et al. (1997). Left column: maps for 06:00, 12:00 and 18:00UTC on 6 th March 1977; right column: 23:00UTC in 6 th March, 04:00 and 10:00UTC on 7 th March 1977. The satellite image in Figure 3.2 corresponds to the phase at the bottom map on the right. (Units: hPa).....	31
Figure 3.4 Filtered PMSL field from the same date of Figure 3.3.....	32
Figure 3.5 The result of tracking algorithm from 06:00UTC 6 th to 00:00UTC 8 th March 1977.....	32

Figure 3.6 2 hourly filtered PMSL field from 10:00UTC to 20:00UTC 7th March 1977, P represents the Polar Low, S represents the synoptic low and D represents the Polar Low in Bresch et al. (1997). The satellite image in Figure 3.2 corresponds to the phase at the top map on the left. (Units: hPa) 33

Figure 3.7 PMSL as described by NCEP 1 re-analysis with a 1.875° grid resolution interpolated for 10:00UTC 7th Mar 1977, when a Polar Low formed west of the Kamchatka Peninsula. P represents the Polar Low we studied, S represents the synoptic low and D represents a Polar Low discussed by Bresch et al. (1997). 35

Figure 3.8 NOAA-4 infrared satellite image at 20:21UTC on 22th March 1975, P represents the Polar Low (Businger 1987). 36

Figure 3.9 PMSL of COSMO-CLM simulation result for the Polar Low on 22th March 1975 in the Gulf of Alaska. The results were presented by every two hours from 00:00 to 22:00UTC. Figure 3.8 shows the corresponding satellite image for the bottom third map. (Units: hPa) 36

Figure 3.10 Wind speed field of COSMO-CLM simulation result for the Polar Low on 22th March 1975 in the Gulf of Alaska. The results were presented by every two hours from 00:00 to 22:00UTC 22th March 1975. Figure 3.8 shows the corresponding satellite image for the bottom third map. (Units: m/s)..... 37

Figure 3.11 Filtered PMSL field of COSMO-CLM from the same date of Figure 3.9. 38

Figure 3.12 The result of adapted tracking algorithm from 00:00 to 22:00UTC 22th March 1975. 39

Figure 3.13 PMSL fields of NCEP 1 re-analysis data on 00:00, 06:00, 12:00 and 18:00UTC 22th March 1975. (Units: hPa)The black circles represent the location of the Polar Low..... 40

Figure 3.14 Two-hourly GMS-5 TBB satellite image from 06:00 to 16:00UTC 21th Jan 1997, P marks the Polar Low (Fu et al. 2004a). 42

Figure 3.15 Mean sea level pressure of COSMO-CLM simulation results for the Polar Low on 21th January 1997 in Japan Sea. The results were presented by every two hours from 00:00 to 22:00UTC 21th January 1997. (Units: hPa) 43

Figure 3.16 Filtered PMSL field of COSMO-CLM from same date of Figure 3.15. (Units: hPa) Red circles represent the location of the Polar Low..... 44

Figure 3.17 The geo-potential height on the 500 hPa level of COSMO-CLM simulation result for the Polar Low on 21th January 1997 in the Japan Sea. The results were presented by every two hours from 00:00 to 22:00UTC. (Units: m) 45

Figure 4.1 Number of detected Polar Lows in the North Pacific per PLS. The detected number of Polar Lows without N-S criterion (mark with ■). The solid line represents the trend from 1948/1949 to 2009/2010, which is 0.26 cases/PLS; the dashed line represents the trend from 1949/1950 to 2008/2009, which is 0.18 cases/PLS. The detected number of Polar Lows with N-S criterion (mark with ○). The solid line represents the trend from 1948/1949 to 2009/2010, which is 0.21 cases/PLS; the dashed line represents the trend from 1949/1950 to 2008/2009, which is 0.16 cases/PLS.48

Figure 4.2 Mean number of detected Polar Lows per month for the whole 62 PLSs. Error bars represent the inter-annual variability of Polar Low numbers.50

Figure 4.3 Histogram of the number of days per month on which Polar Lows were observed over the Gulf of Alaska or the Bering Sea during the period 1975-1983. White bar represents the result from our simulation and black bar represents results observed in satellite imagery (Businger, 1987).51

Figure 4.4 Histogram of the duration for all the Polar Lows detected in the tracking result for the 62 PLSs.52

Figure 4.5 a) Polar Low frequency distribution. Unit: detected Polar Lows per 0.4° grid box. b) Sub-regions, for which the numbers of detected Polar Lows were aggregated (R1-R12) and respective number of detected Polar Lows (see text). Also given for each sub-region are mean number of Polar Lows per PLS (Mean), standard deviation (Std dev) and Polar Lows per area unit (Weighted mean). The latter number is divided by the sea grid points of corresponding sub-region.53

Figure 4.6 Time series of area weighted mean Polar Low number for sub-regions. a) presents R1, R3, R4 and R9; b) presents R6, R7, R10, R11 and R12. The weighted mean values are calculated by the detected number of Polar Lows divided by the sea grid points of corresponding sub-regions.54

Figure 4.7 Time series of detected Polar Low numbers and the corresponding trend for the three different sub-regions with the highest frequency of Polar Low cyclo-genesis. Red represents the Gulf of Alaska (R3); Blue represents the band at southwest of Bering Sea (R4) and Green represents the east of Japan Island (R9). The solid lines represent the detected Polar Low number and the dashed represent the corresponding trend.55

Figure 4.8 PMSL field of special PLS a) 1948-1949 and b) 2009-2010.56

Figure 4.9 PMLS anomaly field of special PLS a) 1948-1949 and b) 2009-2010.57

Figure 4.10 The first 5 EOF patterns of the PMSL field and the corresponding time coefficient over

62 PLSs. Red lines indicate the corresponding PLS of maximum time coefficient, blue lines indicate the minimum PLS.58

Figure 4.11 Reconstructed PMSL anomaly field of special PLS a) 1948-1949 and b) 2009-2010. ...59

Figure 4.12 First 2 Canonical coefficient time series (a and b, dashed lines represent the Polar Low occurrences and the solid lines represent the PMSL pattern) and corresponding correlation patterns between regional time series of Polar Low occurrences per PLS in sub-regions R1-R12 (Δ for positive values, ∇ for negative values) and mean sea level pressure fields in Pa. The first CCA pair (Figure 4a and 4c) shares a correlation coefficient of 0.89. The second CCA pair (Figure 4b and 4d) shares a correlation of 0.72.61

Figure 4.13 Result of multiple regression analysis of number of Polar Lows in sub-regions R1-12, as given in Figure 4.5b, and of time coefficient series of mean sea level pressure pattern of the first two pattern of CCA result (Figure 4.12a,b).63

Figure 4.14 Orthogonal rotations of CCA1 and CCA2 (see Figure 4.12). a) $x=0^\circ$, b) $x=30^\circ$, c) $x=60^\circ$, d) $x=90^\circ$, e) $x=120^\circ$, f) $x=150^\circ$, g) $x=180^\circ$64

Figure 4.15 Associated Correlation Pattern between time series of geo-potential height over 62 PLS and time coefficient of the Polar Low occurrence from the first two CCA patterns (1st CCA pair, left column, 2nd right column). From top to bottom 100, 300, 500, 700, 850 and 1000 hPa. All variables are averaged across a PLS, i.e., from October to April.66

Figure 4.16 Associated Correlation Pattern between time series of ocean surface temperature over 62 PLS and time coefficient of the Polar Low occurrence from the first two CCA patterns (1st CCA pair, left column, 2nd right column). All variables are averaged across a PLS, i.e., from October to April. The surface temperature was taken from the NCEP 1 re-analysis data, over the ocean. In case of no ice it indicates the SST, else it indicates the ice surface temperature.67

Figure 4.17 The anomaly of typical wintertime sea surface temperature (SST) (colors), sea level pressure (contours) and surface windstress (arrows) during the warm and cool phases of PDO. (Mantua 2000)68

Figure 4.18 Time series of PDO index. a) monthly PDO index from 1948 to 2010 by Mantua(2000), solid line represents the yearly mean PDO index, blue and red bars represent the monthly PDO index, blue for negative and red for positive; b) corresponding PDO index in every PLS.69

Figure 4.19 Time series of PNA index. a) normalized monthly PNA index from 1948 to 2010 (Wallace and Gutzler 1981), solid line represents the yearly mean PNA index, blue and red

bars represent the monthly PNA index, blue for negative and red for positive; b) corresponding PNA index in every PLS. 70

Figure 4.20 Time series of ENSO index. a) normalized ENSO index from 1950 to 2010 (ENSO: Multivariate ENSO Index, see <http://www.esrl.noaa.gov/psd//people/klaus.wolter/MEI/table.html>), solid line represents the yearly mean MEI, blue and red bars represent the monthly MEI, blue for negative and red for positive b) corresponding MEI index in every PLS 72

Figure 4.21 Time series of normalized detected Polar Low number (black line), PDO index (red, with mark o), PNA index (blue, dash) and ENSO index (green, with mark *) 73

Figure 4.22 Result of multiple regression analysis of number of Polar Low sub-regions R1-12, as given in Figure 3b, and of PLS-time mean circulation indices PDO, PNA and ENSO. 74

Figure 4.23 The original time series of detected Polar Low numbers (shown in solid lines) and reconstructed time series of Polar Low frequency from multiple regression results of PLS-time mean circulation indices PDO, PNA and ENSO (shown in dashed lines) in two sub-regions, top: R1, and bottom: R3. 75

Figure 5.1 Scheme of the storylines for the four scenarios (Nakicenovic et al. 2000). 78

Figure 5.2 Anthropogenic emissions of CO₂, CH₄, N₂O and sulphur dioxide for the six illustrative SRES scenarios (Nakicenovic et al. 2000). 80

Figure 5.3 Number of Detected Polar Lows per PLS from 2001/2002 to 2099/2100 under the scenario of A1B. 1 – 3 indicate the numbers of realization experiments. 81

Figure 5.4 a) Polar Low frequency distribution under A1B_1. Unit: detected Polar Lows per 0.4° grid box. b) Sub-regions, for which the numbers of detected Polar Lows were aggregated (R1-R12) and respective number of detected Polar Lows (see text). Also given for each region are mean number of Polar Lows per PLS (Mean), standard deviation (Std dev) and Polar Lows per area unit (Weighted mean). The latter number is divided by the sea grid points of corresponding sub-region. 82

Figure 5.5 Mean proportion of ice covered time over the North Pacific Ocean during the PLS for different time periods, 1951-1959 and 1991-1999 are calculated from the ECHAM5/MPI-OM1 of 20C_1; 2001-2009, 2031-2039, 2061-2069 and 2091-2099 are calculated from the ECHAM5/MPI-OM1 of A1B_1. To be brief, the number of year represents the first half year of the PLS, for example: 1951 represents the PLS 1951/1952. 84

Figure 5.6 Time series of grid point number fulfilling the third Polar Low criterion during

1948/1949 – 1999/2000 from 20C, 2001/2002 – 2009/2100 from A1B, dashed lines with corresponding color represent the trend. Blue dashed line represents the trend during 1948/1949 – 2009/2010, black dashed line represents the trend during 2001/2002 – 2099/2100.....85

Figure 5.7 Number of Detected Polar Lows from 2001/2002 to 2099/2100. Black line represents the scenario of A1B_1, Blue line represents the scenario of A2_1 and red line represents the scenario of B1_1, dashed lines with corresponding color represent the overall trends.....86

List of Tables

Table 3.1 Examined cases of Polar Low formation. The asterisk * marks the 3 cases, which are discussed in detail. The characters “Observation” represent the data from literature, “NCEP 1” is the data at the corresponding time when there maximum wind speed and minimum central pressure exist in regional simulation. “Simulation” is the data from COSMO-CLM.	26
Table 4.1 Result of Mann-Kendall trend test for the time series of detected Polar Low number over 62 PLSs.	49
Table 4.2 The single variance and accumulated variance of the first 5 mode EOF results.	59
Table 4.3 Result of multiple regression analysis of first two time series of PMSL-patterns from the CCA results, and of PLS-time mean circulation indices PDO, PNA and ENSO.	75
Table 5.1 Mean value, standard deviation and overall trend of detected number of Polar Lows under the three realizations of A1B.	81
Table 5.2 Detected number of Polar Lows, corresponding proportion in the sub-regions of highest Polar Low density, overall and weighted mean trend during 2001/2002-2099/2100 (R1, R4, R8, R9 and R11) for the first and last 20 PLSs under A1B_1. PL represents the detected number, % represents the proportion. The weighted mean trend value is the trend for the sub-region divided by the corresponding number of sea grid points.	83
Table 5.3 Mean value, standard deviation and overall trend of detected number of Polar Lows under the three different scenarios A1B_1, A2_1 and B1_1.	86

Chapter 1

Introduction

During winter in the polar region, cold air builds up to create a polar front, where cold air coming from north and warm air from south meet. Small cyclones named Polar Lows form in the cold air north of the polar front, they are associated with wind speeds near or above gale force (Rasmussen and Turner 2003).

Legends and stories about Polar Lows have been passed from generation to generation from the seafarers in the north Atlantic and Arctic oceans. Fierce storm represents dangerous weather and often disasters for the ancient shipping business and oversea activities. The accompanied strong winds are hard to shelter on the sea. The unpredictable and short-lived cyclones are the most frighten assailant for the navigation around the polar region, thousands ships disappeared without trace under this threat (Rasmussen and Turner 2003).

The characteristic of this unpredictable extreme weather phenomenon have mostly been studied in individual cases. Some climatology studies have been carried out by satellite imagery for a short period of a few years. The long term characteristic of Polar Lows over the North Pacific is still unclear.

In the last century, industrialization and greenhouse gas emission made a great influence to the global climate change. It is a great challenge to investigate the long term trend of Polar Lows over the North Pacific before the background of climate change. The linkage between the variability of Polar Low and the climate change is a great help to understand how the large atmosphere condition feedback to this meso-scale weather phenomenon. This issue is becoming more and more significant to the society. The large scale climate pattern such as El Niño/La Niña-Southern Oscillation (ENSO), Pacific–North American tele-connection pattern (PNA) or Pacific Decadal Oscillation (PDO) may also have a close relationship with the formation of Polar Lows over the North Pacific, but the linkages between them are still uncertain. The investigation of multi-decadal variability of Polar Lows in the last century is a great help to understand how the Polar Low form under the large scale atmosphere circulation.

The aim of the following thesis is to assess the multi-decadal climatology of Polar Lows over the North Pacific by numerical simulation and further data analysis technique. The simulation, tracking result, multi-decadal variability of Polar Lows over the North Pacific and the mechanism of Polar Low cyclo-genesis over the region will be discussed in detail to support our work. Diverse technologies both on numerical simulation and data analysis have been employed in this work. Different data from simulation and observation have also been applied to compare and verify the result and conclusion.

1.1 Definition of Polar Low

“Polar Low” has been defined as the generic term for all meso-scale cyclonic vortices pole-ward of main polar front. It should be used for intense maritime meso-cyclones with scales up to 1000km with strong wind speed (Heinemann and Claud 1997). As the definition of intense sub-synoptic-scale cyclones, Polar Lows occur over sub-polar oceans during the cold season. They form in cold air masses pole-ward of the polar front. These cyclones go along with strong winds. Therefore they constitute a significant risk for shipping and offshore activities. Polar Lows have a relatively short life cycle (usually less than 2 days) and spatial scales of 200-1000km, which is smaller than the scales of the baroclinic “polar front” lows (Lystad 1986).

Since the Polar Lows were identified by Harley in the Norwegian Sea (1960), several theories have been used to explain Polar Low development during the past decades, such as: baroclinic instability, barotropic instability, Conditional Instability of the Second Kind (CISK) or Wind Induced Surface Heat Exchange (WISHE) instability (Forbes and Lottes 1985; Bond and Shapiro 1991; Kolstad 2006; Kolstad et al. 2009; Wu and Petty 2010). We take a brief view here on these theories.

The baroclinic instability is the first theoretical assumption to explain the formation of Polar Low by Mansfield (1974). By simulating Polar Lows in a baroclinicity model and comparing the result with observation, he indicated that the unstable wavelength which produced by the shallow baroclinic zone is close to the reality. Reed also supported the baroclinic theory in 1979, but he did not reject the possibility of other instabilities for the Polar Low mechanism (1979). Using the first satellite observation of Polar Low over the Norwegian Sea, Shapiro et al. investigate the development of Polar Low response to the baroclinic forcing by an eastward propagating upper-level synoptic scale short wave (Shapiro et al. 1987).

The barotropic shear instability has also been put forward to explain the genesis of meso- β -scale Polar Lows over the Polar-airmass Convergence Zone of Japan Sea (Nagata 1993). The role of upper level disturbance and barotropic instability is also important for the formation and evolution of Polar Lows over the Labrador Sea (Rasmussen et al. 1996).

As Polar Lows always take place in the winter during cold air outbreaks, the latent heat release caused by a large difference of air-sea temperature is the main driving force. Rasmussen reconstructed this heat flux and unstable CISK-forced disturbance during Polar Low simulation in a quasi-geostrophic model (Rasmussen 1981).

The wind induced surface heat exchange (WISHE) instability theory has also been used to explain the cyclo-genesis of Polar Lows in recent studies. A theoretical balanced axisymmetric model has been applied to investigate the WISHE intensification mechanism in Polar Low development by Gray and Craig (1998). The surface heat and moisture fluxes have a close relationship with Polar Low formation.

Various case studies indicate that usually several mechanisms together lead to the formation of Polar Lows (Businger 1985; Nordeng 1986; Mailhot et al. 1996).

1.2 Climatology background of North Pacific

The North Pacific is one of the most important regions for global atmospheric circulation. The cyclo-genesis of Polar Lows over North Pacific has a close relationship with both the large-scale atmospheric system and ocean. A detailed investigation was done through the climatology background and Polar Low formation by Henderson before (Yarnal and Henderson 1989a, 1989b). In general, there is a semi-permanent trough located along the coast region of the Eurasian Continent and North Pacific in the winter season. It is mainly induced by the downstream effects of the westerlies and the baroclinic gradient which caused by the strong land-sea thermal difference in these regions (Reed 1979). Cold air from Siberia and the polar region has been brought over the relatively warm coastal regions by this trough. Furthermore, the cold flow and jet stream through the troposphere on the upper level transports the cold air to the open ocean. Baroclinicity and instability will be induced by the strong air-sea temperature difference. On the other hand, the warm ocean current and polar front also plays an important role to the vertical stability of the cold air mass on the thermodynamics gradient level. Therefore, the highest frequency of Polar Low cyclo-genesis should be located along the coast zone of the Eurasian Continent, around the warm ocean current and eastern Asian jet.

As we mentioned above, Polar Low is a climate phenomenon which is induced by the air-sea interaction. There is a close relationship between the formation of Polar Low and the air pressure (at mean sea level; PMSL) pattern, the sea surface temperature (SST) and the wind field in the North Pacific.

The mean 500 hPa level wind field is calculated from NCEP 1 re-analysis data (Figure 1.1). Since the Polar Low takes highest frequency cyclo-genesis in winter, we calculated the mean wind field from every October to next April as a standard Polar Low Season (PLS), and calculated the mean field through PLS 1948/1949 – 2009/2010. We found the North Pacific is dominated by a west-to-east wind on the upper level. It brings the cold air from the Eurasian continent, especially from the Siberia. The area around Japan Island and Bering Sea are the first ocean barriers for the cold flow. So in these regions should be those with the highest frequency for Polar Lows.

1.2 Climatology background of North Pacific

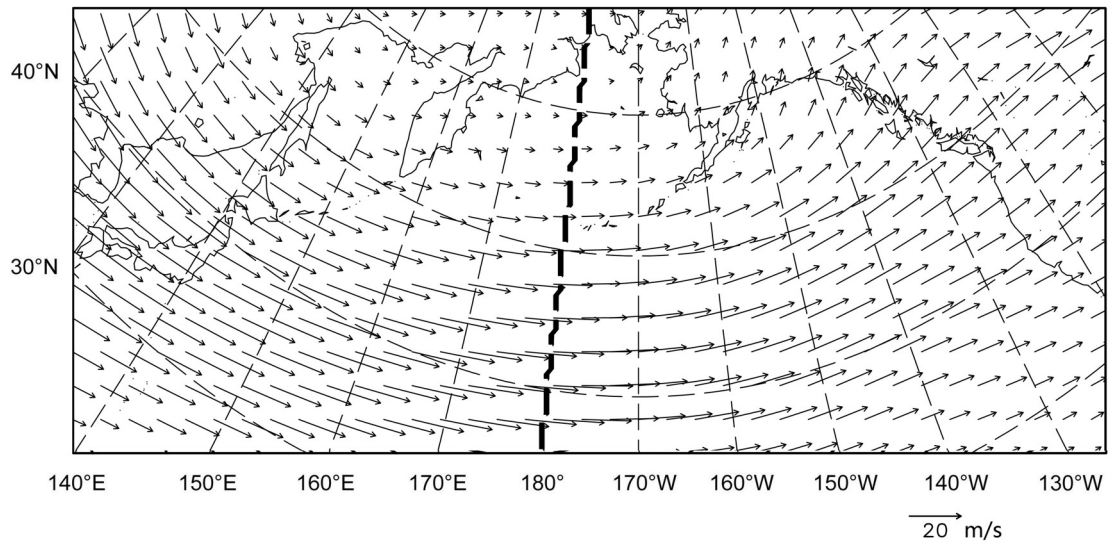


Figure 1.1 Mean wind field at the 500 hPa level during PLS over 1948/1949 – 2009/2010 from NCEP 1. (Unit: m/s)

Figure 1.2 shows the averaged PMSL field during last six decades. The climatology situation over the East Asian and North Pacific is obvious.

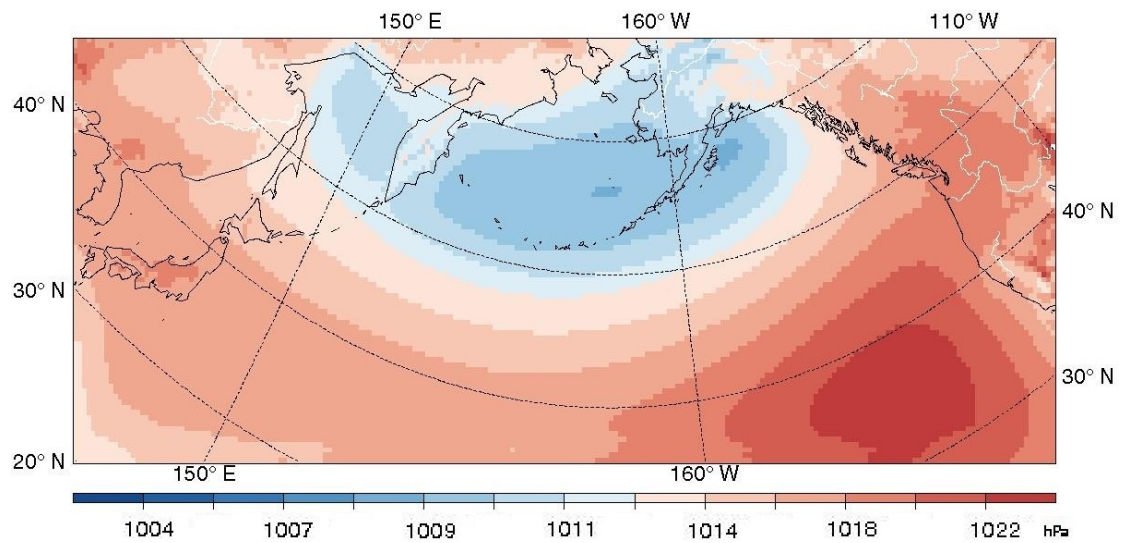


Figure 1.2 Averaged PMSL field during PLS over 1948/1949 – 2009/2010 over the North Pacific from NCEP 1. (Unit: hPa)

There existed a deep Aleutian Low over the Aleutian Islands. Most of the Bering Sea and part of Alaska have been controlled by this low system. The Eurasian Continent was characterized by a large area of

high pressure pattern, in which the Siberian High predominated over the polar region where cold flow emerges. The pressure gradient between the Aleutian Low and Siberian High was very strong, in which suggested the strong polar air outbreak. The strong pressure gradient just crosses the Japan Sea and the Northwestern Pacific, such as Bering Sea and the open ocean to the south of Kamchatka Peninsula.

The mean surface temperature was calculated from the NCEP 1 re-analysis data for the PLS (Figure 1.3). In case of no ice it indicates the SST, else it indicates the ice surface temperature. We have found that the SST around the Japan Island is relatively higher compared to the other marginal sea over 45°N. A high air-sea temperature difference would be expected when the cold flow outbreaks from the north, so one would expect a high frequency area of Polar Low cyclo-genesis around the Japan Island. The SST over the Sea of Okhotsk is low, partly it is covered by sea ice. As the air-sea temperature difference is not high enough to trigger Polar Low, the density of Polar Low formation there could be low. Therefore the air mass of the cold flow could be still cold enough after crossing the Sea of Okhotsk until it meets the higher SST region in the open ocean. Thus there should be a band of high frequency formation around the 45°N into the open North Pacific south of the Aleutian Islands, as the SST there is higher than the north part. It is the first thermal barrier for the cold flow from the north. Bering Sea and the Gulf of Alaska would get some polar lows, but not as much as the region around Japan Island.

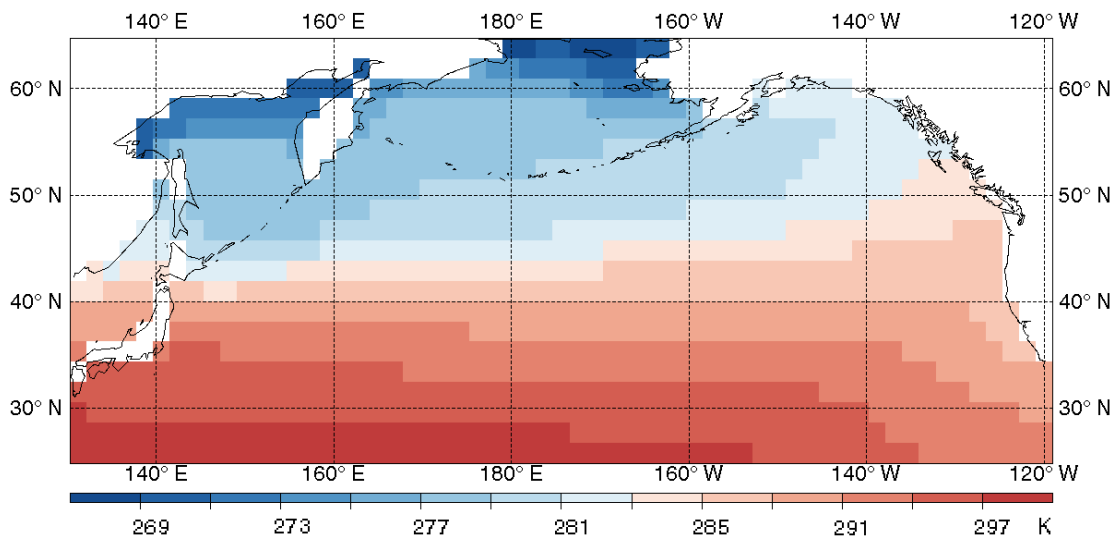


Figure 1.3 Mean surface temperature field during PLS averaged across 1948/1949 – 2009/2010 over the North Pacific from NCEP 1. Over the ocean, in case of no ice it indicates the SST, else it indicates the ice surface temperature. (Unit: K)

As we know in last section, Polar Low is a cyclone which is produced mostly by air-sea interaction. The

general information of wind field, upper level pressure field and sea surface and sea ice temperature indicate that the North Pacific is a region with the potential of a high Polar Low cyclo-genesis, especially in the southwest of Bering Sea, the Gulf of Alaska and the east of Japan Sea. This high air-sea temperature difference is related to warm waters in the south and cold air flow from the polar region in the north. We will prove this hypothesis by numerical simulation in the next step.

1.3 Main achievements of Polar Low study over North Pacific

The history of Polar Low research extends only over the last few decades. At the very beginning, observational data of Polar Low was very difficult to get, because of its relatively short life time and the high latitude occurrence in winter. The observation stations and ships are not sufficient neither on the temporal nor for the spatial scaled of such storms.

Since the advent of satellites, Polar Lows can be identified relatively easily, and short-term risk management can be performed. However, risk assessment is problematic since a homogeneous description of the formation and spatial distribution of such disturbances for multi-decadal time periods has not yet been achieved. Even if one could screen all satellite imagery, one would be left with very incomplete weather maps prior to the advent of satellite use. Indeed, North Pacific Polar Low studies have been limited to either specific cases or to statistics covering only a few years (Yarnal and Henderson 1989b; Fu et al. 2004a).

So far, a great part of the knowledge about Polar Lows is based on the analysis of satellite imagery. Polar Lows over the Northern North Pacific Ocean are characterized by a tight, spiral or comma cloud pattern; the comma cloud feature is dominant in the Bering Sea and Gulf of Alaska; both the spiral and comma patterns are found in the Japan Sea (Businger and Walter 1988; Douglas et al. 1991). A couple of authors have dealt with climatological issues of Polar Lows in the North Pacific (Businger 1987; Yarnal and Henderson 1989a). However the satellite observation based studies cover only a few years of Polar Low occurrences. Also, such efforts suffer from inhomogeneities due to the changing way of data recording and detection method, so that statements on trends and variability maybe are not robust.

Satellite-based climatologies have been derived for relatively short periods of time (Carleton 1985; Yarnal and Henderson 1989b). According to these studies, most Polar Low cyclo-genesis takes place in the western mid-latitude North Pacific, with a maximum of Polar Low cyclo-genesis located just off the east coast of Japan's northernmost island Hokkaido. The eastern North Pacific is less active with Polar Lows forming infrequently in the Gulf of Alaska. Since Polar Lows usually form in cold air masses moving from cold continents or ice-covered regions to open water, this pattern of formation reflects mostly the geographically different surface temperature conditions.

In a number of case studies, it was demonstrated that Polar Lows can be described by dynamical high-resolution models for the Japan Sea, see Yanase *et al.*, (Yanase et al. 2004; Yanase and Niino 2007); the Bering Sea see Bresch et al. (1997); the Gulf of Alaska see Businger (1987) and Blier (1996). In all cases the model results were consistent with satellite observations. Different from our approach, these studies make use of initial conditions describing the specific synoptic situation, within which the Polar Low forms, or first traces of the Polar Low itself. Consequently, these models are initiated right before the actual Polar Lows began to develop. Such studies allow hardly an assessment weather characteristics of Polar Lows are changing over time.

Polar Lows in the North Atlantic (Zahn and von Storch 2008a) as well as typhoons in East Asia (Feser and von Storch 2008) are two sub-synoptic phenomena, thus a methodology has been developed recently to construct a homogeneous data base for the formation and life cycles of such sub-synoptic disturbances. "Homogeneous" refers here to the property that changes in the data base are most likely reflecting changes in the physical reality and not changes in the observational-analytical process. Thus a homogeneous data base has the same error statistics in 1960 as in 2000, and no improvement would be implemented in the course of the analysis; the reason is, of course, that we want to attribute changes in the data base to changes in the physical system and not to unknown technical and procedural causes like changing density of observations or ever improving quality of instruments.

1.4 Research Plan

Data sets representing Polar Low formation and tracks, which are homogeneous, have high resolution and cover a long period do not exist. Thus sufficiently long and homogeneous time series for deriving the Polar Low climatology can only be generated by numerical simulation. A number of authors have applied global re-analysis data to investigate favorable, or unfavorable conditions of the formation of Polar Lows and meso-cyclones statistics in both Atlantic and Pacific (Condron et al. 2006; Kolstad 2006). Kolstad identified low static stability and reverse-wind shear conditions in the 40 years period of ERA-40 re-analyses as favorable conditions. A further work (Kolstad 2011) assessed the Polar Low information in coarse resolution datasets. He computed the climatological properties of favourable conditions for Polar Lows over the North Atlantic, the North-West Pacific and the Southern Hemisphere from a series of re-analysis products.

Here, we take the advantage of the dynamical downscaling methodology developed by Zahn and von Storch (2008b), for investigating the multi-decadal characteristic of Polar Lows over the North Pacific. This method is based on the observation that a standard multi-year re-analysis, such as NCEP 1 with a grid resolution of T62 (about 1.875°), is insufficiently describing sub-synoptic-scale phenomena like Polar Lows, but provide a homogeneous description of the large-scale flow conditions. The method consists of running a regional climate model (RCM) over the North Pacific Ocean, and dynamically downscale the NCEP 1 re-analysis data (Kalnay et al. 1996).

The thesis is structured as follows:

In the first chapter the background information of Polar Lows over North Pacific and the research plan is introduced.

All data and methods we applied for the study are presented in Chapter 2.

In order to demonstrate that the Zahn et al. (2008b) method performs well also in the North Pacific, it is necessary to verify the numerical simulation and data analysis technique before launching a multi-decadal simulation for studying the variability of annual statistics of Polar Lows in the Northern North Pacific. As a pre-work to identify the applicability of this downscaling technology, we run several cases to demonstrate that most of the individual cases of Polar Lows can be well reproduced (Chen et al. 2012). 10 cases are presented and 3 of them are discussed in detail in Chapter 3.

The continuously 63-years simulation result over the North Pacific is described and presented in Chapter 4. By making use of this downscaled simulation result and an automatic tracking algorithm (Zahn and von Storch 2008b), we have investigated the trend and variability of Polar Low occurrences in the North Pacific over last six decades. The linkage between Polar Low formation, and the atmospheric circulation, the variability of PMSL and SST is discussed next.

In Chapter 5 we study different climate scenarios for the future. The possible trend of Polar Low frequency and the spatial distribution over North Pacific under the global warming and greenhouse gas emission is discussed.

The conclusion and outlook is given in the last chapter.

Chapter 2

Data and methods

In order to produce a continuous simulation result for multi-decadal climatology study of Polar Lows, a regional climate model, forcing data and corresponding methodology is needed. The data sets we applied in the study are described in section 2.1; the used model and setup in section 2.2; the dynamical downscaling method in section 2.3; the spatial nudging technology which is used in the downscaling in section 2.4; the tracking algorithm used for automatically detecting and recording the formation of Polar Lows in section 2.5; a series of statistical methods in sections 2.6, 2.7 and 2.8.

2.1 Data Introduction

This study is based on simulations with a regional climate model dynamically downscaled from global data sets. For the hindcast climatology NCEP 1 is used. Simulations which describe the climate change under different scenarios in the future are made use to investigate the possible trend of Polar Lows over North Pacific in the next century. Various observational data from literature are used to compare and verify the results. Climate change indices are introduced to analysis the potential relationship between Polar Low cyclo-genesis and large-scale climate phenomena.

The general information of the data sets is presented below:

NCEP 1

The NCEP 1 re-analysis data is produced by the National Centers for Environmental Prediction and National Center for Atmospheric Research (NCEP/NCAR) with a spatial resolution of T62L28 (1.875°) and six hour temporal resolution (Kalnay et al. 1996). The period of this data set is from January 1948 to the present. We selected the data from 1948 to 2010 for our simulation. The data is produced with 17 pressure levels and 28 sigma levels.

We have applied these data for initial and lateral boundary values when running the regional climate model. The zonal and meridional wind component, air temperature, specific water vapor content, specific cloud water content, the surface specific humidity, skin temperature of ocean, thickness of surface snow amount and volume fraction of soil moisture are used to initialize the regional climate model. Following atmospheric and surface variables are provided as lateral boundary condition of

regional climate model: surface air pressure, air temperature, U and V component of wind and specific humidity. Skin temperature of ocean is used as lower boundary condition in case of sea points.

External data sets

The information about the lower boundary of the simulation domain is important for a regional climate model. The orography and orographic roughness length are provided by the gtopo30 (Moore et al. 1991), the land-sea fraction, parameters of vegetation, leaf area, root depth and lake fraction are provided by the Global ecosystems V2.0 (Champeaux et al. 2005). The soil type and the climatological deep soil temperature is provided by the Food and Agriculture Organization of the United Nations (FAO) (van Engelen and Wen 1995).

ECHAM5

The global climate model products for the climate change scenarios which used to force the regional climate model was produced for CMIP5 with the coupled GCM ECHAM5/MPI-OM1 (Roeckner et al. 2003) which refers the European Centre Hamburg Version 5/Max-Planck-Institute – Ocean Model Version 1. This model is designed by the Max-Planck-Institute for Meteorology. The atmospheric simulation results are produced with a spatial resolution of T63L31 (1.875°) and 6 hourly output. The number of vertical levels of the atmosphere model is 31 for hybrid sigma coordinate. More information on the atmospheric part, the ocean part and the coupling is available in the documentations (Roeckner et al. 2003; Marsland et al. 2003; Jungclaus et al. 2005).

Firstly Roeckner et al. performed 2655 years pre-industrial control run for the coupled model to spin up the atmosphere and ocean system and to have a measure for the model internal variability. Secondly there are three different realizations for the 20th century, namely 20C_1, 20C_2 and 20C_3. These three experiments of 20C were initialized at different years of the control run. Then realizations of A1B, A2 and B1 are initialized in year 2000 of the corresponding 20C realization. For example the A1B_1 is initialized in the year 2000 of 20C_1 (Roeckner et al. 2006a, 2006b, 2006c, 2006d, 2006e). A recent climate condition control run result 20C during 1948 – 2000 is also used for further discussion (Roeckner et al. 2006f). Various variables are presented in this global product, including the sea ice temperature, sea surface temperature, surface air pressure, surface snow amount, canopy water amount, sea ice fraction and surface temperature. The air temperature, U and V component of wind, specific humidity, mass fraction of cloud liquid water in air are given on the hybrid sigma model level.

We take the experiment result of A1B_1, A1B_2, A1B_3, A2_1 and B1_1 here to investigate the possibility of Polar Low trend during 2001-2100 over the North Pacific.

Observation data

In order to compare and verify the hindcast simulation result with reality, we introduced various observation data from literatures. The satellite observation is based on National Oceanic and

Atmospheric Administration National Environmental Satellite-5 (NOAA-5) visible satellite image, NOAA-4 infrared satellite image and cloud-top temperature of equivalent black body (TBB) data estimated from Geostationary Meteorological Satellite-5 (GMS-5) infrared data of the Japan Meteorological Agency (JM). Some data from ships, shore, island stations (Bresch et al. 1997) Rawinsonde soundings data for air temperature (Businger 1987) surface meteorological stations, Sapporo and Niigata radars and regional objective analysis (RANAL) data (Fu et al. 2004a) are also used.

Large-scale climate phenomenon indices

We have used three indices for investigation. They are the indices of the Pacific Decadal Oscillation (PDO), Pacific North America tele-connection (PNA) and El Niño Southern Oscillation (ENSO).

The **PDO** index is defined as the leading principal component of North Pacific monthly SST variability. Here we take the index from Joint Institute for the Study of the Atmosphere and Ocean (JISAO), University of Washington. They calculated it as the leading PC of monthly SST anomalies in the North Pacific Ocean, pole-ward of 20°N. By removing the monthly mean global average SST from the data, they separated the PDO pattern of variability from any “global warming” signal (Hare and Francis 1995; Mantua et al. 1997; Zhang et al. 1997). Additional information is given in section 4.5.1.

The **PNA** index is derived by

$$\text{PNA} = 0.25 * [Z(20\text{N},160\text{W}) - Z(45\text{N},165\text{W}) + Z(55\text{N},115\text{W}) - Z(30\text{N},85\text{W})]$$

The Z are standardized 500 hPa geo-potential height values. This formula is given by Wallace and Gutzler (1981) and the data is provided by JISAO, University of Washington. Additional information is given in section 4.5.2.

Here we take the Multivariate **ENSO** Index (MEI) to describe the ENSO variability in the last century. It was calculated by the Earth System Research Laboratory, NOAA. The MEI is performed from six main observed variables over the tropical Pacific. They are: sea-level pressure, zonal and meridional components of the surface wind, sea surface temperature, surface air temperature, and total cloudiness fraction of the sky. These observations have been collected and published in the International Comprehensive Ocean-Atmosphere Data Set (ICOADS) for many years. The MEI is computed separately for each of twelve sliding bi-monthly seasons (Dec/Jan, Jan/Feb,..., Nov/Dec) (Rasmusson and Carpenter 1982; Wolter and Timlin 2011). Here we are trying to relate the MEI to monthly value of ENSO index. We take Dec/Jan to represent the value of January. All the values of the other month follow this order. Additional information is given in section 4.5.3.

2.2 General information on the regional climate model

The regional climate model which we have applied here is the COSMO-CLM (Steppeler et al. 2003). The COSMO-CLM (COSMO model in CLimate Mode) is the climate version of the operational weather prediction model of the Deutscher Wetterdienst and the Consortium for Small scale MOdelling (COSMO), adapted to climate simulation purposes by the CLM-Community (<http://www.clm-community.eu>). This nonhydrostatic regional model is designed for numerical weather prediction and various scientific studies. The official version of this COSMO-CLM model is CCLM_4.8. The unified model version which we applied for this study is cosmo_4.8_clm11. The most important features of the model are presented below. A detailed description can be found on the official website (<http://www.cosmo-model.org>).

Dynamics: the model is based on the nonhydrostatic, full compressible hydro-thermodynamical equations. A subtraction is applied for the hydrostatic base state. The prognostic variables are horizontal and vertical Cartesian wind components, temperature, pressure perturbation, specific humidity, cloud ice content and specific cloud liquid water. The cloud ice content, turbulent kinetic energy, specific water content of rain, snow and graupel are optional. The total air density, precipitation fluxes of rain and snow are diagnostic variables. The equations are formulated in rotated geographical coordinates and a generalized terrain following height coordinate.

Numerics: the horizontal grid is Arakawa C-grid and with a Lorenz vertical grid staggering. The spatial discretization is done by the second-order finite differences. The default time-split integration scheme is the second-order leapfrog with explicit on horizontal and implicit on vertical. A 4th-order linear horizontal diffusion is applied for the numerical smoothing with an orographic limiter.

Initial and Boundary Conditions: interpolated data from coarse-grid driving models can be used.

Physical Parameterizations: the subgrid-scale turbulence is described by the prognostic turbulent kinetic energy closure including effects from subgrid-scale condensation and from thermal circulations. The 3D turbulence is calculated by the horizontal turbulent diffusion in the corresponding terrain following coordinates. The process of cloud water condensation and evaporation is adjusted by saturation. The precipitation is parameterized by a bulk microphysics in water vapour, cloud water, cloud ice, rain and snow with 3D transport for the precipitating phases. More parameterizations could be found in the documentation files of COSMO-CLM model.

Code and Parallelization: the standard Fortran constructs are used for the modular code. A gridline halo is applied for the horizontal domain decomposition in Leapfrog and Rung-Kutta scheme under different lines. The Message Passing Interface (MPI) is also used for parallelization on distributed

memory super computers.

There is a series of additional components required for the simulation process, such as interpolation of boundary conditions from the driving data and post-processing utilities.

COSMO-CLM has been widely used for climate studies not only over the European continent, Mediterranean Sea and Atlantic Coast (Rockel and Geyer 2008), but also for studying North Atlantic Polar Lows (Zahn and von Storch 2008a), East Asian typhoons (Feser and von Storch 2008) “Medicanes” in the Mediterranean Sea (Cavicchia and von Storch 2011), soil-vegetation-atmosphere transfer model in tropical Africa (Akkermans et al. 2012), summer monsoon in Indian (Dobler and Ahrens 2011), climate projections in Eastern Europe (Pavlik et al. 2012), mixed-phase clouds and precipitation in the Alps (Zubler et al. 2011) and precipitation in Europe and South Asia (Dobler and Ahrens 2008).

The model configuration is presented next, most of the namelist parameters are set to default of COSMO4.8, only the modified part is presented.

The domain and the model grid: The simulation region is shown in Figure 2.1. A rotated grid with 0.4° grid resolution and 220 and 80 points is employed for the longitudinal and latitudinal grid map. The 8 grids sponge zone is introduced to avoid reflection of waves at the boundaries. Boundary data is prescribed by this zone with decreasing influence for the inner grid points. The simulation results from the sponge zone are not usable for further analysis. The number of vertical levels is 40. The region includes the Bering Strait in the north, the winter low pressure system “Aleutian Low” with its great influence on the formation of Polar Lows, and the Japan Sea.

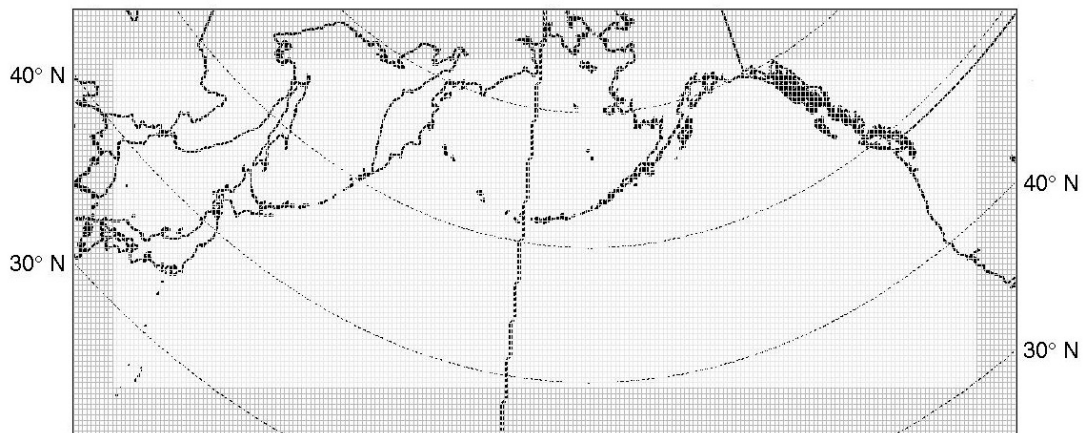


Figure 2.1 Simulation area and model grid used for this study. Darker grid boxes at the border represent the sponge zone.

Parameters for the model run: The time step is 200 seconds. We set the model in restart mode and

the duration of the hindcast is one month. The number of processors in the x-direction of grid is 8 and y-direction is 16.

All the parameters for **tuning dynamics and physics** are set as default.

Parameters for the numerical schemes to solve the thermodynamic model equations: The semi-implicit time-integration scheme is 10 dimension of Krylow space for elliptic solver. The spectral nudging is switched on (see section 2.4).

Parameters for the physical parameterizations: For the **radiation**, the time interval between two calls of the radiation scheme is 1 hour. The effective CO₂ parameterization (including CO₂, CH₄ and N₂O) is considered to choose a special CO₂-concentration for scenario simulation. For the mode of **vertical turbulent diffusion** parameterization, we used Neumann boundary conditions for heat and moisture transport at the lower boundary instead of Dirichlet boundary conditions. For the **surface layer fluxes** we selected the new TKE-based scheme including a laminar sub-layer, interpolated the 2 and 10 meter values based on profile relations used in the new scheme to diagnosis the synoptic station values. For **soil processes**, the multi-layer soil model TERRAL_ML is switched on. The number of soil layers is 10 and the depth of bottom of last hydrological active soil layer is 4 meter. The melting processes are included in this model. The soil freezing temperature is calculated dependent on the water content not. For subgrid-scale **moist convection**, as temperature, water vapour and horizontal wind parameterization is included.

The parameters **controlling the input**: they are used to control the initial and boundary data for the model. We applied NCEP 1 re-analysis product for the initial and lateral boundary condition. As the NCEP 1 re-analysis data is available every 6 hours, we set the interval between two consecutive boundary data to 6, which means the boundary values are interpolated linearly between 6 hours.

The parameters **controlling the output**: they are used to control the output. The variables of air temperature, U and V component of wind, specific humidity, mass fraction of cloud liquid water in air, the surface downward latent and sensible heat flux, the surface net shortwave and longwave radiation, are output on the 40 hybrid sigma model level. The variables of air pressure, U and V component of wind are outputted on the height-level 500, 1000, 1500, 2000, 2500, 3000, 3500, 4000, 4500 and 5000 meter. The geo-potential height, air temperature, U and V component of wind, specific humidity, specific cloud liquid water content, relative humidity are output on the pressure level of 100, 300, 500, 700, 850, 925 and 1000 hPa. The soil temperature and soil water content are output on the soil levels. The PMSL, surface temperature and 10 meter wind component are output on the corresponding level.

2.3 Downscaling method

As the observation of atmosphere is limited both in space and time, the description of long-term

trends suffers from in-homogeneities. In order to get a long term and horizontally highly resolved simulation which is close to the reality, a downscaling technique is employed. We downscale global re-analysis data to produce a homogeneous hindcast of Polar Low activity. By forcing the RCM, the large scale information of atmosphere which provided by the re-analysis are mostly reproduced by the RCM. Additionally meso-scale features are produced due to the high resolution (Rockel et al. 2008).

The downscaling method which employs on the statistically determined links is called statistical downscaling. On the other hand, a high resolution regional climate model can downscale global states in a dynamical way. We used the re-analysis for initial conditions and the lateral and lower boundary conditions. The dynamical downscaling is enforced by a spectral nudging, which is presented in 2.4.

Figure 2.2 shows the NCEP 1 re-analysis data of PMSL for a Polar Low forming over the Bering Sea. The red circles indicate the location where a Polar Low should be, but we found there is no Polar Low information in the re-analysis. Coarse resolution limits the analysis of Polar Lows using global re-analysis data. This case is discussed in detail in section 3.2.

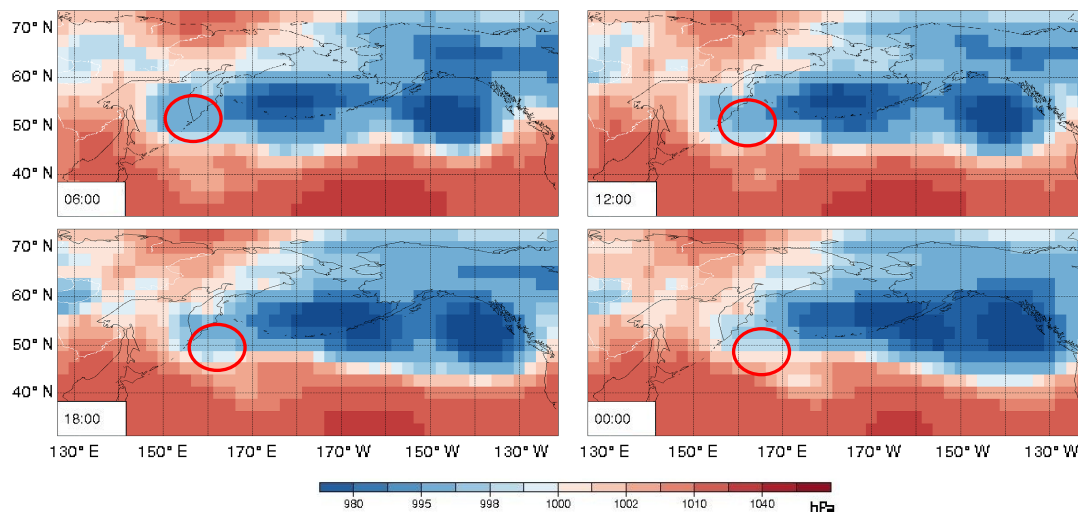


Figure 2.2 PMSL field from NCEP 1 at 06:00, 12:00, 18:00UTC 6th and 00:00UTC 7th March 1977. (Units: hPa)

The red circles indicate the location where a Polar Low should be.

It is shown in chapter 3 by test cases that the used methodology leads to good reproductions of Polar Low life cycle and their movement across the ocean. The model is initiated well in advance of the formation of the cyclones, so that the generation of the lows is not due to some seeds in the initial field, but dynamically induced by favorable large-scale conditions (which are enforced on the regional model by “large-scale nudging” (von Storch et al. 2000) towards the driving NCEP 1 re-analysis, is discussed in the next section 2.4). It turns out that the Polar Lows are realistically described by the regional model, with considerably more detail than in the driving NCEP 1 re-analysis.

2.4 Spectral nudging

Spectral nudging is a technique applied in regional climate models. The method stabilizes the large scale synoptic status for long time series simulation. By applying the spectral nudging method, the large-scale circulation of the regional climate model result follows the steering provided by the NCEP 1 re-analyses and develops additional, consistent small-scale features. The quality of this technique is verified by several experiments in a regional climate model (Feser 2006). It is indicated that the meso-scale variability is significantly improved by this technique. The spectral nudging was introduced by Waldron et al. (1996).

In our model and simulation, we use the large-scale spectral nudging technique introduced by von Storch et al. (2000). This technique constrains the development in the interior of the model domain. The spectral nudging is applied for the wind components at 850 hPa and above, with the nudging becoming stronger with height. It is limited to spatial scales larger than 800 km.

Here we do Fourier transform of the variable from the regional climate model COSMO-CLM for an example:

$$\psi(\lambda, \phi, t) = \sum_{j=-J, k=-K}^{J, K} \alpha_{j,k}^m(t) \exp(ij\lambda / L_\lambda) \exp(ik\phi / L_\phi) + \psi_{rest,m}(\lambda, \phi, t) \quad (2.1)$$

λ and ϕ are the zonal and meridional coordinates, j and k are corresponding wavenumbers on the zonal and meridional direction, index m indicates the regional climate model, J and K are the maximum zonal and meridional wavenumber to be nudged, α is the Fourier coefficient, L_λ and L_ϕ are the zonal and meridional extensions of the area, $\psi_{rest,m}$ is the unchanged part of the transformed field, t indicates time. By doing the same transform for global model (NCEP1 in our case), we have:

$$\psi(\lambda, \phi, t) = \sum_{j=-J, k=-K}^{J, K} \alpha_{j,k}^a(t) \exp(ij\lambda / L_\lambda) \exp(ik\phi / L_\phi) + \psi_{rest,a}(\lambda, \phi, t) \quad (2.2)$$

The index a indicates the variables from NCEP 1. So the nudging terms for the spectral interior domain should be:

$$\sum_{j=-J, k=-K}^{J, K} \eta [\alpha_{j,k}^a(t) - \alpha_{j,k}^m(t)] \exp(ij\lambda / L_\lambda) \exp(ik\phi / L_\phi) \quad (2.3)$$

Following von Storch et al. (2000) the parameter η is defined by:

$$\eta(p) = \alpha \left(1 - \frac{p}{850hPa}\right)^2 \quad (2.4)$$

The p represents the pressure level in the model above 850 hPa. The strength of nudging “ α ” is selected by 0.5 as the “alpha_sn” in the name list of COSMO-CLM, “J” is selected by 15 for “isc_sn” which represents the zonal wavenumber, and 5 for “K” indicates the meridional wavenumber as “jsc_sn”.

2.5 Detection and Tracking algorithm

It is a challenge to detect the location and time for the Polar Lows from complex and large output of the model simulation. We test if the detection and tracking-algorithm previously developed by Zahn and von Storch (2008b), for finding Polar Lows in the output of COSMO-CLM simulations also works for our region.

The objective detection-and-tracking procedure was applied to determine the presence and tracks of Polar Lows in the North Pacific. The detection procedure searches for the minimum in the band-pass filtered PMSL fields and concatenates the minimum in consecutive time steps to tracks.

A two dimensional digital band-pass filter is needed for the spatial analysis of the mean sea level pressure output field. The certain scale of wave has been filtered for the meteorological field. The Polar Low is a meso-scale cyclone with spatial scale up to 1000 km. A digital band-pass filtering retaining scales of 200-800 km is used (Feser and von Storch 2005).

Figure 2.3 shows a PMSL field on 15:00 22th March 1975 as an example. There a low forms over the Gulf of Alaska marked by a red circle. The low pressure system can be found around (163°W, 54.5°N).

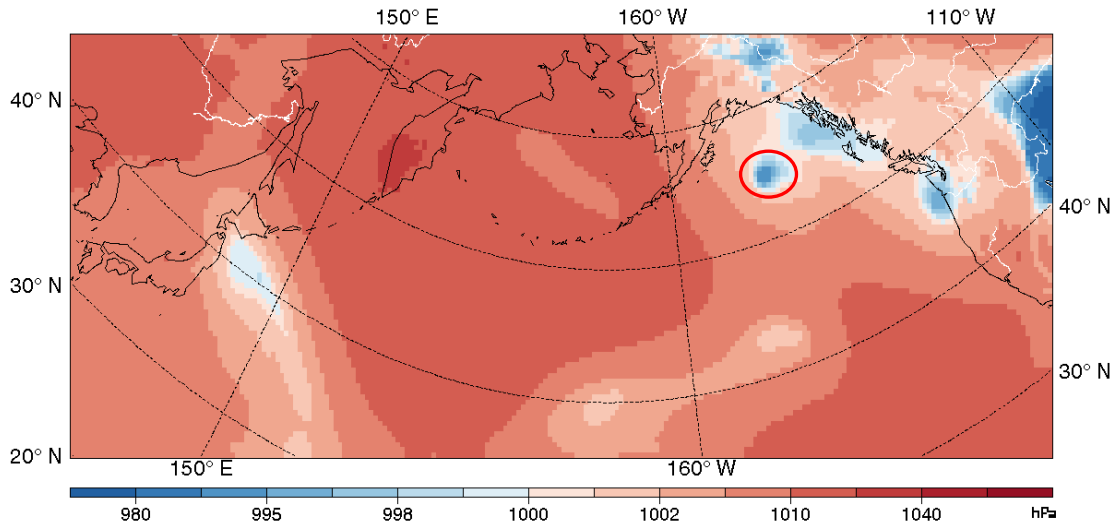


Figure 2.3 PMSL field of simulation output on 15:00UTC 22th March 1975. The red circle indicates the location Polar Low should be. (Units: hPa)

Figure 2.4 presents the filtered PMSL field at the same time. We found there is an obvious filtered minimum located at the same position on the filtered PMSL field where the low exists, marked by a red circle. By detecting the minimum in the filtered PMSL field, we got the location of a possible Polar Low at 15:00 22th Mar 1975.

Then we combine all detected positions time step by time step to get the track of the low. After this tracking we have to decide whether the low is a Polar Low.

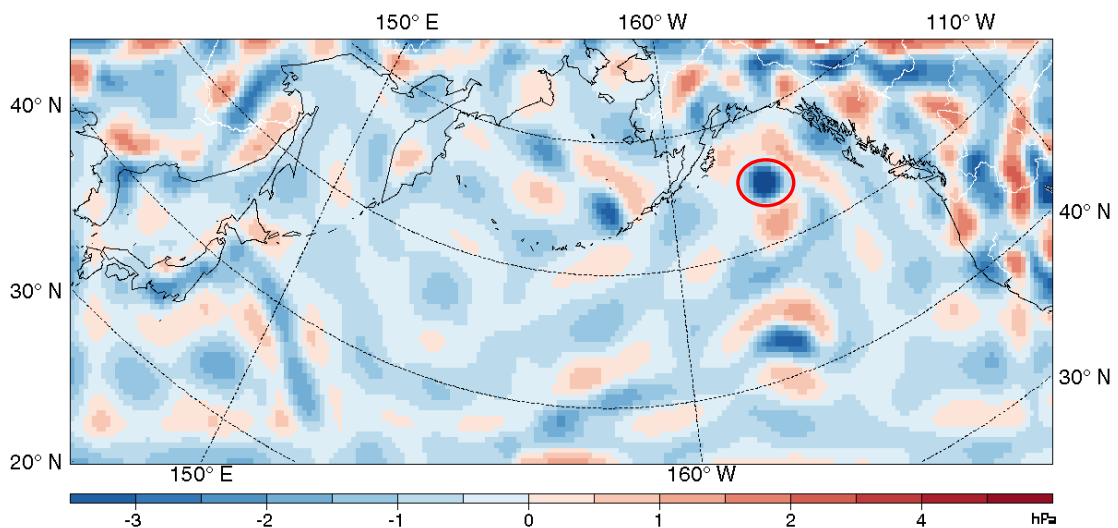


Figure 2.4 Filtered PMSL field on 15:00 22th March 1975. (Units: hPa) The red circle indicates the location where the low should be.

Along these tracks, the fulfillment of further criteria is requested for categorizing an event as Polar Low:

(1) strength of the minimum band-pass filtered PMSL: ≤ -2 hPa once along the track. As strong meso-scale disturbances, the Polar Lows should be retained for the stronger cyclones from the filtered PMSL field. So we exclude the tracks with their filtered minimum pressure do not fall below -2 hPa at least once.

(2) 10m height wind speed: ≥ 13.9 m/s once along the track. Strong wind is an obvious feature of a Polar Low. The surface wind speed should be near or above the gale force. By checking cases of Polar Low and comparison with observation, we set the threshold value for 13.9 m/s. The maximum 10 m wind speed in a distance of about 100 km around the detected positions along the track must exceed this value at least 20% along the track.

(3) air-sea temperature difference: $SST - T_{500 \text{ hPa}} \geq 39$ K. The background condition of Polar Lows cyclo-genesis is a convectively unstable atmosphere system. The lower level should be warmer than the upper level in terms of potential temperature. The Norwegian Meteorological Institute introduced the temperature difference between the sea surface temperature (SST) and the 500hPa to describe the vertical stability (Noer and Ovhd 2003). This value has been chosen by 39K according to more than 10 cases of Polar Lows simulation results over the North Pacific.

(4) direction of the track: a north-to-south component. The Polar Lows always forms with a cold air outbreak, the cold flow from the polar region usually takes a southward direction.

(5) no coastal points: the filtering program is influenced by the orography along the coastlines. In order to avoid falsely detected disturbances, tracks are excluded when over 50% of the positions are neighbors of land points.

When the minimum of the band-pass filtered PMSL along these tracks decreases below -6 hPa once, and there are no coastal grid boxes close to that location, a Polar Low is recorded irrespective of the other criteria.

This is mostly identical to the setting of Zahn and von Storch (2008b), but some parameters (like the air-sea temperature difference) have been modified in order to catch the Polar Lows more accurately in North Pacific (Chen et al. 2012). However, we used a cosine (DCT) band-pass filter of Denis et al. (Denis et al. 2002) instead of the digital filter used by Zahn et al., after Xia et al. (Xia et al. 2012) pointed out the superiority of the first one. The discrete cosine transforms (DCT) is more precise in scale separation than the original digital filter. It is more suited for the band-pass filtering of PMSL fields.

There are some North Pacific Polar Lows moving zonally, like the case from 22th March 1975 on the Gulf of Alaska (Chen et al. 2012, see section 3.3). Therefore Polar Low numbers are also determined without the “north-to-south direction” criterion. In doing so, more Polar Lows but also more synoptic cyclones would be included (see chapter 4).

2.6 Empirical Orthogonal Functions

The Empirical Orthogonal Function (EOF) analysis is a multivariate analysis technique applied for the separation of different dominant patterns of variability from a meteorological field. It was first described by Pearson in 1902 (Pearson 1902) and introduced into climate research by Lorenz (1956). Here we take the functions and theoretical analysis from the “Statistical Analysis in Climate research” (von Storch and Zwiers 1999).

Introduced by an m-dimensional random vector \vec{X} , which represents the meteorological field in a time series we are interested in, the \vec{X}_t stands for the value observed at time t. The anomalies are given by $\vec{X}'_t = \vec{X}_t - \hat{\vec{\mu}}$, with the mean field $\hat{\vec{\mu}}$.

By expanding the anomalies, a finite series is obtained as

$$\vec{X}'_t = \sum_{i=1}^k \hat{\alpha}_{i,t} \hat{e}^i_t \quad (2.5)$$

$\hat{\alpha}_{i,t}$ are the time coefficients and the \hat{e}^i_t stand for the fixed patterns. The patterns are chosen to be orthogonal so that optimal coefficients $\hat{\alpha}_{i,t}$ are obtained by simply projecting the anomalies \vec{X}'_t onto the patterns. The patterns can be specified further when the error

$$\sum_t (\vec{X}'_t - \sum_{i=1}^k \hat{\alpha}_{i,t} \hat{e}^i_t)^2 \quad (2.6)$$

is minimum. For brevity we assume $\vec{\mu} = 0$. We could find the first pattern \vec{e}^1 when

$$\epsilon_1 = \varepsilon(\|\vec{X} - \langle \vec{X}, \vec{e}^1 \rangle \vec{e}^1\|^2) = \text{Var}(\vec{X}) - \text{Var}(\langle \vec{X}, \vec{e}^1 \rangle) \quad (2.7)$$

have been minimized, in which the $Var(\langle \vec{X}, \vec{e}^1 \rangle) = \vec{e}^{1\dagger} \sum \vec{e}^1$. The \sum is the covariance matrix of \vec{X} . The \dagger is the conjugate transpose. So, to minimize the ϵ_1 we have to maximize $Var(\langle \vec{X}, \vec{e}^1 \rangle) = \lambda$. Thus the \vec{e}^1 is an eigenvector of \sum associated with its largest eigenvalue λ .

Next pattern can be found by minimizing the:

$$\epsilon_2 = \epsilon(\|\vec{X} - \langle \vec{X}, \vec{e}^1 \rangle \vec{e}^1 - \langle \vec{X}, \vec{e}^2 \rangle \vec{e}^2\|^2) \quad (2.8)$$

The EOF analysis has been applied in climate research for various topics. Such as monthly mean sea surface temperature analysis over the greater part of the Pacific Ocean (Weare et al. 1976), the comparison of dominant rainfall patterns from normal rainfall records over India (Singh 2004) and the variability of sea surface temperature analysis over the Atlantic (Guan and Nigam 2009).

The result of EOF analysis is presented in section 4.2 for the mean sea level pressure field.

2.7 Canonical Correlation Analysis

Here we are going to introduce another analysis method which focuses on a pair of random vectors \vec{X} and \vec{Y} . The Canonical Correlation Analysis (CCA) is designed to investigate the correlation structure for the two vectors. The CCA analysis was first described in 1936 by Hotelling (1936). Here we take the functions and theoretical analysis from the "Statistical Analysis in Climate research" (von Storch and Zwiers 1999).

We would like to summarize the purpose and idea of the Canonical Correlation Analysis in a short sentence. The objective is to find a pair of patterns \vec{f}_X^1 and \vec{f}_Y^1 with maximized correlation between the two linear combinations $\vec{X}^T \vec{f}_X^1$ and $\vec{Y}^T \vec{f}_Y^1$. A second pattern can also be calculated by maximizing the correlation coefficient of the corresponding linear combinations when it has no correlation with the first pair of combination vectors. The patterns \vec{f}_X^1 and \vec{f}_Y^1 are called the canonical correlation pattern.

We are going to explain the mathematics ways of CCA analysis in several general steps. At the very beginning we would like to introduce two inner products

$\beta^X = \langle \bar{X}, \vec{f}_X \rangle$ and $\beta^Y = \langle \bar{Y}, \vec{f}_Y \rangle$ to represent the linear combination. The maximum correlation of these two inner products can be maximize

$$\rho = \frac{\text{Cov}(\beta^X, \beta^Y)}{\sqrt{\text{Var}(\beta^X)\text{Var}(\beta^Y)}} = \frac{\vec{f}_X^T \text{Cov}(\beta^X, \beta^Y) \vec{f}_Y}{\sqrt{\text{Var}(\langle \bar{X}, \vec{f}_X \rangle) \text{Var}(\langle \bar{Y}, \vec{f}_Y \rangle)}} \quad (2.9)$$

Take the pattern for particular

$$\text{Var}(\langle \bar{X}, \vec{f}_X \rangle) = \vec{f}_X^T \sum_{XX} \vec{f}_X = 1 \quad (2.10)$$

$$\text{Var}(\langle \bar{Y}, \vec{f}_Y \rangle) = \vec{f}_Y^T \sum_{YY} \vec{f}_Y = 1 \quad (2.11)$$

Where \sum_{XX} and \sum_{YY} are the covariance matrices of \bar{X} and \bar{Y} . \sum_{XY} represents the cross-covariance matrix of $\sum_{XY} = \varepsilon((\bar{X} - \bar{\mu}_X)(\bar{Y} - \bar{\mu}_Y))$. We could obtain $\rho = \vec{f}_X^T \sum_{XY} \vec{f}_Y$.

The vectors \vec{f}_X and \vec{f}_Y could be found by maximized

$$\varepsilon = \vec{f}_X^T \sum_{XY} \vec{f}_Y + \zeta (\vec{f}_X^T \sum_{XX} \vec{f}_X - 1) + \eta (\vec{f}_Y^T \sum_{YY} \vec{f}_Y - 1) \quad (2.12)$$

Where ζ and η are Lagrange multipliers which used to account for constrains (2.10) and (2.11).

In order to maximize the ε , we calculated the partial derivatives of (2.12) and set it to zero. After few steps, we could get

$$\rho^2 = \vec{f}_X^T \sum_{XY} \vec{f}_Y \vec{f}_X^T \sum_{XY} \vec{f}_Y = 4\eta\zeta \vec{f}_X^T \sum_{XX} \vec{f}_X \vec{f}_Y^T \sum_{YY} \vec{f}_Y = 4\eta\zeta \quad (2.13)$$

The $4\eta\zeta$ is the eigenvalue of matrices $\sum_{XX}^{-1} \sum_{XY} \sum_{YY}^{-1} \sum_{XY}^T$ and $\sum_{YY}^{-1} \sum_{XY}^T \sum_{XX}^{-1} \sum_{XY}$.

Generally, the correlation coefficient could be calculated by the square root of the eigenvalue of the two matrices given above.

The CCA has been applied to study various different climate issues. It also has been introduced to investigate the relationship between the mean sea level pressure field and the Polar Low formation frequency over the North Atlantic (Zahn and von Storch 2008a). Judged from the mean sea level pattern, we have got a general view of time mean flow induced by the PMSL field. The linkage between the occurrence of Polar Low and the air flow will be shown.

Here we applied the CCA to our simulation output. The linkage between the Polar Low cyclo-genesis frequency and the mean sea level pressure over the North Pacific is presented in section 4.3.

2.8 Associate Correlation Pattern

We have presented different kinds of analysis method which will be applied for the simulation and tracking result in last two sections. But it is necessary to point out that both of them are designed for studying the linkage between seasonal statistics, such as seasonal mean fields or the number of Polar Lows formed, and not the linkage in individual synoptic situations. Which means we will get an overview about the most dominated pattern for the seasonal mean sea level pressure field over the North Pacific in the last 6 decades, or the seasonal mean sea level pressure pattern which has the highest correlation between Polar Low occurrence over the North Pacific.

The Associate Correlation Pattern (ACP) is designed to identify the correlations between time series of one single variable and a meteorological field. Such as the correlation between the annual mean sea level pressure field with Madden-Julian Oscillation (MJO) index and the sea surface temperature (SST) field with Southern Oscillation index (Wright 1985; von Storch et al. 1988).

Here we introduced the time series of detected Polar Lows as a vector \vec{Z}_t , a three dimensional matrix $\vec{V}_{(i,j,t)}$ represents the time series of meteorological field of the model simulation. The indices i and j count the grid boxes in the COSMO-CLM model domain. The field of the correlation coefficients between \vec{Z}_t and the time series of analyzed variable on the meteorological field at all grid points (i,j)

$$\rho_{(i,j)} = \text{corr}(\vec{Z}_t, \vec{V}_{(i,j,t)}) \quad (2.14)$$

is the associate correlation pattern.

The associate correlation pattern between the time series of detected Polar Low number and both the geo-potential height and air temperature field on the 100, 300, 500, 850 and 1000 hP level will be presented and discussed in detail in section 4.4.

Chapter 3

Case Studies

Basing on the simulation and tracking algorithm introduced in chapter 2, 10 cases of North Pacific Polar Lows were simulated to check the reliability of our simulations. We show three case studies in detail to verify the simulation and tracking algorithm. The sub-synoptic-scale phenomena of Polar Lows are described by the higher resolution model. A comparison between our simulation result, satellite images and results from other authors has also been presented to support. 9 of 10 cases can be clearly reproduced and tracked by adapted tracking algorithm.

We are going to present a summary of simulation and tracking result of 10 cases over the North Pacific in section 3.1. Three of them are discussed in detail in section 3.2, 3.3 and 3.4. They occurred in March 1977, March 1975 and January 1997 and were selected from the regions with highest frequency of Polar Low formation. The first is from Bering Sea, the second is from Gulf of Alaska, and the third is from Japan Sea. The discussion and conclusion of the tracking algorithm criterion are presented in section 3.5.

The verification has been processed in several steps.

Firstly, we checked the literatures of previous Polar Low studies, locating the exactly position and time of Polar Low cyclo-genesis from satellite imagery. Secondly, as Zahn et al. pointed out that the resolution of NCEP 1 data is not high enough to detect the Polar Low, we started the regional simulation one month before the Polar Lows formed which is forcing by NCEP 1 re-analysis data. Thirdly, we compared both results from simulation and the detected and tracking algorithm with detailed analyses from literatures. Positions, strength, trace and life cycle were all included. Finally, we cross checked the corresponding NCEP 1 re-analysis data. The downscale technology introduced in section 2.2 was designed to reconstruct the meteorological field with both higher spatial and temporal resolution. The important sub-grid scale characteristic for Polar Low study has been resolved.

At last, further discussion has been involved for the cases which exist in the reality but could not be detected or identified as a Polar Low by the tracking algorithm in the regional climate model output. It is impossible to reconstruct or track all of the Polar Lows. As we pointed in section 2.4, all the threshold values under different criterion have been settled in a scientific and reasonable but nevertheless to some extent arbitrary way. Various cases have been tested over North Atlantic and

North Pacific to identify the values. Some of the Polar Lows can be observed from the satellite imagery, but the simulation results fail to fulfill the filtered minimum, wind speed or the air-sea temperature difference criterion. Since these cases only take a small percentage of the result, a general number for climatology study is enough for statistics.

This chapter is mostly based on the material published in Chen et al. (2012).

3.1 Validation of case simulations

Here we show 10 cases which are carefully examined and verified with both the literature and original forcing data. For brevity there is no discussion in detail for all ten Polar Lows, but the information for all 10 cases is summarized in Table 3.1. The general date and locations are shown in the second column. The third column is the data source type. Observation data from the literature, the forcing NCEP 1 re-analysis data and the simulation result are all presented. The fourth column is the position at minimum pressure or first occurrence of Polar Low from satellite observation, corresponding simulation results are presented. We first checked the literature and satellite images and recorded the location of Polar Low. Then we checked the model result at the closest output time step, recorded the position of Polar Low. The fifth and sixth columns are the value of maximum wind speed and the minimum central pressure, and the time when it happens. We first checked the simulation result to find the minimum and maximum value respective, and checked the NCEP 1 data at the nearest time. The literature and tracking summary for each case is listed in the seventh and eighth column. Detailed information is shown in Table 3.1 and discussed below.

*Table 3.1 Examined cases of Polar Low formation. The asterisk * marks the 3 cases, which are discussed in detail.*

The characters "Observation" represent the data from literature, "NCEP 1" is the data at the corresponding time when there maximum wind speed and minimum central pressure exist in regional simulation. "Simulation" is the data from COSMO-CLM.

	Region and time	Data type	Precise Location		Max wind speed		Minimum central pressure		Literature	
			Position	Time	m/s	Time	hPa	Time		
1*	Gulf of Alaska 22 th Mar 1975	Observation	(149°W, 58°N)	20:21UTC 22 th	25	---	980	00:00UTC 23 th	(Businger 1987)	Detected by omitting criterion 4 (N-S)
		Simulation	(148°W, 55°N)	20:00UTC 22 th	21.9	10:00UTC 23 th	994	22:00UTC 22 th		
		NCEP 1	---	---	14	12:00UTC 23 th	997	00:00UTC 23 th		
2*	Bering Sea 7 th Mar 1977	Observation	(171°E, 48°N)	09:58UTC 7 th	---	---	984	12:00UTC 7 th	(Bresch et al. 1997)	Detected another one NOT like Bresch
		Simulation	(171°E, 49°N)	10:00UTC 7 th	14	04:00UTC 7 th	998	06:00UTC 6 th		
		NCEP 1	---	---	8.7	06:00UTC 7 th	997	06:00UTC 6 th		
3	Bering Sea	Observation	(168°E, 56°N)	22:24UTC 23 th	---	---	988	00:00UTC 24 th	(Businger 1987)	Detected omitting criterion 4 (N-S)
		Simulation	(169.7°E, 52°N)	22:00UTC 23 th	23.99	08:00UTC 23 th	995.2	14:00UTC 23 th		
		NCEP 1	---	---	14.12	06:00UTC 23 th	996	12:00UTC 23 th		

3.1 Validation of case simulations

	23 th Jan 1979									
4	Gulf of Alaska 13 th Mar 1985	Observation	(163°W, 52°N)	00:00UTC 13 th	25	07:00UTC 13 th	988	00:00UTC 14 th	(Businger and Walter 1988)	Detected by omiting criterion 4 (N-S)
		Simulation	(160.5°W, 54°N)	00:00UTC 13 th	19.62	03:00UTC 13 th	994	06:00UTC 13 th		
		NCEP 1	---		13.61	06:00UTC 13 th	997	06:00UTC 13 th		
5	Gulf of Alaska 05 th Mar 1987	Observation	(144.5°W, 58°N)	13:17UTC 05 th	---	---	---	---	(Douglas et al. 1991)	Detected
		Simulation	(140°W, 56°N)	13:00UTC 05 th	17.1	01:00UTC 05 th	998	05:00UTC 05 th		
		NCEP 1	---		7.8	00:00UTC 05 th	998.5	06:00UTC 05 th		
6	Gulf of Alaska 01 th Dec 1987	Observation	(140°W, 50°N)	00:00UTC 01 th	36	---	959	00:00UTC 01 th	(Bond and Shapiro 1991)	Detected by omiting criterion 4 (N-S)
		Simulation	(141°W, 49°N)	00:00UTC 01 th	25.89	12:00UTC 01 th	960	00:00UTC 01 th		
		NCEP 1	---		16.0	12:00UTC 01 th	960	00:00UTC 01 th		
7	Japan Sea 27 Feb 1996	Observation	(131.5°E, 40°N)	02:00UTC 27 th	---	---	---	---	(Fu et al. 1999)	Detected with changed criterion 3
		Simulation	(135°E, 42°N)	06:00UTC 27 th	17.53	12:00UTC 27 th	1005	05:00UTC 27 th		
		NCEP 1	---		13.02	12:00UTC 27 th	1004	06:00UTC 27 th		
8*	Japan Sea 21 th Jan 1997	Observation	(138°E, 40°N)	16:00UTC 21 th	25.3	22:00UTC 21 th at Aikawa	998.5	22:00UTC 21 th at Niigata	(Fu et al. 2004a)	Not detected
		Simulation	(138°E, 41°N)	16:00UTC 21 th	15.37	22:00UTC 21 th	1008	18:00UTC 21 th		
		NCEP 1	---		14.09	00:00UTC 22 th	1006	18:00UTC 21 th		
9	Japan Sea 10 th Feb 1997	Observation	(131°E, 40°N)	21:00UTC 10 th	---	---	---	---	(Fu et al. 2004b)	Detected with changed criterion 3
		Simulation	(131°E, 39°N)	21:00UTC 10 th	15.57	14:00UTC 10 th	1005	11:00UTC 10 th		
		NCEP 1	---		5.14	12:00UTC 10 th	1009	12:00UTC 10 th		
10	Japan Sea 19 th Dec 2003	Observation	(139°E, 40°N)	21:00UTC 19 th	20	---	992	00:00UTC 20 th	(Guo et al. 2007)	Detected
		Simulation	(139°E, 43°N)	21:00UTC 19 th	18.23	07:00UTC 19 th	1003	16:00UTC 19 th		
		NCEP 1	---		14.18	06:00UTC 19 th	1001	18:00UTC 19 th		

Firstly, we are interested in the fourth column, which is used for comparison of satellite images and the locations of Polar Low cyclo-genesis from simulation result. It is very important to get a general overview whether the COSMO-CLM simulation result is close to the reality. In 5 cases (case 1, 6, 7, 9 and 10), the simulated locations of Polar Lows are relatively near to the satellite images. The distance between two locations is not more than 2 degrees (about 220). For the other 4 cases (case 3, 4, 5 and 8), there is a position shift compared to the reality. The distance between the two positions is relatively far, more than 280 km. This comparison discloses that half of the downscaled Polar Lows are very close to reality. On the other hand, the aim of this study focus on the number of detected Polar Lows, so that a small bias in location is not a serious limitation. Indeed the position shift is less than 5 degrees shift which may be considered is acceptable.

The fifth column is the maximum value of 10 meter wind speed during the whole life cycle of each Polar Low. The result of simulation is selected from the maximum value of wind speed in a distance of 100 km along the tracks. NCEP 1 data is presented correspondingly at the closest available time out of 6 hourly values. The COSMO-CLM 10 meter wind speed is higher than the NCEP 1 data for all the 10 cases. There is a rapid increase of wind speed for case 1, 3, 6 and 9 (not shown).

The sixth column is the minimum value of central PMSL for the whole lifetime of each Polar Low. The

corresponding NCEP 1 value is also presented at the closest time step. Most of the cases show very similar values for the driving NCEP re-analysis and the simulated data, and in most cases the simulated minimum pressure is similar to observational estimates.

By checking the fifth and sixth columns, we found that our dynamical downscaling technology is effective. It is hard to investigate the Polar Low from the raw NCEP 1 re-analysis data. Some of the variables are different from the real phenomenon, like 10 meter wind speed which is too small. But the simulation improved the variables close to reality. On the other hand, by downscaling the coarse NCEP 1 re-analysis data to the higher resolution COSMO-CLM, the reconstructed model output carries the information from the forcing data. The PMSL is similar for both forcing and simulation data. But more meso-scale information can be presented which could not be found in NCEP 1. The meso-scale structure issue is presented in the detailed cases analysis next.

The detecting results by the tracking algorithm are listed in the eighth column. Three of them (case 2, 5 and 10) have been recorded under the default algorithm with the N-S direction criterion, used by Zahn for North Atlantic Polar Lows. The other seven cases are also simulated, but because of the northward direction (case 1, 3, 4 and 6) and the weak signatures (case 7, 8 and 9), they are not detected. By adjusting the criterions of the algorithm, 6 of them (case 1, 3, 4, 6, 7 and 9) have been detected and recorded. Case 7 and 9 are detected when the air-sea temperature difference which represents the vertical stability had been changed from 43 to 39K. Case 1, 3, 4 and 6 are also detected when we disabled the North-to-South direction criterion, but case 2 is not the one Bresch studied before. In particular for case 8, there is a weak signature on the mean sea level pressure field and air-sea temperature difference. It could not be detected by the tracking algorithm.

The traces for all the 9 detected Polar Lows are presented in Figure 3.1. The tracking results for these cases from the long time simulation are almost the same with the individual case studies. The traces we presented here are taken from long time simulation. Generally, 9 of the 10 cases have been tracked by the tracking algorithm with new criterions 3 and 4. The value of threshold which we presented in section 2.4 was reasonable and efficiency. With 10% failed cases, the bias is acceptable.

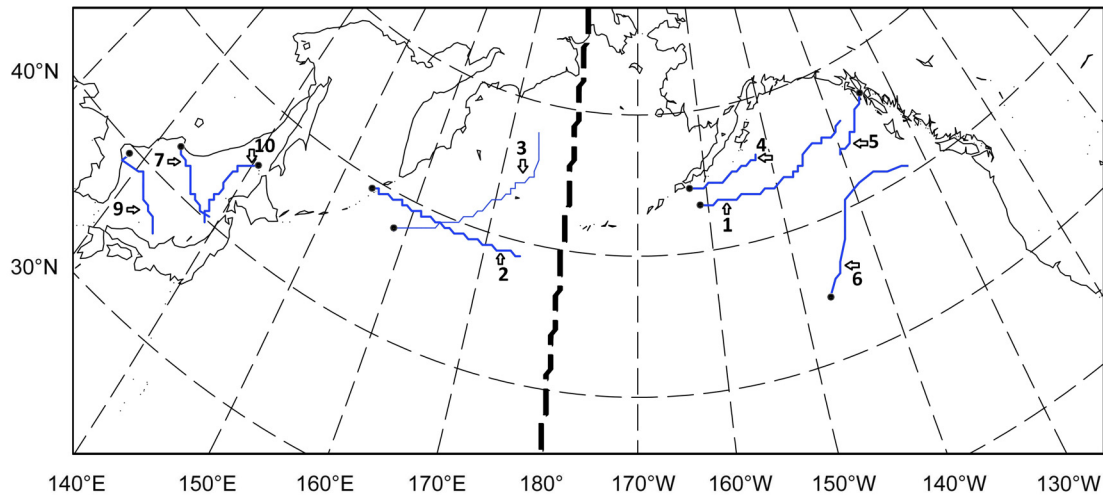


Figure 3.1 The traces of all the 9 detected Polar Lows. The black points represent the locations where the Polar Lows were first detected and recorded.

Case 1, 2 and 8 are discussed in detail in the next three sections. The forcing NCEP 1 re-analysis data, the satellite images, the simulation variables such as PMSL, filtered PMSL and 10 meter wind speed are all presented at the corresponding period of the Polar Lows.

3.2 A Case from Bering Sea

Case 2 is a Polar Low on 6 – 7th March 1977 in the Bering Sea, which was examined by Bresch (1997). The general cloud pattern of this case at 09:58UTC 7th March is presented by the satellite image which Bresch et al. used before (1997) – see Figure 3.2, where 2 Polar Lows are marked.

The cloud pattern represented by “D” is the Polar Low investigated by Bresch. The “P” represented another low system on the mean sea level pressure field which Bresch did not consider. We are going to check the corresponding simulation result for both cloud patterns in the model output.

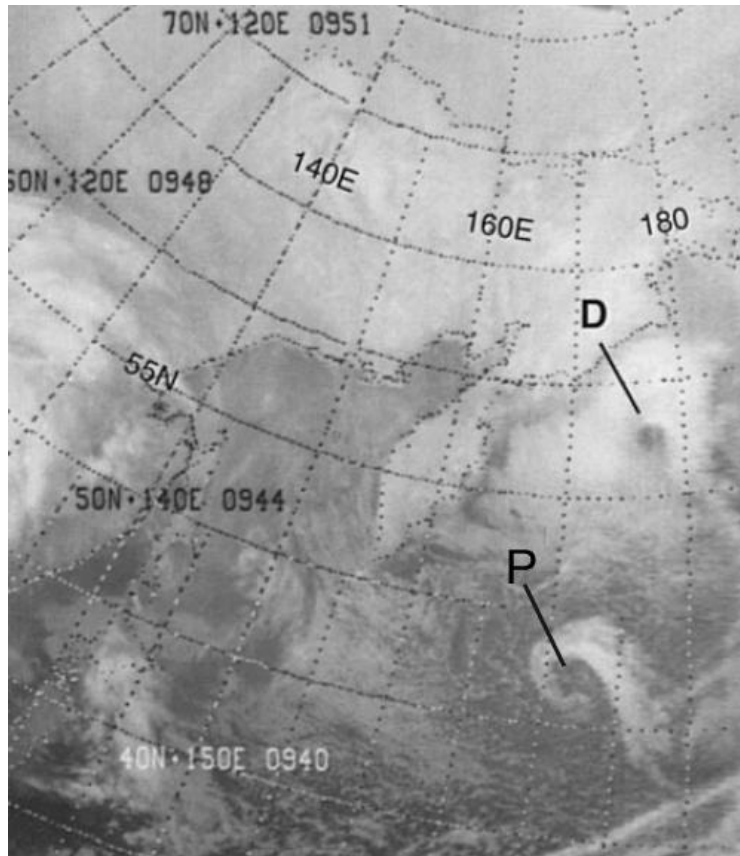


Figure 3.2 NOAA-5 infrared satellite image at 09:58UTC 7th March 1977 (taken from (Bresch et al. 1997)); “P” marks the cloud pattern of the Polar Low in COSMO-CLM simulation and “D” is the Polar Low described by Bresch et al., (1997).

We started the simulation on 1st February 1977, and the downscaling simulation with the COSMO-CLM provides more sub-synoptic-scale detail (Figure 3.3). We find the same synoptic situation as Bresch et al. (1997), with the large scale low in the Bering Sea moving cold air southward at its western flank.

In the reconstructed mean sea level pressure field appeared a clearly meso-scale feature of a Low system. The “P” represented a spiral structure on the PMSL field with a southeast-ward direction. By checking further criterions, it was identified to be a Polar Low.

The 06:00UTC 6th March simulated PMSL field (Figure 3.3) shows a mature state synoptic low S, and a sub-synoptic-scale pressure minimum P, at approximately around (156°E, 50°N). Later the simulated Polar Low P was moving southeast-ward and becoming weaker. The 12:00UTC model result shows a weaker PMSL pattern of Polar Low. After 18:00UTC, the low travelled over the sea and moved east-ward along the 50°N latitude line. At 10:00UTC 7th March, the position is around (172°E, 50°N), generally the same as the satellite image at 09:58UTC (Figure 3.2).

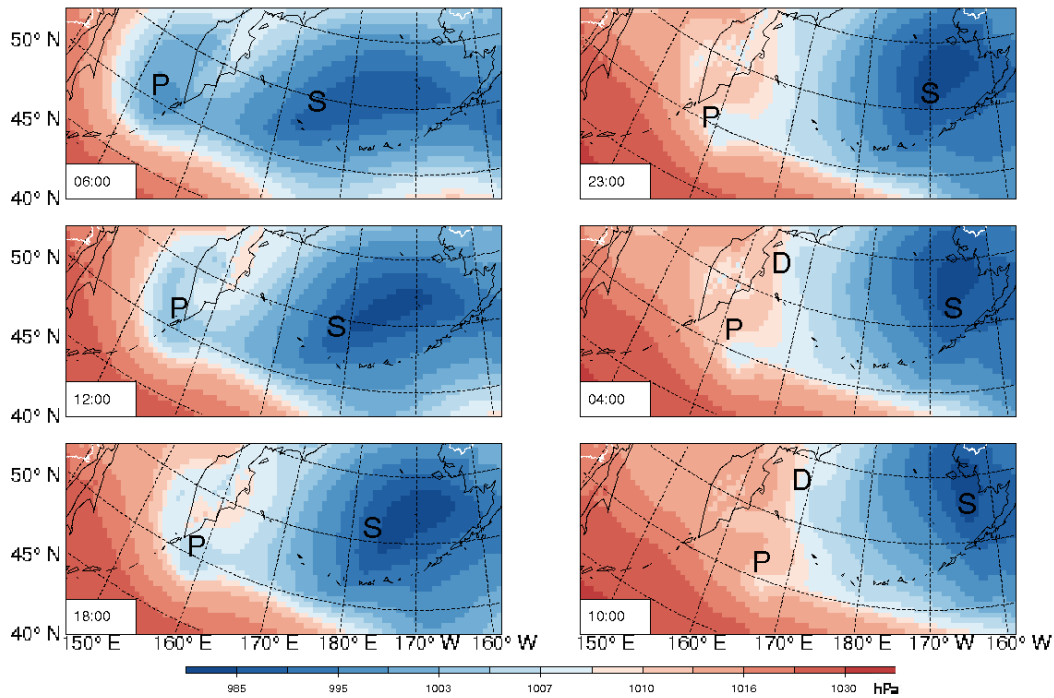


Figure 3.3 PMSL of COSMO-CLM simulation results from 06:00UTC 6th to 10:00UTC 7th March 1977, P represents the Polar Low, S represents the synoptic low and D represents the Polar Low in Bresch et al. (1997). Left column: maps for 06:00, 12:00 and 18:00UTC on 6th March 1977; right column: 23:00UTC in 6th March, 04:00 and 10:00UTC on 7th March 1977. The satellite image in Figure 3.2 corresponds to the phase at the bottom map on the right. (Units: hPa)

The sub-synoptic-scale swirl D, as shown in Figure 3.2, is reproduced by our simulation only to a very limited extent, namely as a very weak disturbance of the isobars at 10:00UTC on 7th March 1977 (Figure 3.3). Interestingly, Bresch et al. (1997) focused on the D-case, and addressed “our” P case only in passing.

By checking the filtered PMSL field over the same period (Figure 3.4), we have found there is an obvious minimum located at the corresponding position where the Polar Low “P” exists. The filtered minimum was detected since 06:00UTC at the south of Kamchatka Peninsula around (156°E, 50°N), the central value is below -1.5 hPa. The Polar Low is getting stronger on the filtered PMSL field (fall below -2 hPa) in the next 12 hours. With a southeast-ward direction the filtered minimum was getting weaker during 23:00UTC 6th Mar and 04:00 7th Mar. While it researched -2hPa at its central point at 10:00UTC 7th Mar again. This track is well detected by the automated detection and tracking algorithm (Figure 3.5).

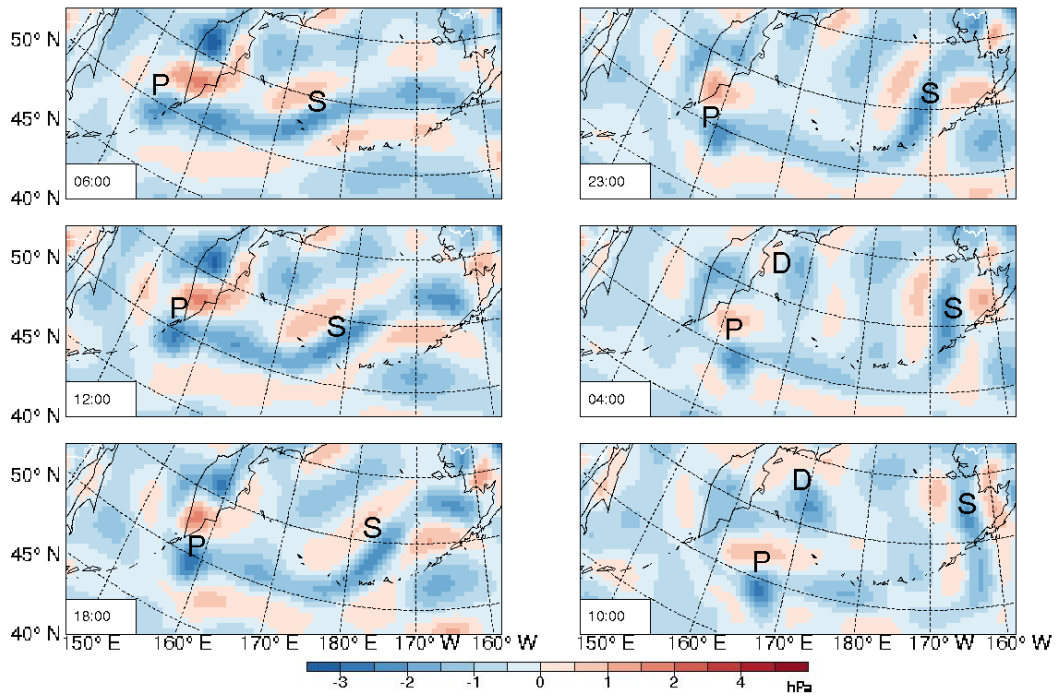


Figure 3.4 Filtered PMSL field from the same date of Figure 3.3.

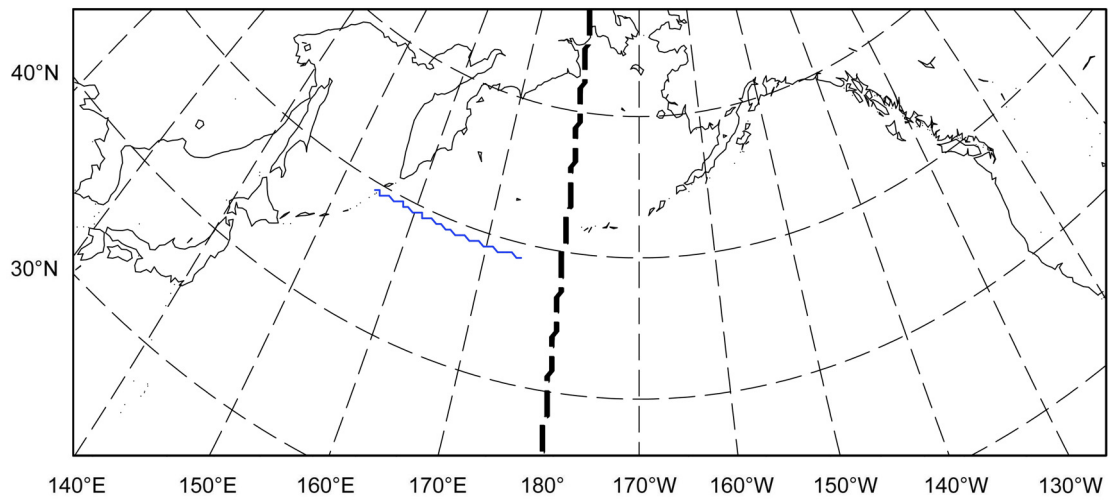


Figure 3.5 The result of tracking algorithm from 06:00UTC 6th to 00:00UTC 8th March 1977.

Polar Low “P” forms at south of Kamchatka Peninsula and moves eastward. It is probably due to the cold flow from Siberia. The cold air outbreak which induced by the synoptic low S (Figure 3.3 and Figure 3.4) brings cold air from the polar region in the north. Once the cold air moves off the

Kamchatka Peninsula, it meets the relatively warm open ocean. As we discussed in the first chapter, northward Kuroshio (known as Japan Current off the northeast of Hokkaido) brings warm water from the south. The warm SST leads to a great air-sea temperature difference. The Polar Low generated under this instability mechanism and moves east-ward with a tiny southward direction, finally perished on the open ocean.

We also have to mention that the Polar Low which Bresch investigated is also presented at 04:00 and 10:00UTC 7th Mar marked as “D”. Especially for 10:00UTC, two filtered minimum located at the same positions as in the satellite images (Figure 3.2). “D” is too weak to be detected as a Polar Low by the algorithm. On the other hand, we are interested about this case. It is labeled with “D” in Fig 3.2, 3.3 and 3.4. There is a corresponding minimum on the filtered PMSL field over the Bering Sea (Figure 3.4). Further information about filtered PMSL field after 10:00UTC 7 Mar are presented in Figure 3.6. We were interested in whether this case can be recorded.

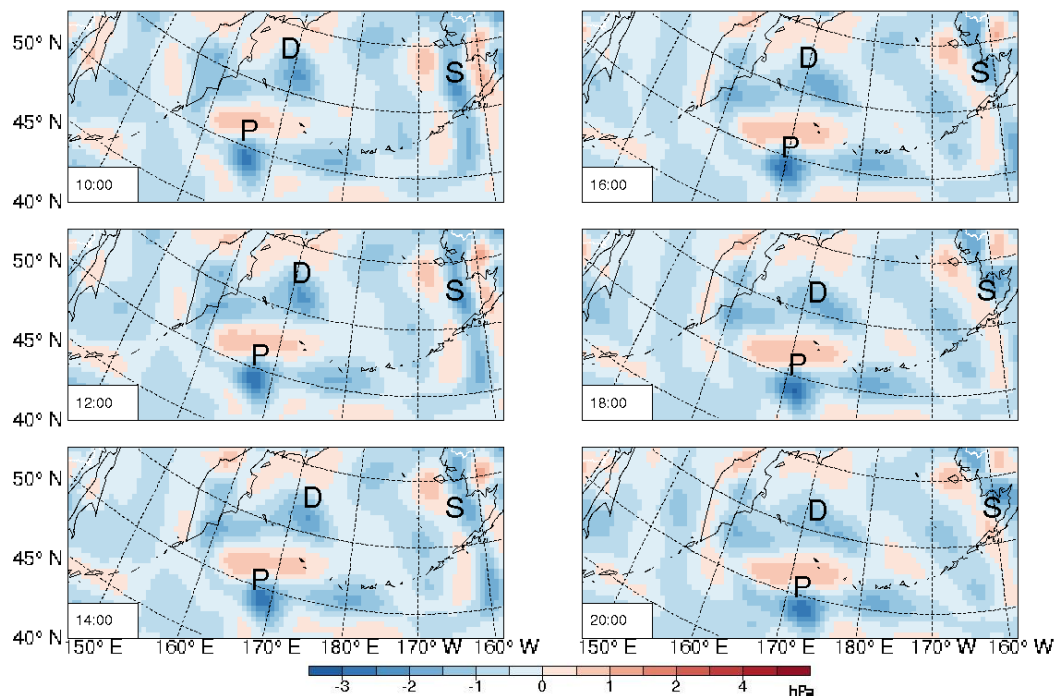


Figure 3.6 2 hourly filtered PMSL field from 10:00UTC to 20:00UTC 7th March 1977, P represents the Polar Low, S represents the synoptic low and D represents the Polar Low in Bresch et al. (1997). The satellite image in Figure 3.2 corresponds to the phase at the top map on the left. (Units: hPa)

By checking the filtered minimum in the next 12 hours, we find that the Polar Low which marked as “D” is relatively weak during its whole life cycle. 10:00UTC 7th Mar is the peak stage with filtered minimum below -1.5 hPa at central position. The central minimum only researched -1 hPa after 14:00UTC 7th Mar. The values of filtered minimum in the central position are always between -1 and -0.5 hPa. This Polar Low is getting weak very quickly in the filtered field with a southeast-ward

movement. The direction is similar with what Bresch observed from satellite image. They both first formed at early 7th Mar around (175°E, 58°N), and moved southeast-ward around (176°E, 57.5°N) at 12:00UTC 7th Mar. Bresch pointed that this Polar Low cross the date line around 22:00UTC 7th Mar, this is similar to what we found at 20:00UTC 7th Mar. The central position is very close to the 180° longitude.

The trace from satellite observation (not shown), simulation and detecting algorithm share a similar position and southeast-ward direction. It indicates that the application of dynamical downscaling method is effective. The reconstructed meso-scale phenomenon from coarse NCEP 1 re-analysis data is close to the reality. The band-pass filter has captured the relative weak disturbance from the PMSL field. On the other hand, we have to point out that the strength of this filtered minimum is mostly higher than -1hPa, it has not reached the threshold of -2 hPa. This case only can be detected and recorded by lowering down the threshold of the tracking algorithm. So it could not be detected or recorded by the default tracking algorithm.

Thus, it is impossible to count every Polar Low by our detecting and tracking algorithm with little bias. To get the multi-decadal climatology characteristic of Polar Lows over the North Pacific, a general number with reasonable threshold on the statistics level is needed. The criterions we presented in section 2.4 have been verified on Atlantic (Zahn and von Storch 2008a). It is not necessary to change the criterions just for some particular or extreme cases. More synoptic storms and front cyclones would be involved into the tracking result. Few Polar Low numbers close to the reality comes along with great error of synoptic cyclones. It is undesirable both in statistic and dynamic. So here we only take the trace of "P" (Figure 3.2) for the tracking result. The "D" had been excluded.

Finally we checked the relatively coarse-grid NCEP 1 re-analysis air pressure field on 10:00UTC 7th March in Figure 3.7. It is interpolated from 06:00 and 12:00UTC. A large synoptic low is located in the Bering Sea (see "S" in Figure 3.7). The location of the Bering Sea low "S" is stable over the next 36 hours. In the southward air stream at its western flank, there are two diffuse depressions "D" and "P".

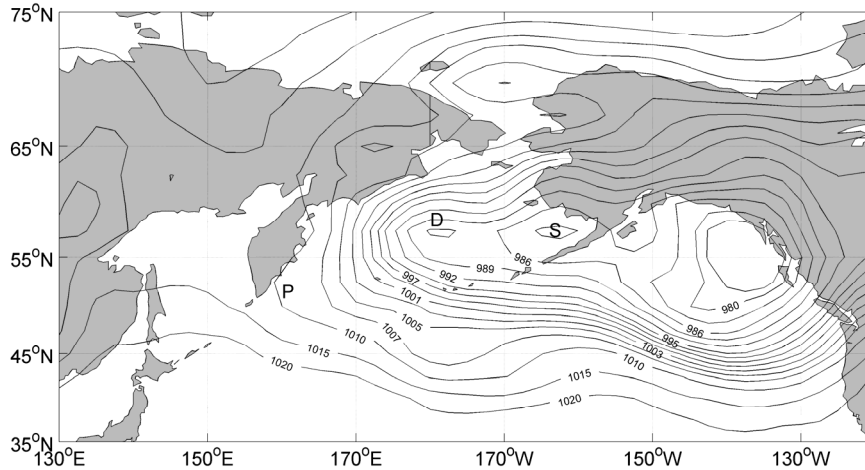


Figure 3.7 PMSL as described by NCEP 1 re-analysis with a 1.875° grid resolution interpolated for 10:00UTC 7th Mar 1977, when a Polar Low formed west of the Kamchatka Peninsula. P represents the Polar Low we studied, S represents the synoptic low and D represents a Polar Low discussed by Bresch et al. (1997).

Caused by the coarse spatial resolution in NCEP 1 re-analysis data, both lows are hard to identify. By a quick judgment of Figure 3.7, we have found the low systems labelled with “P” and “D” appeared a meso-scale feature on the PMSL field. They are mainly induced by the synoptic low marked as “S”. The “S” existed with a relatively large spatial scale and stable. The “P” low is not observed in the NCEP 1 data, only exists as a weak disturbance. The low represented by “D” is relatively weak. No Polar Low information can be obtained from this low resolution initial field. The tracking of both D and P in NCEP 1 analysis data is not possible because of the large spatial (for “P”) or temporal (for “D”) resolution.

3.3 A Case from Gulf of Alaska

In this section, we are going to discuss our case 1 which formed on 22th March 1975 south of Alaska described by Businger (1987). The satellite images (Figure 3.8) shows the mature stage of this Polar Low, labeled as “P”. It lasted nearly 48 hours.

The COSMO-CLM results (Figure 3.9) showed the initial and mature stages of the Polar Low “P”. The spatial scale is about 500 km and the central pressure minimum is below 995 hPa around 22:00UTC 22th. The minimum pressure from observation is 980 hPa at 00:00UTC 23th (Businger 1987), so that the simulation is considerably less deep, namely 15 hPa. This Polar Low was formed around (154°W , 54°N) at 00:00UTC 22th March 1975. With a northeast-ward movement, the Polar Low had grown stronger and stronger with a maximum wind speed of 18 m/s at 22:00UTC (Figure 3.10). The Polar Low turned to its peak stage around (147°W , 55°N) at 16:00UTC 22th March 1975 and lasted the next 8 hours. It

still kept a northeast-ward direction.

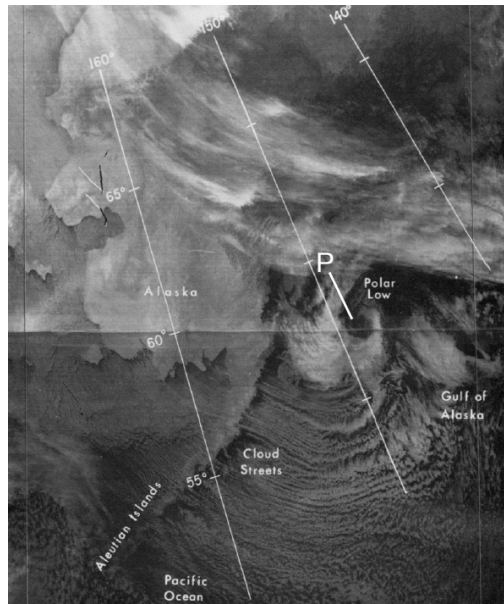


Figure 3.8 NOAA-4 infrared satellite image at 20:21UTC on 22th March 1975, P represents the Polar Low (Businger 1987).

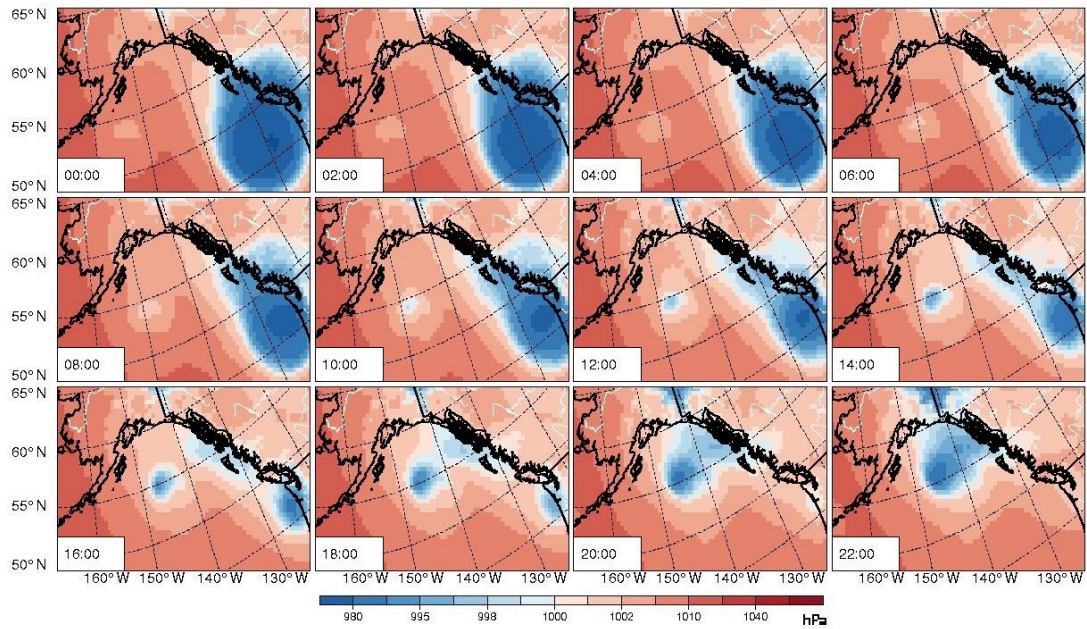


Figure 3.9 PMSL of COSMO-CLM simulation result for the Polar Low on 22th March 1975 in the Gulf of Alaska. The results were presented by every two hours from 00:00 to 22:00UTC. Figure 3.8 shows the corresponding satellite image for the bottom third map. (Units: hPa)

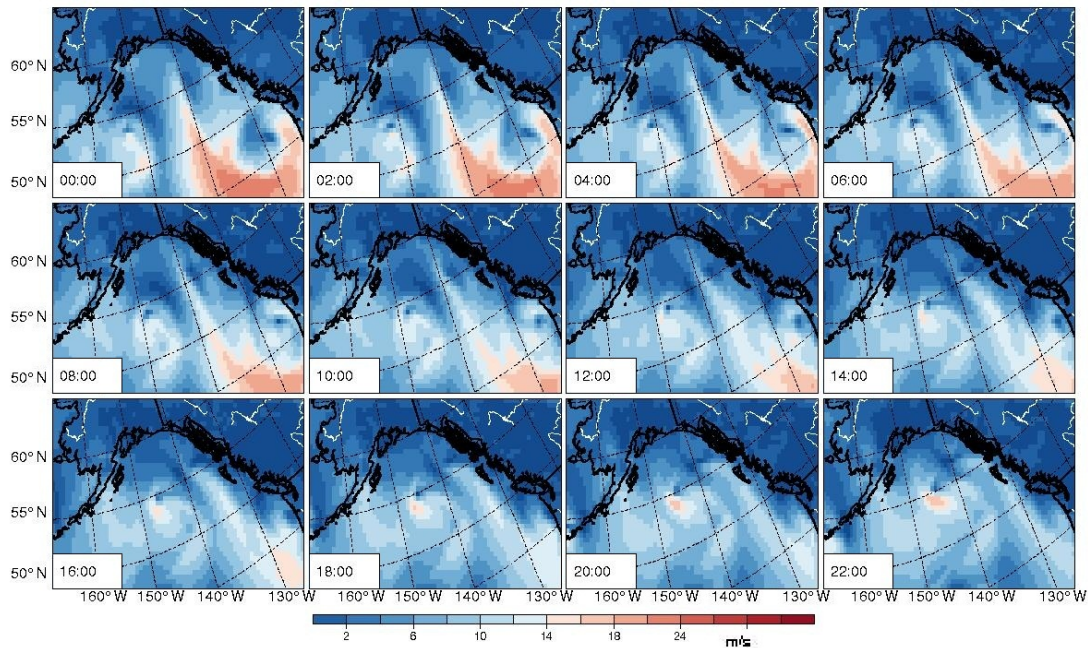


Figure 3.10 Wind speed field of COSMO-CLM simulation result for the Polar Low on 22th March 1975 in the Gulf of Alaska. The results were presented by every two hours from 00:00 to 22:00UTC 22th March 1975. Figure 3.8 shows the corresponding satellite image for the bottom third map. (Units: m/s)

The 10 meter wind field presents a much more clearly comma structure of this Polar Low. The initial stage of this Polar Low is shown in the first row of Figure 3.10, from 00:00 to 06:00UTC. The high wind speed value in the east belongs to the synoptic low which induced the Polar Low. The wind speed in the central position of this Polar Low at this time was round about 12 m/s. The second row of Figure 3.10 shows the developing stage of this Polar Low. The 10 meter wind speed researched 16 m/s at 12:00UTC. The wind speed of the synoptic low decreased very quickly. Finally the Polar Low reached its mature stage after 16:00UTC. The wind speed increased over 18 m/s. The Polar Low appeared to be a perfect spiral pattern on the wind field and moved northeast-ward directly.

From the filtered PMSL fields at the same period (Figure 3.11), we found that the meso-scale pressure phenomenon is presented at the corresponding location. With a strengthen core minimum pressure and northeast-ward position trace, the life cycle of this Polar Low is obvious and easily summarized.

Another noteworthy point is that we have found that the filtered PMSL field appears a comma structure which we could not observe from the PMSL field directly. It is indicated that the band-pass filter is efficacious to extract the meso-scale structure of Polar Low. The filtered minimum pressure field is more direct and effective for analysis. We can get the position and trace of Polar Low by detecting and recording the filtered minimum easily.

There was another important issue about the tracking algorithm we have to mention here. Even though this Polar Low can be detected after band-pass filtering: it appeared as minimum on the filtered mean sea level pressure field, but it still could not be recorded by the default algorithm which was applied to the North Atlantic (Zahn and von Storch 2008). By checking the criterions step by step, we found that it did not fulfill the third criterion. The air-sea temperature difference which represents the vertical stability has been set to 43K to identify the Polar Lows in North Atlantic. But it seemed too high for this case. This Polar Low has been perfectly recorded when we reduced the threshold to 39K (Figure 3.12).

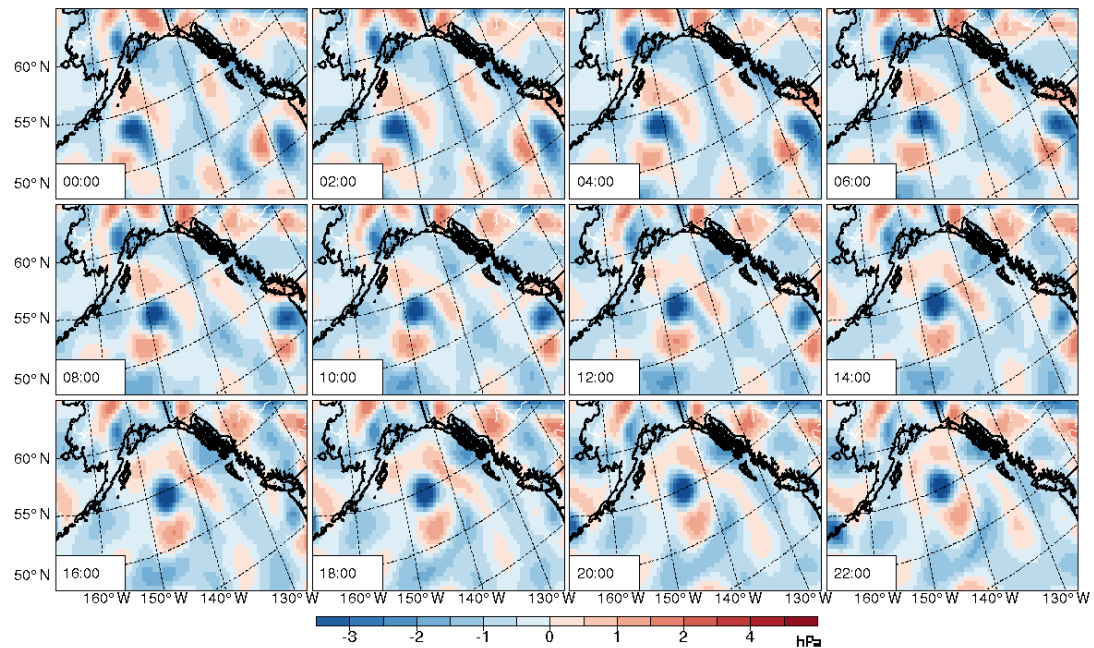


Figure 3.11 Filtered PMSL field of COSMO-CLM from the same date of Figure 3.9.

On the other hand, we found there is another minimum at the corresponding position of synoptic low on the filtered PMSL field (Figure 3.11). The synoptic low moved northward and perished near the coast of American Continent at 16:00UTC 22th March (Figure 3.9). The minimum of this synoptic also can be detected. By checking the tracking algorithm in a further step, we found this trace was excluded by several criterions: the air-sea temperature difference, the maximum wind speed and the N-S direction. The wind speed field showed that this synoptic low had over 14 m/s wind speed during 00:00 to 06:00UTC (Figure 3.10), and it was getting weaker and weaker. After 08:00UTC, the wind speed around the synoptic position is only 6 – 12 m/s. This is an example that the tracking algorithm excluded the synoptic lows automatically and efficiently.

It is unwise to change the threshold value in this tracking algorithm which had been applied for various cases and a long term climatology study over the North Pacific just because of only one special

case. So we took more cases to verify this air-sea temperature difference issue. Nearly 30% cases are not recorded under the default threshold value 43K. Therefore, the modification of this vertical stability by 39K was acceptable. We are going to discuss it in detail in section 3.4.

Here we have to mention that Polar Lows usually take place during cold air outbreaks, with a movement southward from ice covered land to the open ocean. Quite uncommonly, the track of this Polar Low has a slight northward component. This situation may be due to the steering synoptic circulation induced by the synoptic low to the east. By the criterion 4 of the tracking algorithm we presented in last chapter, this case is detected but not recorded. Omitting the north-to-south criterion, the track of this case had been perfectly recorded (Figure 3.12). In order to avoid this north-to-south direction criterion deviation, we consider statistics derived from analysis both with and without the N-S direction criterion for a comparison. The results will be presented in chapter 4 and discussed in detail.

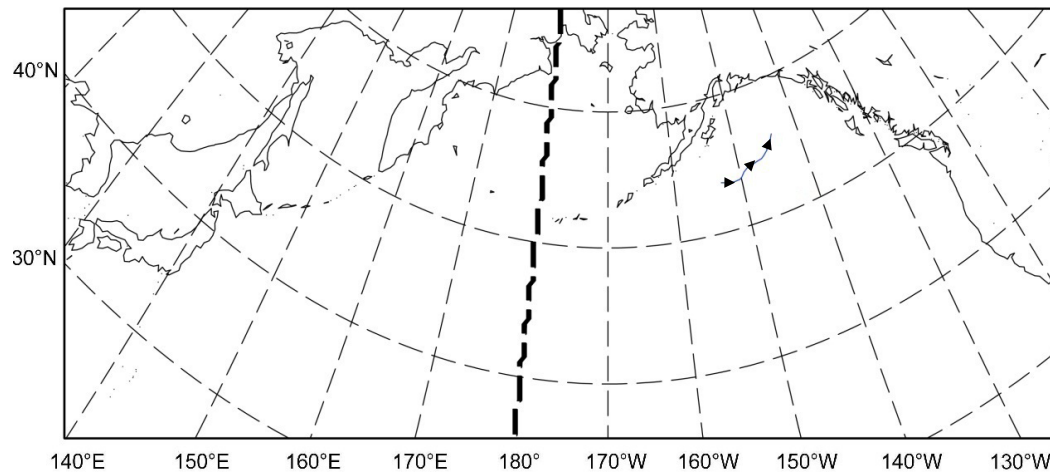


Figure 3.12 The result of adapted tracking algorithm from 00:00 to 22:00UTC 22th March 1975.

This Polar Low was hardly detectable in the NCEP 1 re-analysis PMSL field (Figure 3.13), but well reproduced by our regional model and tracked by the algorithm.

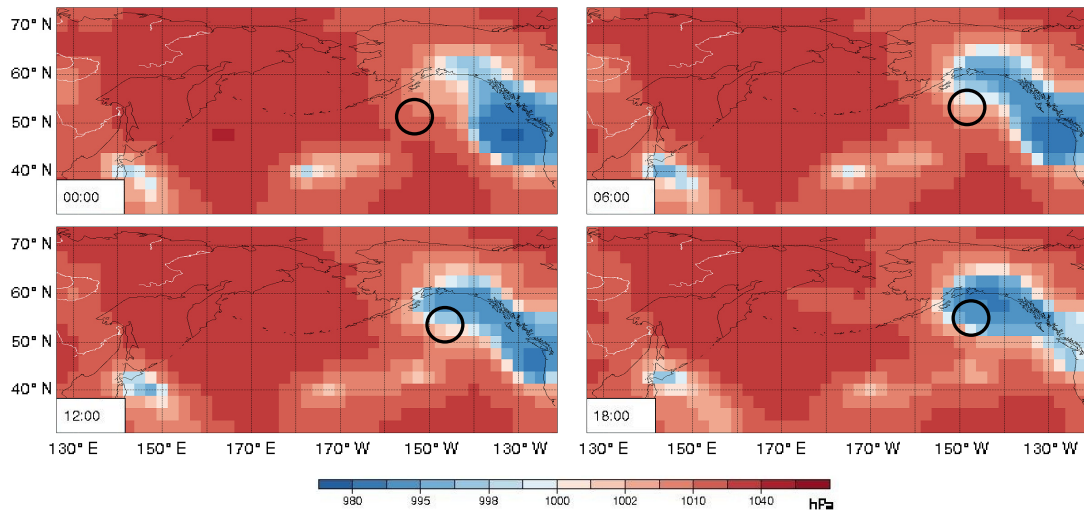


Figure 3.13 PMSL fields of NCEP 1 re-analysis data on 00:00, 06:00, 12:00 and 18:00UTC 22th March 1975.
(Units: hPa)The black circles represent the location of the Polar Low.

There is no obvious indication for a Polar Low on the NCEP 1 PMSL field. Again, the dynamical downscaling technique is effective for our purpose.

3.4 A Case from Japan Sea

The third case took place on 21th January 1997, when a Polar Low moved across the Japan Sea (Fu et al. 2004a). Figure 3.14 shows in the satellite imagery sequence the mature stage of this Polar Low. The Polar Low on 21th January 1997 lasted less than 32 hours. The minimum central pressure is 998.5 hPa at 22:00UTC 21th from observation (Fu et al. 2004a). The value from simulation result is 1008 hPa at 18:00UTC 21th. It seems that this case is weak in the regional climate model.

The Polar Low was formed off the western coast of Hokkaido Island on 20th January 1997. With a southward movement direction, the Polar Low turned to the developing stage after 06:00UTC 21th. The cloud pattern of this Polar Low wrapped up to form like an inverted spiral shape in the next 10 hours (Figure 3.14). The size and circulation pattern showed an obvious change. The eye structure with a cloud free center appeared after 10:00UTC. This typhoon-like pattern is convincing evidence for Polar Low formation in the high latitude region.

This Polar Low is probably induced by the synoptic scale east-westward trough with cold air at 500 hPa. Cold air outbreak travels southward to the relatively warm Japan Sea. High temperature difference in the vertical induced the Polar Low. Following the cold flow from the north, the track is southward across the Japan Sea and ends on Japan Island. This Polar Low decayed quickly after having reached

Japan Island.

Fu et al. analyzed (2004a) that this Polar Low had a weak signature at the surface in the Regional objective analysis (RANAL) data of JMA (Japan Meteorological Agency). Yanase et al. studied this case by a 5 km resolution regional climate model (2004), it is visible in the high spatial resolution simulation results. By checking the result from our COSMO-CLM simulation for the same period, no obvious Polar Low pattern can be found at the corresponding location (Figure 3.15). Only weak disturbance showed up on the mean sea level pressure field. This disturbance existed for a short period and the central pressure was round about 1007 hPa. It is really hard to identify a Polar Low from such weak signature on the mean sea level pressure field.

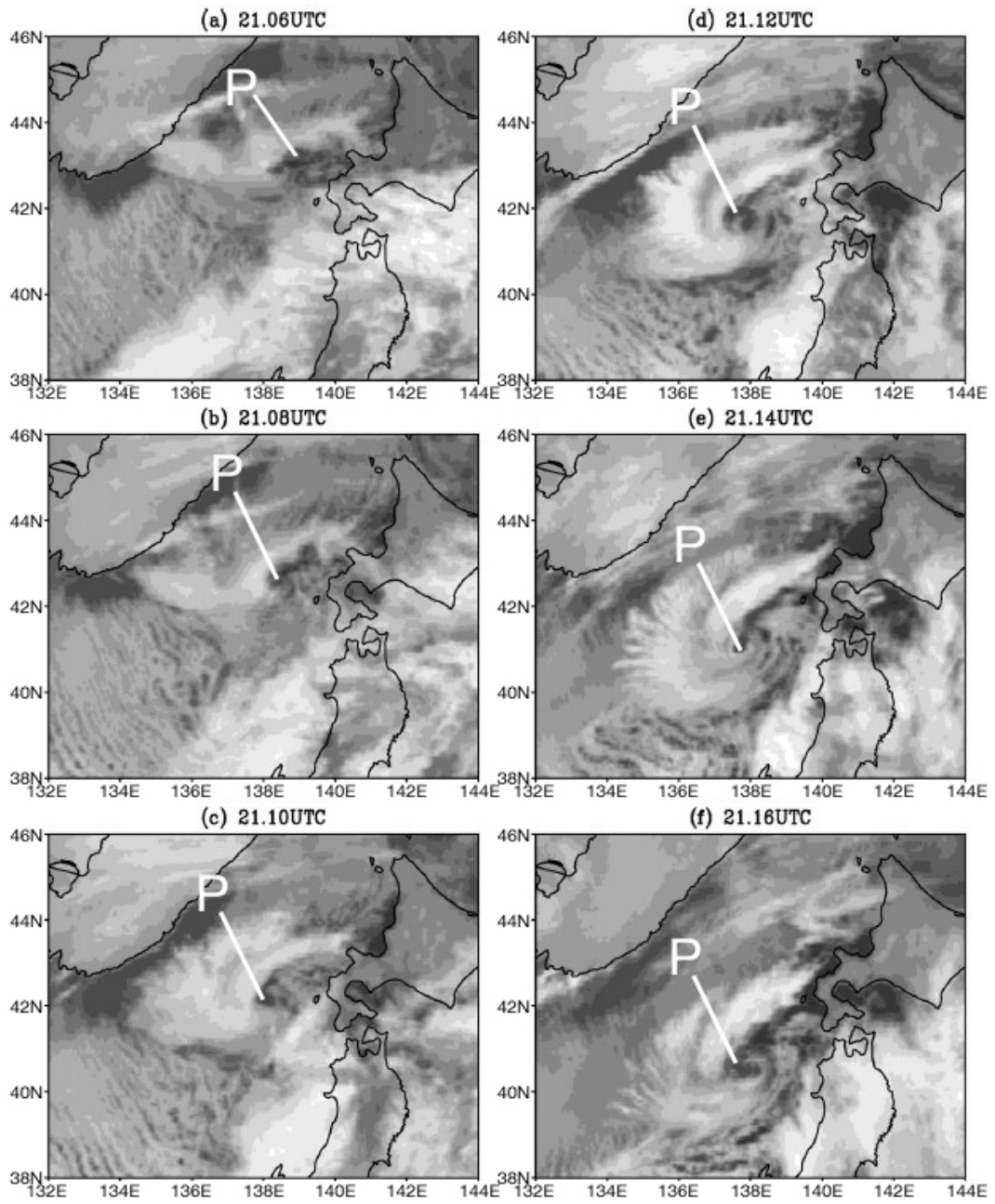


Figure 3.14 Two-hourly GMS-5 TBB satellite image from 06:00 to 16:00UTC 21th Jan 1997, P marks the Polar Low (Fu et al. 2004a).

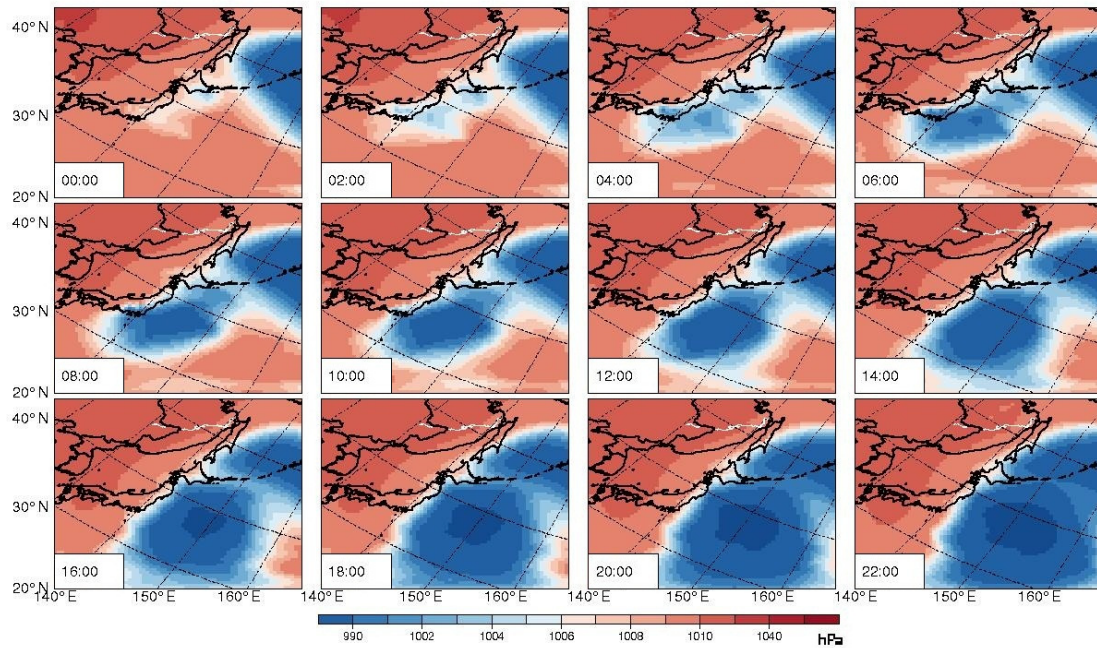


Figure 3.15 Mean sea level pressure of COSMO-CLM simulation results for the Polar Low on 21th January 1997 in Japan Sea. The results were presented by every two hours from 00:00 to 22:00UTC 21th January 1997. (Units: hPa)

The spatial resolution of our simulation output is 0.4° grid, about 50 km. Compared to the 5 km resolution simulation result from Yanase et al. (2004), the relatively coarser resolution is supposed to be the reason of no obvious pattern on PMSL field. The structure of this Polar Low can be improved by a higher spatial resolution regional climate simulation.

On the other hand, we are still interested in the skill of the tracking algorithm, even there is no Polar Low detected. We show the corresponding filtered mean sea level pressure field for the same time period as for the PMSL field in Figure 3.16.

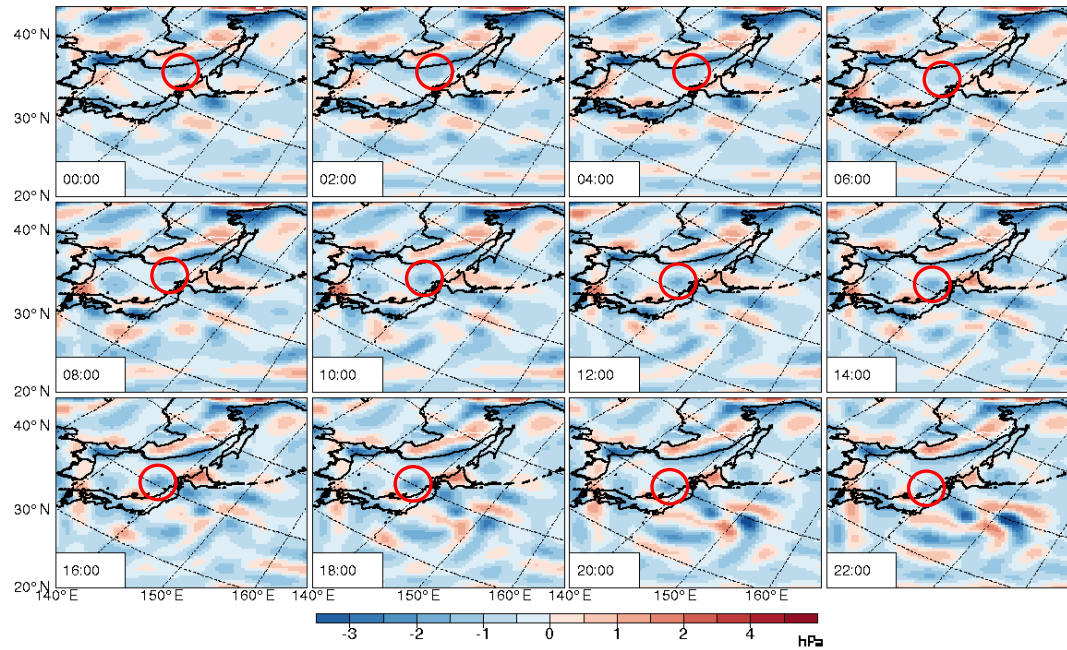


Figure 3.16 Filtered PMSL field of COSMO-CLM from same date of Figure 3.15. (Units: hPa) Red circles represent the location of the Polar Low.

We found there was a weak filtered minimum located over the Japan Sea and moving southward (marked by red circles in Figure 3.16). The trace of the filtered minimum is consistent with both the satellite observation and the result from literature. Unfortunately, the series of filtered minimum were too weak to be detected and recorded. From 00:00 to 14:00UTC the central minimum was just round about -0.5 hPa. After 16:00UTC 21th it fall below -1 hPa. This case did not fulfil the first criterion which we presented in section 2.5: strength of the minimum band-pass filtered PMSL: ≤ -2 hPa once along the track.

Although the COSMO-CLM result had weak disturbance showed up for this case (Figure 3.15) and the signature is too weak to be tracked by our automated algorithm (Figure 3.16), it is clearly visible as a cold core vortex at the 500 hPa upper level (Figure 3.17). The simulated track shows the Polar Low moving realistically southward across the Japan Sea.

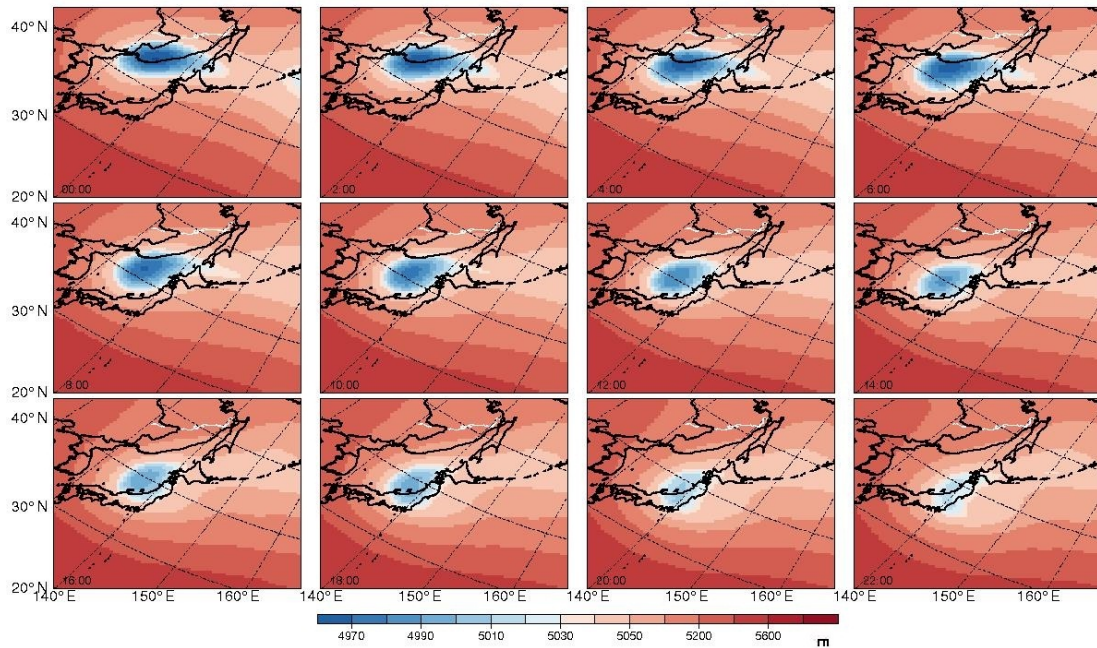


Figure 3.17 The geo-potential height on the 500 hPa level of COSMO-CLM simulation result for the Polar Low on 21th January 1997 in the Japan Sea. The results were presented by every two hours from 00:00 to 22:00UTC.
(Units: m)

It would be a challenge to develop a tracking algorithm on the 500 hPa pressure levels. It may be a valuable improvement for the tracking algorithm which we have applied. The result would be a possibility to correct the bias due to the cases which cannot be detected or recorded by their weak signature at the surface.

3.5 Conclusion

In this chapter, we have shown an overview on 10 Polar Low cases and 3 cases in detail to verify the downscaling technology and tracking algorithm which we introduced in chapter 2. The simulation results had been presented for different variables as mean sea level pressure field, 10 meter wind field and geo-potential height field on the 500 hPa level.

As a preparational analysis for the feasibility of simulating and investigating long term trends and variability of Polar Lows in the North Pacific, we have examined the performance of the dynamical downscaling system, which makes use of the NCEP 1 re-analysis data as forcing of the COSMO-CLM limited area model. The objective is to generate sub-synoptic scale descriptions of Polar Lows, without making use of high-resolution initial fields. In three case studies of Polar Low formation and life cycle,

we found due to the higher spatial resolution considerably more detail in the simulation compared to the re-analysis description of NCEP. Also the hourly output turns out to be helpful compared to the routine 6 hourly output from NCEP 1 re-analysis. We also compared model results with satellite observations, available from detailed studies of the ten cases, and found that our system adds realistic sub-synoptic details mostly consistent with the satellite observations.

Furthermore, we could improve our simulation result by a higher resolution grid. However, the higher the resolution we use, the more computing time is necessary. The limited computing resource and time is a constraint we have to concern. It is perfect to use high resolution model for individual case studies but not for climatology investigation. The high resolution simulation result is a great help to investigate mechanism of Polar Low formation or dynamical process. But the aim of this study is focus on the multi-decadal variability of Polar Lows. Most of the 10 test Polar Lows can be reconstructed and detected on our 0.4 degree grid.

We also found that the detection and tracking algorithm, originally developed for the North Atlantic, needed to be adapted to a somewhat different situation in the North Pacific. By adjusting the threshold value of the criterions such as the air-sea temperature difference and the north-to-south direction, most of the cases are well detected and recorded. Now the algorithm is suitable for statistical study of the Polar Lows over the North Pacific.

Chapter 4

Multi-decadal Climatology

The dynamical downscaling system has demonstrated its skill in successfully describing and tracking North Pacific Polar Lows. Therefore we have launched a continuous simulation with COSMO-CLM, forced by six decades of NCEP 1 re-analyses. The output of this simulation is searched for the formation and movement of Polar Lows, and changes from year-to-year as well as a frequency trend are determined. The Polar Low climatology over North Pacific from this simulation extending from 1948 to 2010 is presented in this chapter.

From the result of case studies presented in last chapter, we found that there are some Polar Lows which do not fulfill the North-to-South direction criterion during the tracking algorithm over the North Pacific. In Chapter 3, we found 3 of 10 cases the Polar Lows with an eastward or northeast-ward direction over the North Pacific in reality (Table 3.1), which is related to the large-scale synoptic circulation. The question is whether to include this criterion or not.

We are looking for an estimation of Polar Low number which is close to the reality in this study. It is impossible to count every Polar Low precisely. On one hand, more cyclones and synoptic storms will be included without North-to-South criterion. On the other hand, some Polar Lows with northward direction will be excluded with the North-to-South criterion. We compared the results with and without North-to-South criterion. The comparison will be discussed in detail to investigate the multi-decadal climatology of Polar Lows with different constraints over the North Pacific.

Based on the verification from last chapter, we applied the 63 years NCEP 1 re-analysis data to the COSMO-CLM model and the tracking algorithm in a further step. Climatology characteristic of Polar Low cyclo-genesis over the North Pacific is presented in section 4.1; the EOF results of PMSL is discussed in section 4.2; the linkage with sea level pressure, upper layer geo-potential height and surface temperature over the ocean is presented in section 4.3 and 4.4; the correlation analysis with large-scale climate change phenomenon PDO, PNA and ENSO will be presented and discussed in section 4.5.

Polar Lows are a phenomenon forming in the “cold season”; therefore the “Polar Low Season” (PLS) in the North Pacific is defined as the time from October through April the following year. This is a bit different from Zahn and von Storch (2008a): they define the PLS from July to next June. As we know

there are few Polar Lows taking place in summer, this October-April selection presents a smaller bias in Polar Low number statistics. The period of summer during May to September is not included. The PLS is addressed by the first and second year, for example the PLS 1950/1951 begins in October 1950 and ends April 1951. The statistical analysis excluded the first half year of 1948 and last half year of 2010, as they represent not a whole PLS. So we have 62 PLSs from 1948/1949 to 2009/2010.

4.1 General Characteristic of Climatology

Figure 4.1 shows the time series of the number of detected Polar Lows per PLS both without and with N-S criterion. By a quick overview, we have got a general idea of the tracking results under different criterions. The number without N-S criterion is only one third of the amount with N-S criterion. But their trends appeared similar. We conclude that the North-to-South direction criterion has little influence to the long term trend.

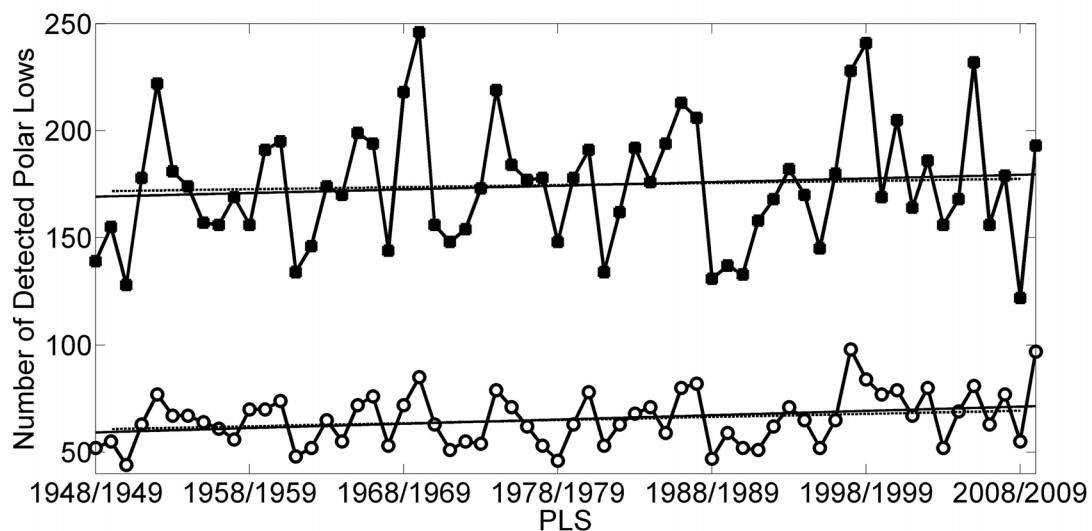


Figure 4.1 Number of detected Polar Lows in the North Pacific per PLS. The detected number of Polar Lows without N-S criterion (mark with ■). The solid line represents the trend from 1948/1949 to 2009/2010, which is 0.17 cases/PLS; the dashed line represents the trend from 1949/1950 to 2008/2009, which is 0.09 cases/PLS. The detected number of Polar Lows with N-S criterion (mark with ○). The solid line represents the trend from 1948/1949 to 2009/2010, which is 0.2 cases/PLS; the dashed line represents the trend from 1949/1950 to 2008/2009, which is 0.14 cases/PLS.

When looking only for cases **without a directional constraint of the movement**, a total of 10812 Polar Lows was detected by the tracking algorithm during the 62 PLSs. On average, 174 Polar Lows were found per PLS, with a strong year-to-year variability indicated by a standard deviation of 29 ($\pm 17\%$ of

the long term mean). The decadal variability is weak. The overall trend, from the first PLS in 1948/1949 to the last PLS in 2009/2010, in the frequency of Polar Low is positive with 0.17 cases/PLS, which yields about 11 Polar Lows more in the end than in the beginning of the series (11 cases corresponds to 6% of the long term mean). We have to point out that the slope of the trend depends on the number of cases of the first and last PLS. When disregarding the last and the first PLS, the trend of Polar Lows from PLS 1949/1950 to 2008/2009 is smaller, with only 0.09 cases/PLS.

For the result **with the N-S criterion**, fewer Polar Lows are detected, namely only 4052 Polar Lows during the 62 PLSs. On average, 65 Polar Lows were found per PLS, with a strong year-to-year variability indicated by a standard deviation of 12 ($\pm 18\%$ of the long term mean). Maximum number of detected cases is found in PLS 1997/1998 with 98 cases the minimum number is in PLS 1950/1951 with 44 cases. The overall trend, from the first PLS in 1948/1949 to the last PLS in 2009/2010, in the frequency of Polar Low is positive with, on average, additional 0.2 cases per PLS, which yields about 12 Polar Lows more in the end than in the beginning of the series (corresponding to 18% of the mean total). The trend of Polar Lows from PLS 1949/1950 to 2008/2009 is positive with 0.14 cases/PLS. When calculating 10 trends from 1948/1949 – 2009/2010, 1949/1950-2008/2009 to 1957/1958 – 2000/2001, the mean trend is 0.16 cases/PLS; the standard deviation of these 10 trends is 0.03/PLS – so that the estimate of the trend appears relatively insensitive to the early and late values.

There is no acceleration of a trend towards the end of the time series, as one would expect if a change due to anthropogenic climate change has emerged. Instead the trend seems mostly uniform and rather small. According to the pre-whitened Mann-Kendall trend test (Kulkarni and von Storch 1995), the 62-PLS-trend of the number of detected Polar Low is significant (5% risk; Table 4.1) for the configurations with directional constraint. The overall trend is 0.2 cases/PLS and the standard error for the M-K trend test is 0.09. With a t stat value of 2.73 and P value of 0.01, the trend is positive and significant. By a 5% risk, the lower confidence limit is 0.07 and the upper confidence limit is 0.39. But it is insignificant when examining the curve derived without directional constraint.

Table 4.1 Result of Mann-Kendall trend test for the time series of detected Polar Low number over 62 PLSs.

	trend	Std. error	t Stat	P-value	Lower 95%	Upper 95%
Time series with N-S criterion	0.2	0.09	2.73	0.01	0.07	0.39

The meso-scale synoptic lows usually moves from lower latitude northward in the North Pacific. Furthermore, the cold air outbreak which is favourable for Polar Low cyclo-genesis always takes a southward direction. Therefore less bias of detected Polar Low number is included when we adopte the N-S criterion. We have chosen the results with N-S criterion for further discussions.

The annual cycle of monthly numbers of detected Polar Lows exhibits a highest frequency in winter

with maxima in December and January and almost no Polar Low activity in summer (Figure 4.2) in consistence with the observation that Polar Lows form in the cold season. The error bars in Figure 4.2 represent the inter-annual variability of Polar Lows for every month. They are calculated by the standard deviation of time series of Polar Low numbers in every month over the 62 PLSs. The variability of Polar Low cyclo-genesis in the PLS from October to April is higher than in the other month of the year.

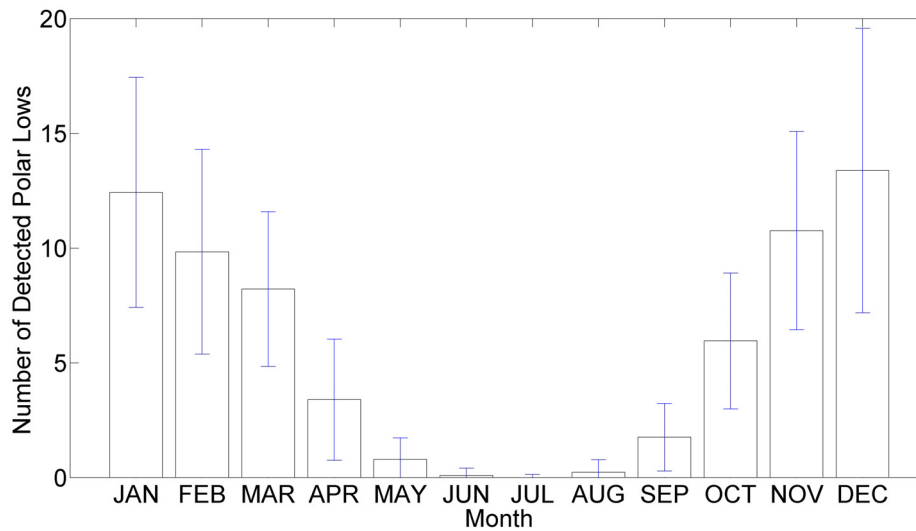


Figure 4.2 Mean number of detected Polar Lows per month for the whole 62 PLSs. Error bars represent the inter-annual variability of Polar Low numbers.

Furthermore, we determined the annual cycle of the days with Polar Lows during the same time period as Businger (1987), namely 1975-1983, and found our results consistent with Businger's results. We both share a highest frequency of Polar Lows activity during November to February, and a secondary maximum. The results differ with respect to the secondary peak in January in our 1975-1983 climatology, but in February in Businger's climatology (Figure 4.3). In view of the very different methods applied by us and by Businger, namely satellite observations vs. downscaled re-analyses, the differences may be considered acceptable. When examining the set of Polar Lows derived without the directional constraint, a very similar annual cycle, except for a uniform difference in the magnitude, is found (not shown).

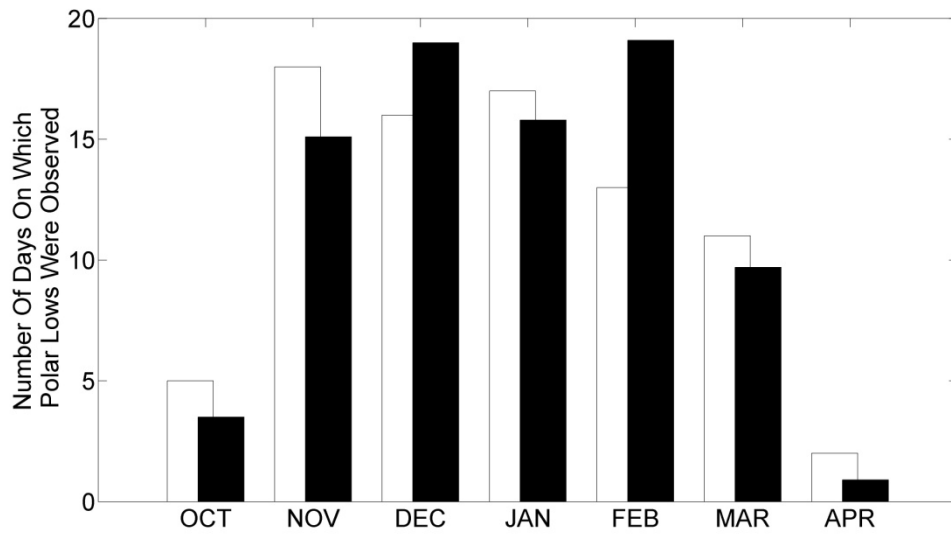


Figure 4.3 Histogram of the number of days per month on which Polar Lows were observed over the Gulf of Alaska or the Bering Sea during the period 1975-1983. White bar represents the result from our simulation and black bar represents results observed in satellite imagery (Businger, 1987).

In Figure 4.3 we show frequencies derived from the simulation results but only for the Polar Low seasons 1975-1983 as in Businger (1987), who analyzed counted Polar Lows in satellite images. The first half PLS from January to April in 1975 and the last half PLS from October to December in 1983 did not make a whole PLS.

Furthermore, we checked the duration of every detected Polar Low in the tracking result. Most of the Polar Lows (over 69%) have a life cycle less than two days (Figure 4.4). Businger (1987) also pointed out that most of the Polar Lows have a life time of less than 48 hours.

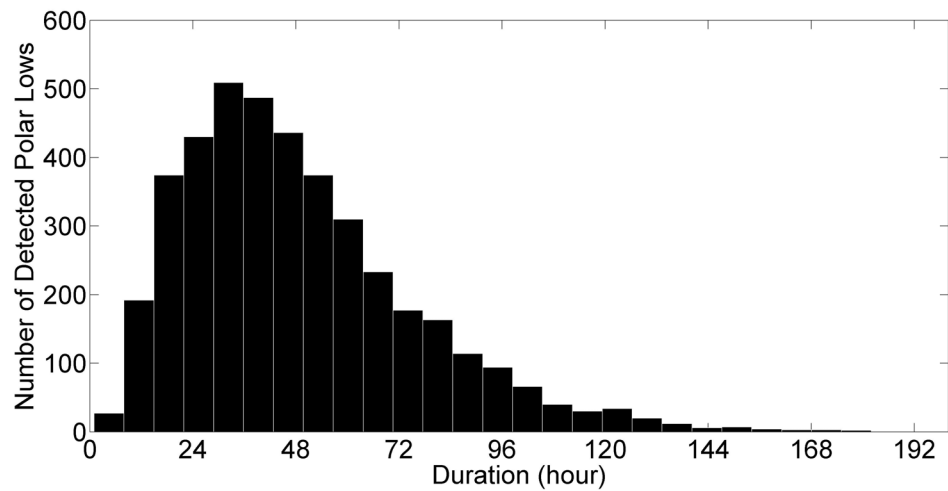


Figure 4.4 Histogram of the duration for all the Polar Lows detected in the tracking result for the 62 PLSs.

The spatial distribution of Polar Low frequency is shown in Figure 4.5a. The Polar Low frequency counts the occurrence per grid box of a first detection of a Polar Low. Highest frequencies are found in the region east of Japan in accordance with the finding of Yarnal and Henderson (1989b). By analyzing Defense Meteorological Satellite Program (DMSP) infrared imagery from 7 winter seasons, Yarnal and Henderson concluded that the most active Polar Lows form in the western extra-tropical North Pacific. Our peak area of Polar Low density is just off the east coast of Japan Island, while Yarnal and Henderson's result has its peak a little north, near the island of Hokkaido. In both analyses, there is much less Polar Low activity in the eastern North Pacific than in the western part.

Yarnal and Henderson pointed out that there are two bands that extend from northern Japan through the Kamchatka Peninsula into the western Bering Sea, another one extends eastward into the open waters of the North Pacific to just east of the International Date Line. Such two bands are also present in our climatology. Additionally, we find also high values for the Gulf of Alaska, where Yarnal and Henderson have detected only "a couple of small, weak pockets of formation".

4.1 General Characteristic of Climatology

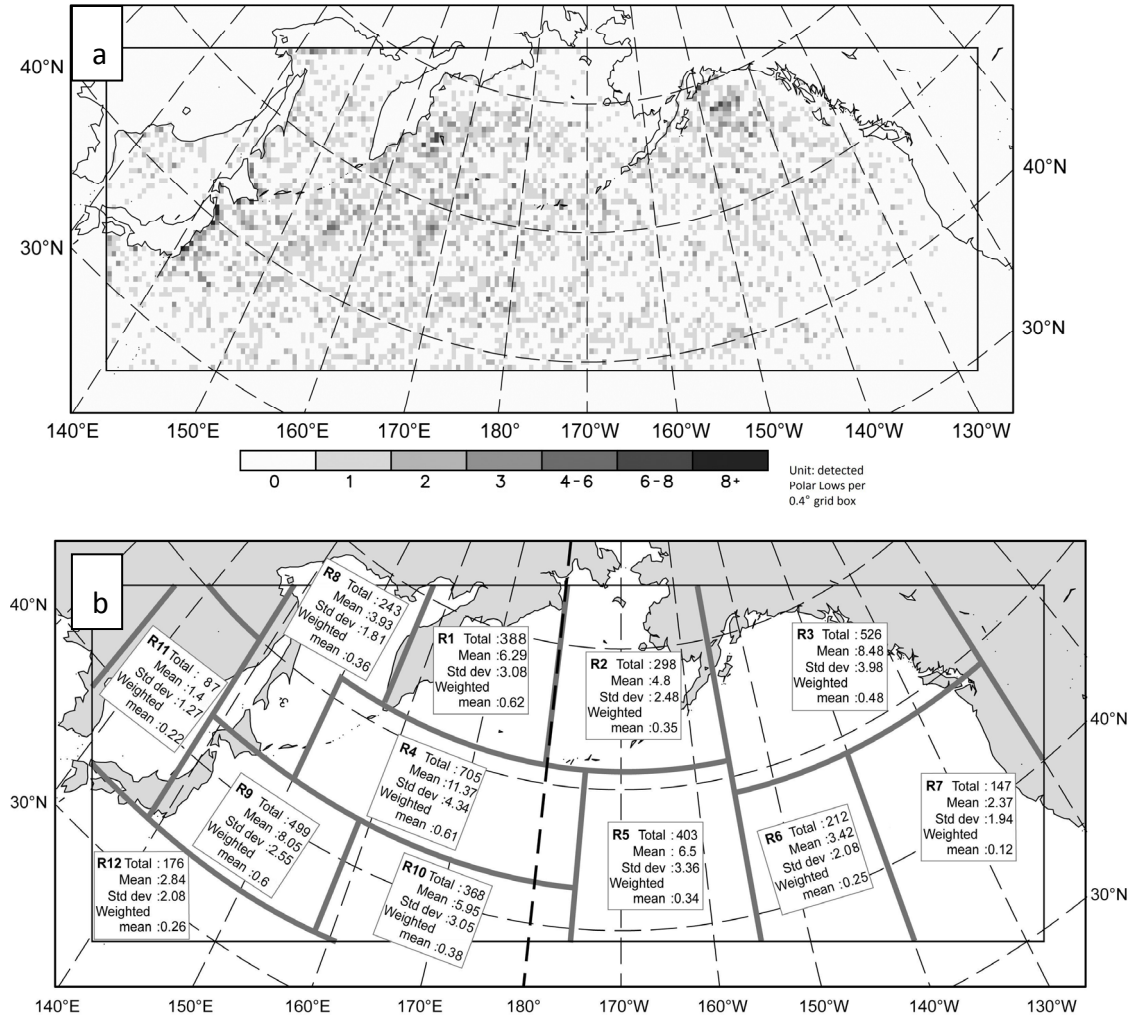


Figure 4.5 a) Polar Low frequency distribution. Unit: detected Polar Lows per 0.4° grid box. b) Sub-regions, for which the numbers of detected Polar Lows were aggregated (R1-R12) and respective number of detected Polar Lows (see text). Also given for each sub-region are mean number of Polar Lows per PLS (Mean), standard deviation (Std dev) and Polar Lows per area unit (Weighted mean). The latter number is divided by the sea grid points of corresponding sub-region.

For further analysis we divided the simulation area in 12 sub-regions and summarized the statistical values (Figure 4.5b). Generally, sub-regions R3, R4 and R9 have the highest total number of detected Polar Lows (526, 705 and 499) and the corresponding mean Polar Low distribution (with the mean detected number of 8.48, 11.37 and 8.05). These three sub-regions represent the southwest of Bering Sea, the Gulf of Alaska, band extends eastward into the North Pacific and east of Japan Island. No uniform year-to-year variability for Polar Low frequency in different sub-regions was found. R4 has the highest standard deviation of 4.34 and R11 has the lowest value of 1.27. R1, R3 and R5 also share a relatively higher year-to-year variability of 3.08, 3.98 and 3.36. We have to mention that some sub-regions also show a high standard deviation with a relatively lower Polar Low distribution. For

example: the standard deviation of R10 is 3.05 (larger than R9, 2.55), but the mean Polar Low number is only 5.95 (less than R9, 8.05).

For the density of Polar Low frequency, R1, R3, R4 and R9 still take the largest value of weighted mean (0.62, 0.48, 0.61 and 0.6). Detailed information of the area weighted mean year-to-year variability and trend of different sub-regions (for R1, R3, R4 and R9 with high density and R6, R7, R10, R11 and R12 with low density) are presented in Figure 4.6.

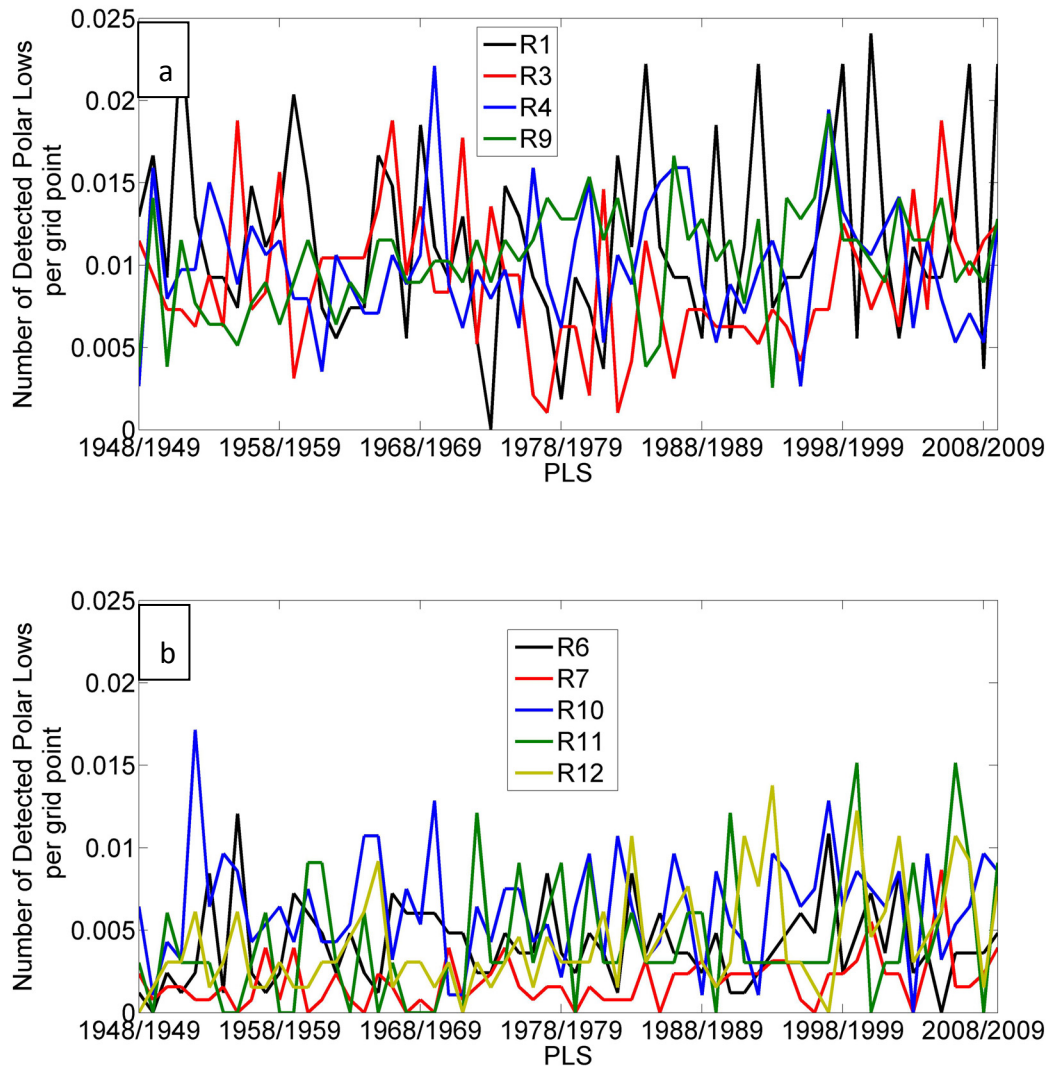


Figure 4.6 Time series of area weighted mean Polar Low number for sub-regions. a) presents R1, R3, R4 and R9; b) presents R6, R7, R10, R11 and R12. The weighted mean values are calculated by the detected number of Polar Lows divided by the sea grid points of corresponding sub-regions.

The time series of weighted mean Polar Low number in different sub-regions show a totally different

pattern of Polar Low formation over the North Pacific. The sub-regions with the highest density (R1, R3, R4 and R9) share a strong year-to-year variability of Polar Low frequency (Figure 4.6a) and relative strong trend. The strongest trend is from R9 with 14.4×10^{-5} cases per grid point per PLS. There is a decreasing trend of -1.7×10^{-5} cases per grid point per PLS in R3. R1 is 1.49×10^{-5} and R4 is 0.16×10^{-5} cases per grid point per PLS. For the sub-regions with less Polar Low formation (R6, R7, R10, R11 and R12), their time series show a relatively lower year-to-year variability (Figure 4.6b). Their trend is relatively weak compared to others (for example: 0.58×10^{-5} for R6, 0.35×10^{-5} for R10).

Generally, the trends are not uniform in the 12 different sub-regions. Here we are going to present the time series of detected number of Polar Lows from the highest Polar Low density sub-regions: the Gulf of Alaska (R3), the band to the southwest of Bering Sea (R4) and east of Japan Island (R9) in Figure 4.7.

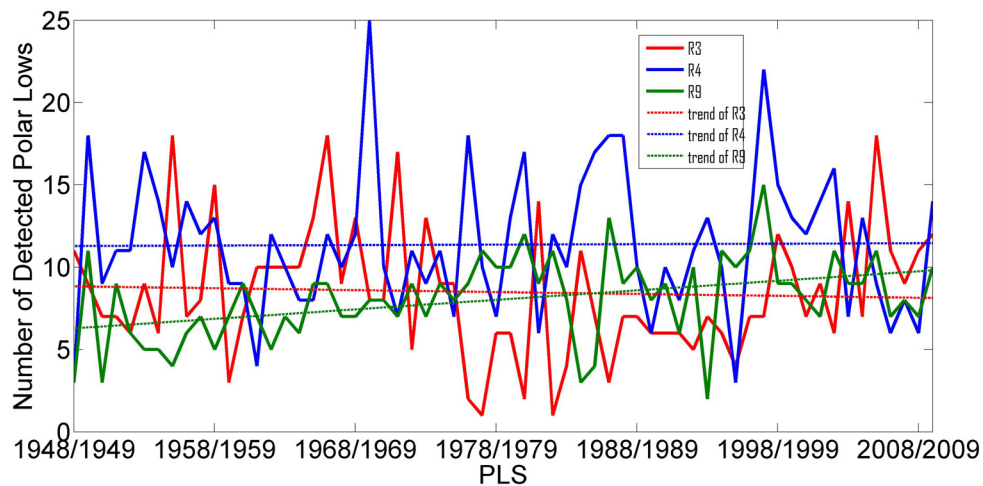


Figure 4.7 Time series of detected Polar Low numbers and the corresponding trend for the three different sub-regions with the highest frequency of Polar Low cyclo-genesis. Red represents the Gulf of Alaska (R3); Blue represents the band at southwest of Bering Sea (R4) and Green represents the east of Japan Island (R9). The solid lines represent the detected Polar Low number and the dashed represent the corresponding trend.

For the sub-region R3 in the Gulf of Alaska, appears a decreasing trend. The trend is -0.011 case/PLS. Numbers for the band to the southwest of Bering Sea (R4) is stable in time. The trend is nearly zero with a slightly increasing trend. R9 shows up a strong positive trend during the 62 PLSs in east of Japan Island. The value is round about 0.06 cases/PLS. Thus, in the western part of the North Pacific the number increases, whereas it decreases in the eastern part. This pattern is related to a changing large-scale atmospheric circulation in the North Pacific over the last 6 decades. A detailed discussion will be presented related to the large scale climate pattern such as PDO, PNA and ENSO in section 4.5.

4.2 EOF analysis of mean sea level pressure field

Before we investigate the linkage between Polar Low cyclo-genesis in the regional simulation and the large scale pressure pattern, some preparation work is needed. In order to exclude weather related noise of the data, we select the first 5 Empirical Orthogonal Functions (EOFs) analysis of the PMSL field and the tracking result. The result of EOF analysis of mean sea level pressure field will be discussed in detail.

Here we show two mean PMSL fields out of the 62 PLSs (Figure 4.8). They belong to the first and last PLS in the time series, which were 1948/1949 and 2009/2010.

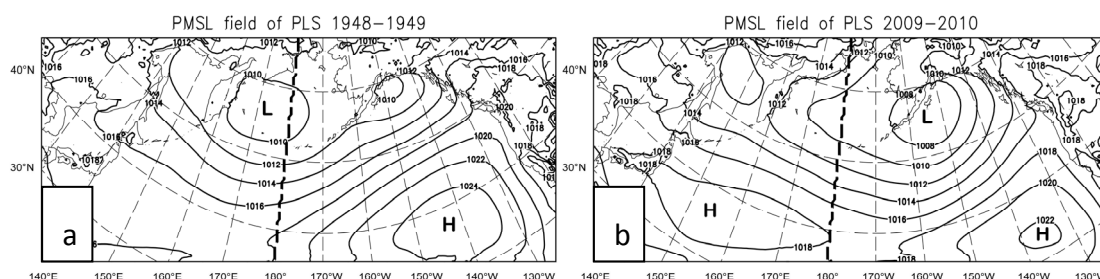


Figure 4.8 PMSL field of special PLS a) 1948-1949 and b) 2009-2010.

The general characteristic of mean sea level pressure field over North Pacific is obvious. There is a great and constant low pressure system forming around the Bering Sea, extending from the Kamchatka Peninsula to the Gulf of Alaska. The strength and region of this low system varies in detail under different PLS. The pressure over Eurasia, American continent and mid-latitude region of North Pacific is higher compared to pressure over marine middle latitudes. This climatology indicates that there must be southward flow from the polar region which is induced by the low pressure system. It transports the cold air from the polar region in the north to the open ocean. The SST there is relatively higher than in the Okhotsk Sea and Bering Sea due to the warm current called “Kuroshio” and North Pacific Drift. Great air-sea temperature difference is a favourable condition for Polar Low formation.

To apply the EOF analysis, the first step is to calculate the anomaly of the PMSL field. By removing the mean value of the 62 PLS, we obtain the anomaly field (Figure 4.9).

4.2 EOF analysis of mean sea level pressure field

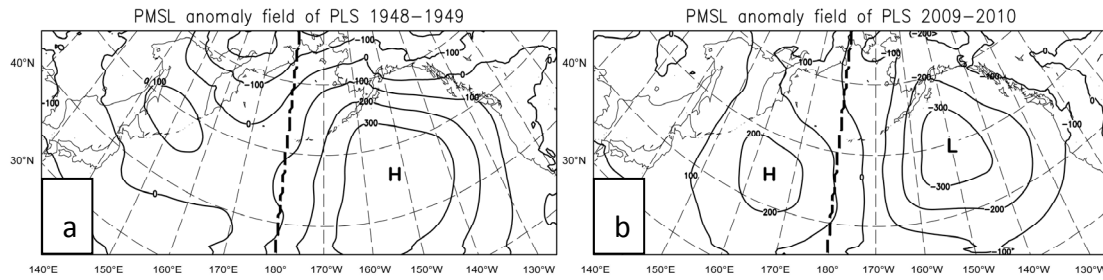


Figure 4.9 PMSL anomaly field of special PLS a) 1948-1949 and b) 2009-2010.

EOF analysis is a multivariate analysis technique for deriving the dominant patterns of variability from a statistical field. The general formula and concept of this analysis was presented in section 2.6. Here we show the first 5 pattern of the results and the corresponding time coefficient series (Figure 4.10). The first 5 takes 87% of the variance (Table 4.2).

By examining the corresponding time coefficient series, we find that EOF 1 pattern dominates the PLS of 1969/1970, 1975/1976, 1980/1981, 1982/1983 and 1997/1998, which takes 52% of the total variance. During these PLSs, the first EOF pattern dominates the North Pacific PMSL anomaly field. The center of this higher anomaly forms around the south of Aleutian Islands. The opposite situation, with large negative EOF coefficients, occurs during PLS 1948/1949, 1960/1961, 1971/1972 and 2008/2009.

The second EOF pattern has a negative anomaly over the Bering Sea. The PMSL field over the North Pacific has been dominated by this pattern under the PLS 1948/1949, 1954/1955, 1976/1977, 1997/1998 and 1998/1999. The largest converse pattern can be found in 1995/1996.

In order to verify the EOF result, we reconstructed the PMSL anomaly field from the first 5 EOF results. The same PLSs are presented (Figure 4.11).

4.2 EOF analysis of mean sea level pressure field

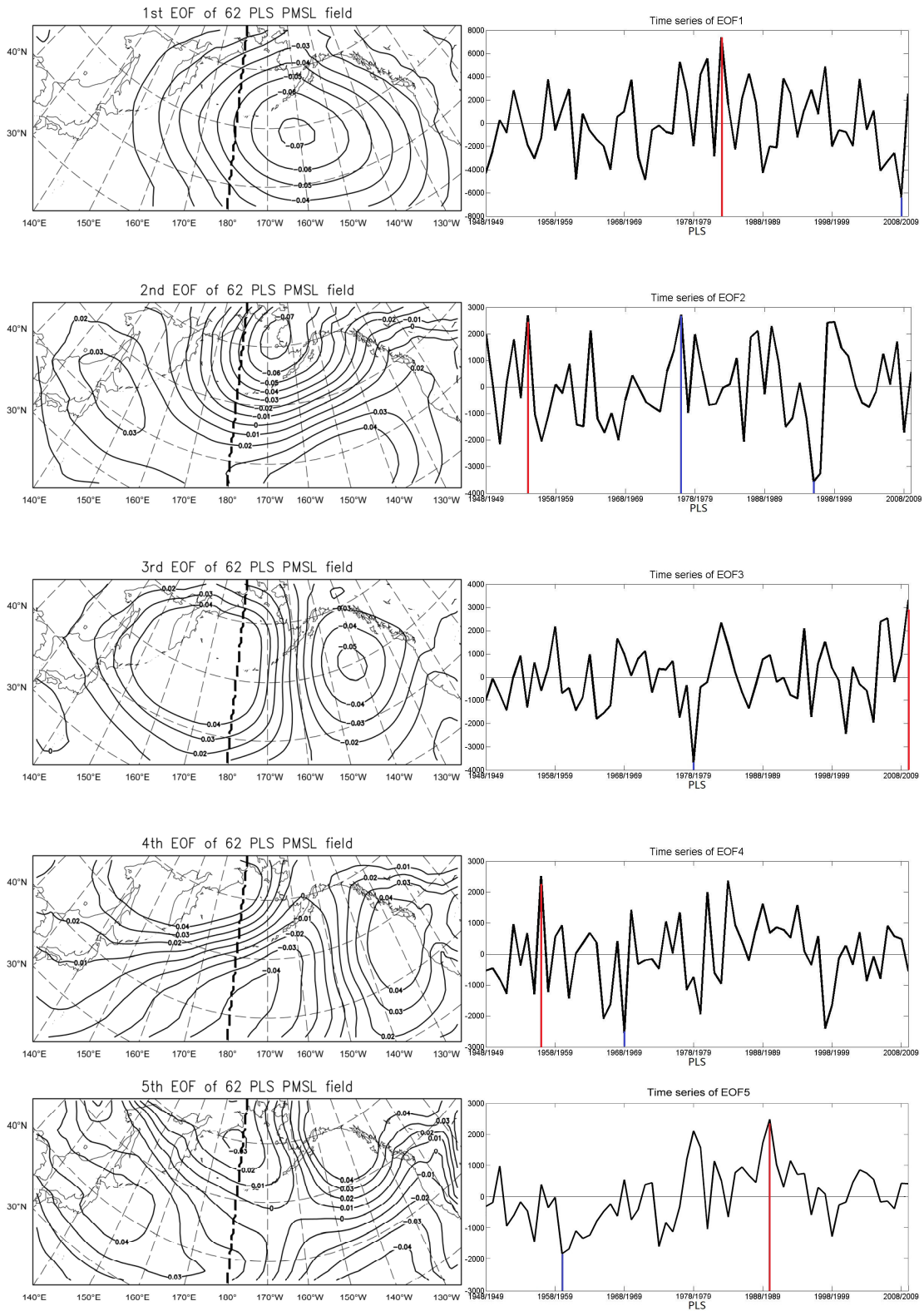


Figure 4.10 The first 5 EOF patterns of the PMSL field and the corresponding time coefficient over 62 PLSs. Red lines indicate the corresponding PLS of maximum time coefficient, blue lines indicate the minimum PLS.

Table 4.2 The single variance and accumulated variance of the first 5 mode EOF results.

	Single	Accumulated variance
1	51.88%	51.88%
2	12.91%	64.78%
3	10.10%	74.88%
4	7.20%	82.08%
5	5.22%	87.30%

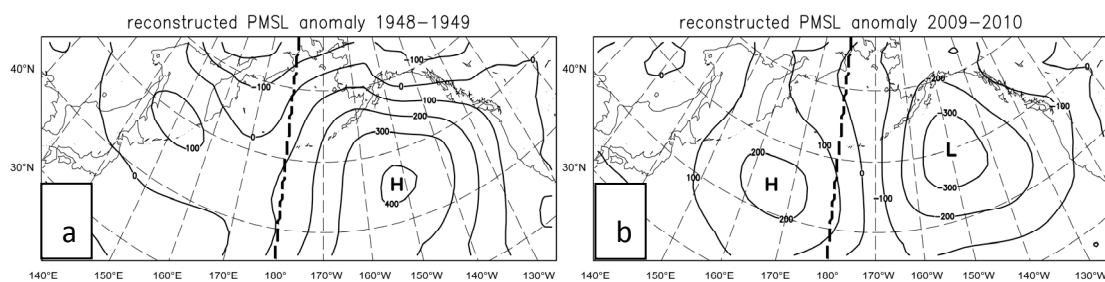


Figure 4.11 Reconstructed PMSL anomaly field of special PLS a) 1948-1949 and b) 2009-2010.

By comparing the original and reconstructed anomaly field, we found that the original field is well reconstructed by the first five EOFs. The isolines are smoother than the original data, which indicated that weather related noise had been reduced.

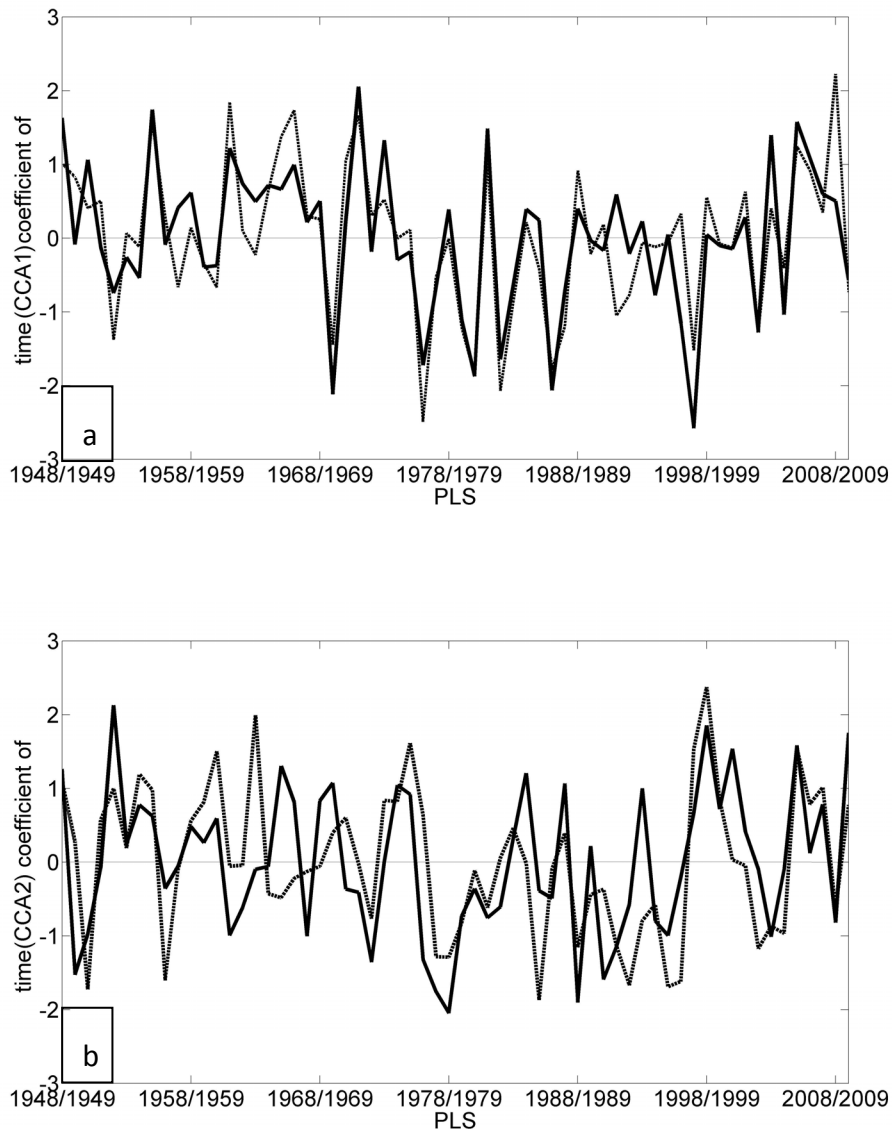
4.3 Linkage of Polar Low distribution with large-scale sea level pressure pattern

We begin with investigating how **PMSL** fields, averaged over a PLS, are related to the distribution of the numbers of Polar Low occurrences in that season. Here we emphasize that the analysis is not about short term synoptic situation or the instantaneous air pressure field directly related with the probability of a Polar Low to form. Instead we compare two statistics during the same PLS, namely the geographical distribution of Polar Lows, aggregated to the twelve sub-regions shown (Figure 4.5b), and the gridded time mean PMSL field.

The correlation analysis between PMSL and the number of Polar Lows is applied by Canonical

Correlation Analysis (von Storch and Zwiers 1999). CCA is a method to calculate correlation between two multidimensional sets of variables. To exclude weather related noise in each set we projected the full fields on the first 5 Empirical Orthogonal Functions (EOFs) of the Polar Low time series (representing 77% of the variance) and of the PLS-mean PMSL (87% of the variance). Prior to the CCA, the long term mean field is subtracted, i.e., the analysis is done with anomalies.

Figure 4.12 shows the resulting time series and spatial patterns of the two most important linkages between the regional distribution of Polar Lows and the time-mean PMSL field.



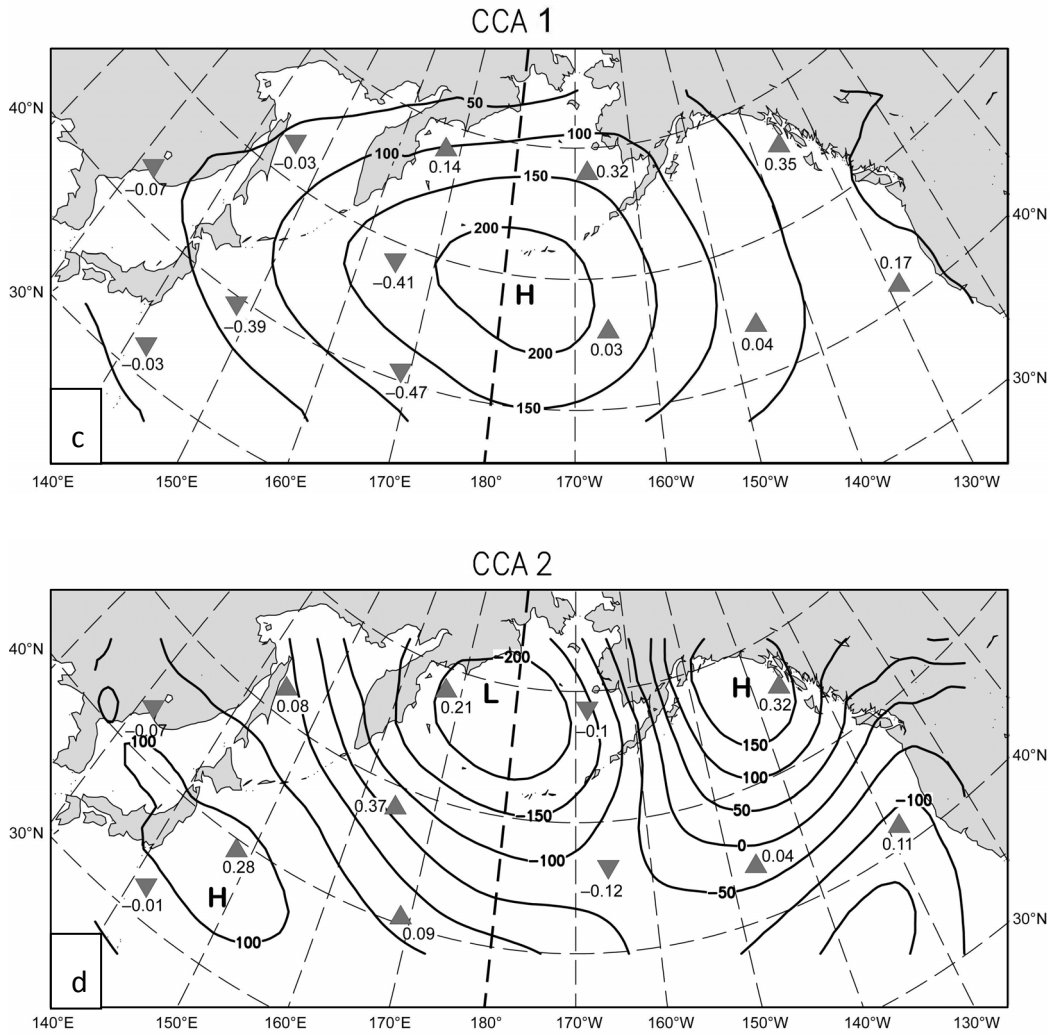


Figure 4.12 First 2 Canonical coefficient time series (a and b, dashed lines represent the Polar Low occurrences and the solid lines represent the PMSL pattern) and corresponding correlation patterns between regional time series of Polar Low occurrences per PLS in sub-regions R1-R12 (\triangle for positive values, ∇ for negative values) and mean sea level pressure fields in Pa. The first CCA pair (Figure 4a and 4c) shares a correlation coefficient of 0.89. The second CCA pair (Figure 4b and 4d) shares a correlation of 0.72.

The first Canonical pattern (CCA1, Figure 4.12c) describes a uni-polar pressure distribution. When the CCA coefficient (CCA1, Figure 4.12a) is positive then on average there will be eastward cold air flow across the Bering Sea and southeastward across the Gulf of Alaska, and consistently, more Polar Lows in that region (upright triangles).

These time mean flows are characteristic for more or less, short term marine cold air outbreaks in these regions. It is indicated that there is a close relationship between Polar Low formation and the presence of a trough in winter over East Asia and the nearby North Pacific (Businger 1987). The strong land-sea thermal contrast along the marginal ice zone pulls cold continental polar or Arctic air over the

Bering Sea and the Japan Sea. The relatively warm waters in the open ocean lead to the formation of Polar Lows through convective instability and baroclinicity.

When CCA1 has a negative coefficient, the pattern reverses sign, and a cold southeastward flow takes place over the western part of the Pacific, while the southerly warm anomaly flow emerges in the East. Accordingly, there are more Polar Lows in the West and less in the East as in the PLS 1969/1970, 1976/1977 and 1997/1998.

The time series of Canonical Correlation coefficient (Figure 4.12a and b) explains the variability of the two fields of variables over the 62 PLS. Dashed lines represent the pattern of Polar Low occurrence over the 12 sub-regions. The solid lines represent the PMSL pattern. By examining the time series in Figure 4.12a, it is found that CCA1 dominates in PLSs of 1954/1955, 1971/1972 and 1981/1982.

The second Canonical pattern (CCA2, Figure 4.12d) shows a mainly bipolar pressure distribution – there is a negative anomaly (below -2 hPa) on the Bering Sea at the same time as two positive anomalies on the Gulf of Alaska and Japan Island (over 1 hPa). Consequently, there will be a south-eastward flow starting from Siberia, across the Sea of Okhotsk, and then the south-west of Bering Sea where the western part of sub-region R4, and consistently more Polar Lows are detected there on average. A time mean pressure contrast of about 3 hPa between the Bering Sea and the west and east part of North Pacific (the region around Japan Island and the west coast of North American continent), is associated with more Polar Lows in the corresponding regions (R1, R3, R4 and R9).

By examining the time series in Figure 4.12b, we found that CCA2 dominates the years of 1951/1952, 1975/1976 and 1998/1999, which means there were more Polar Lows in region R1, R3, R4 and R9; also a negative sign in 1949/1950 and 1978/1979 with remarkably less Polar Lows in these regions.

To determine the relative importance of the two CCA-patterns, we have built for each sub-region R1-R12 a regression model, of the form $PL_i(t) = a_{0,i} + a_{1,i} \times CCA_1(t) + a_{2,i} \times CCA_2(t) + \varepsilon$. Here, $PL_i(t)$ is the number of Polar Lows in season t and in sub-region i ; $a_{0,i}$, $a_{1,i}$ and $a_{2,i}$ are the regression coefficients, which are determined by a least square fit, $CCA_1(t)$ and $CCA_2(t)$ are the CCA coefficients of patterns 1 and 2 in season t , and ε is the residual, the unexplained part. In Figure 4.13 we list the coefficients for every sub-region.

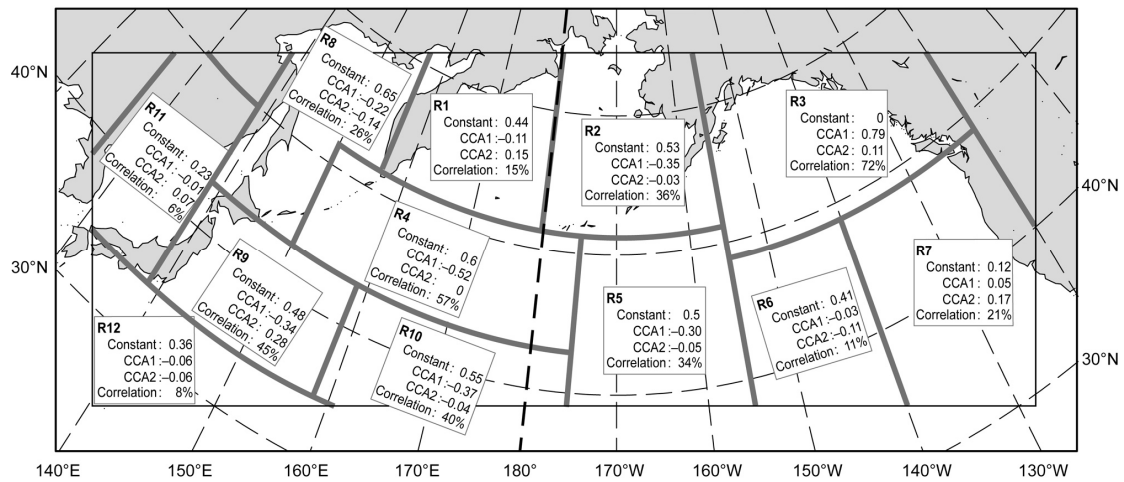


Figure 4.13 Result of multiple regression analysis of number of Polar Lows in sub-regions R1-12, as given in Figure 4.5b, and of time coefficient series of mean sea level pressure pattern of the first two pattern of CCA result (Figure 4.12a,b).

The two series, $CCA_1(t)$ and $CCA_2(t)$ are about equally important, when counting how often $|a_1(t)| > |a_2(t)|$. They are particularly successful to describe the variability in all but one of the highest frequency occurrence area (shown in Figure 4.5) – for sub-regions 3, 4, 9 and 10, the correlation is over 40%, while in the far eastern (sub-region 6 and 7) and western (11 and 12) the correlations are less than 25%. When comparing with Figure 4.5b, we see that the frequency of occurrence of Polar Lows in the sub-regions 6, 7, 11 and 12 is relatively low: the mean number of Polar Lows in 7, 11 and 12 together is 6.7 per PLS, while the occurrences in each of sub-regions 3, 4, 9 and 10 separately is of about that intensity. In sub-region 1 the frequency of occurrence is very high but the correlation is low (15%).

Since the two CCA pairs CCA1 and CCA2 have rather similar correlation coefficients (0.89 and 0.72), they maybe degenerate (von Storch and Zwiers 1999). In that case any orthogonal rotation of the patterns yields a similarly good description of the link between seasonal mean air pressure and the regional distribution of Polar Lows. Polar Low occurrences and mean PMSL exhibit a common co-variability in a two-dimensional space, which is spanned by the two CCA patterns. Therefore, any linear combination of the two patterns, both for pressure and number of Polar Lows is equally good in describing the co-variability. Such linear combinations may be expressed by introducing:

$$CCA(x) = \cos(x) * CCA1 + \sin(x) * CCA2$$

with x is varying from 0 to 2π . Then any pair $CCA(x)$ and $CCA(x + \pi/2)$ forms a pair of CCA-pattern carrying the about same information as CCA1 and CCA2.

Figure 4.14 shows $CCA(x)$ for $x=0, \pi/6, \pi/3, \pi/2, 2/3\pi, 5/6\pi$ and π , which stands for rotations by $0^\circ, 30^\circ,$

60°, 90°, 120°, 150° and 180°. Combinations with $x > \pi$ can be derived through, $CCA(x+\pi) = -CCA(x)$, so that we show only combinations for $0 \leq x \leq \pi$. $CCA(0)$ is CCA1, $CCA(\pi/2)$ is CCA2, and $CCA(\pi) = -CCA1$.

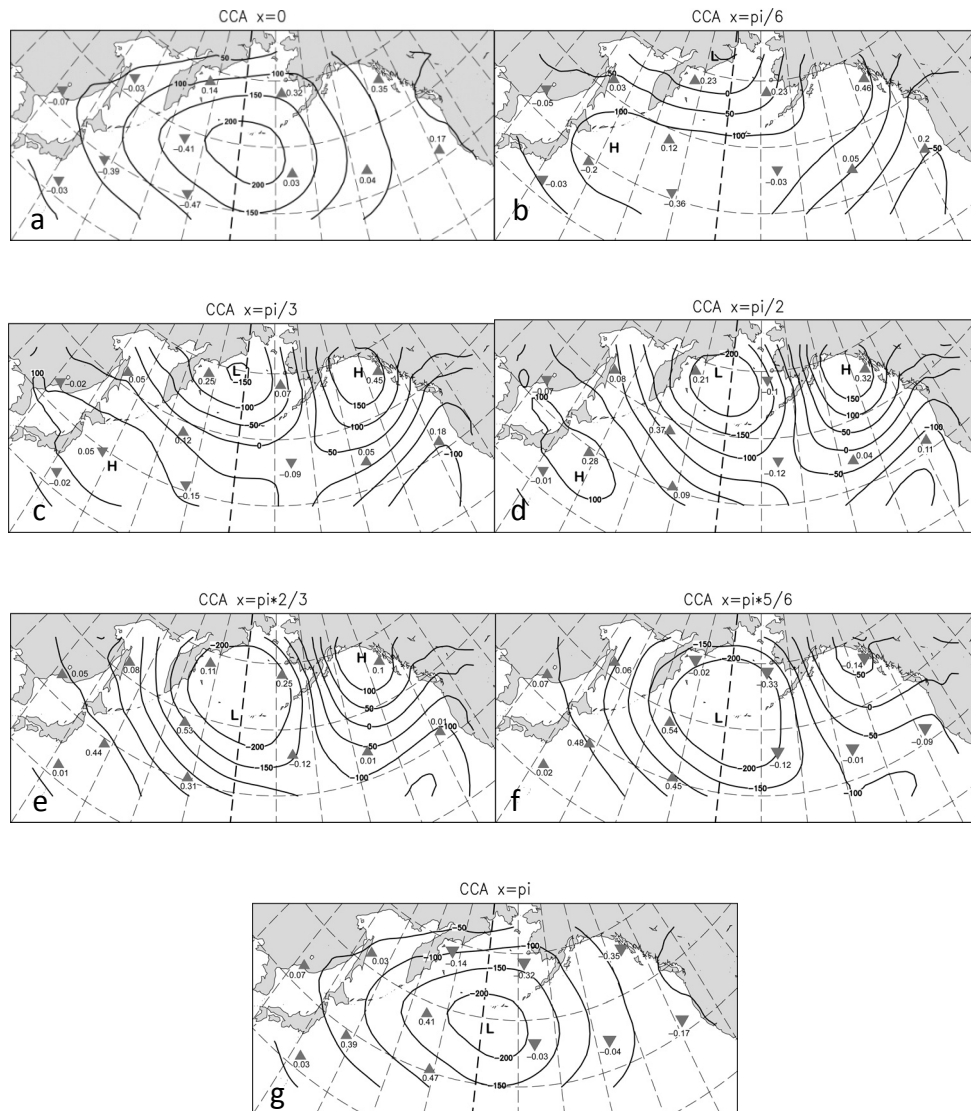


Figure 4.14 Orthogonal rotations of CCA1 and CCA2 (see Figure 4.12). a) $x=0^\circ$, b) $x=30^\circ$, c) $x=60^\circ$, d) $x=90^\circ$, e) $x=120^\circ$, f) $x=150^\circ$, g) $x=180^\circ$.

The result of this exercise is that the resulting different patterns show almost the same types of structures and of linkages. The CCA patterns of PMSL over the North Pacific area, most of them appear uni- or bimodal and of large scale. More Polar Lows occur in currents flowing off cold regions, and less Polar Lows when the air flow anomaly is directed towards cold regions.

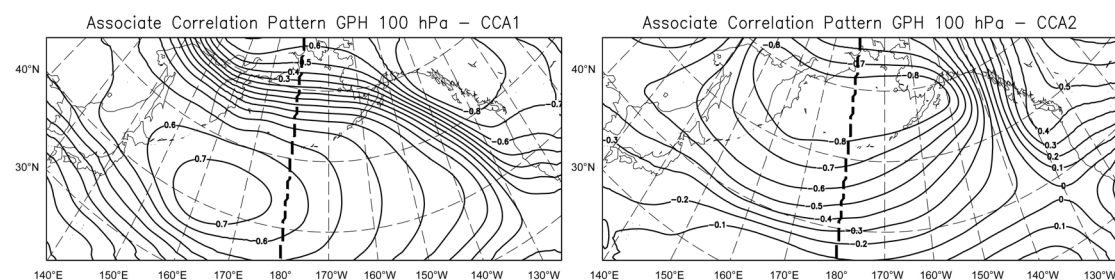
4.4 Linkage of Polar Low occurrence with upper layer and sea surface

Next, we examine the link to time-mean distribution throughout the troposphere, from sea surface to the lower stratosphere. To do so, we derive Associated Correlation Pattern (von Storch and Zwiers 1999) to describe the linkage between multi-decadal Polar Low characters and geo-potential height at different pressure levels.

Associated Correlation Patterns are designed to describe the relationship between time series of an “index” variable and a physical field. The first set of Associated Correlation Pattern was applied between the detected Polar Low number (Figure 4.1) and the seasonal mean geo-potential height field over the 62 PLSs. By calculating the correlation coefficient between the time series of CCA coefficient for Polar Low occurrence pattern (dashed lines in Figure 4.12a and b) and the time series of geo-potential height anomalies for each grid point on each level, we derive typical configurations on every pressure level associated with the two Polar Low patterns shown in Figure 4.12c and d (the triangles). The anomalies were formed by subtracting the time mean fields for the 62 considered PLSs.

The maps of correlation coefficients (Figure 4.15) present similar patterns to the corresponding PMSL field of the CCA results (Figure 4.12c and d; isolines). It indicates that the relationship between the atmosphere circulation and Polar Low occurrence is mostly barotropic, even if in the lower stratosphere of 100hPa the pattern is shifted somewhat. The cold flow which inducing the Polar Low occurrence is uniform throughout the troposphere, from sea level to the upper troposphere and the lower stratosphere.

On the upper levels at 100, 300, 500 and 700 hPa, the isolines are smoother. On the lower level at 850 and 1000 hPa, the isolines are getting wigglier: the orography and sea surface temperature attain a stronger influence on the generation of more or less Polar Lows.



4.4 Linkage of Polar Low occurrence with upper layer and sea surface

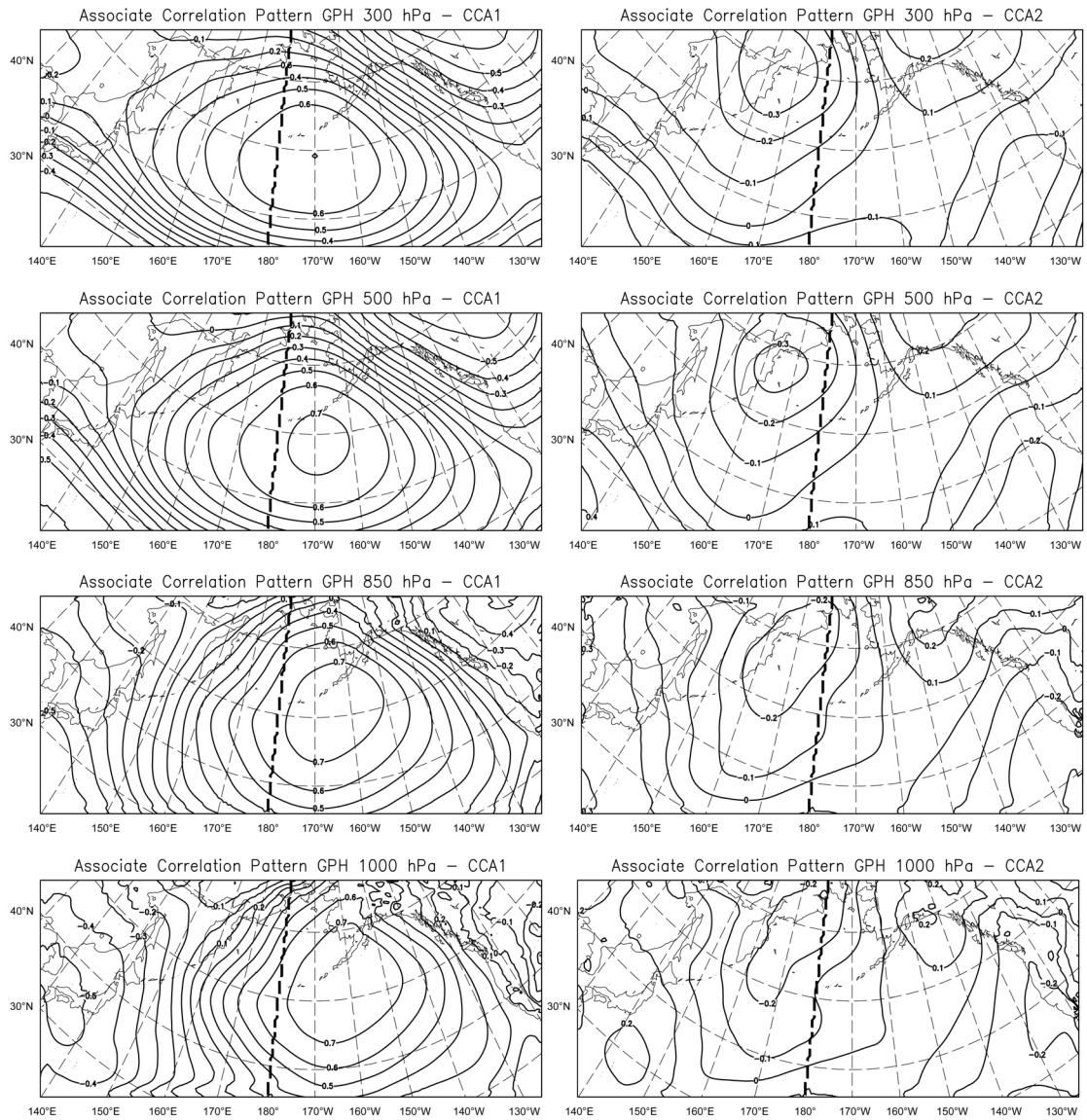


Figure 4.15 Associated Correlation Pattern between time series of geo-potential height over 62 PLS and time coefficient of the Polar Low occurrence from the first two CCA patterns (1st CCA pair, left column, 2nd right column). From top to bottom 100, 300, 500, 700, 850 and 1000 hPa. All variables are averaged across a PLS, i.e., from October to April.

In order to investigate the link with SST respective sea ice temperature in case of ice, a pair of Associated Correlation Pattern is presented (Figure 4.16) to describe the linkage between the CCA-time series of the Polar Low occurrence (dashed lines in Figure 4.12a and b) and the surface temperature. These temperatures were taken from the same NCEP 1 re-analysis, which was used to force the regional model simulation.

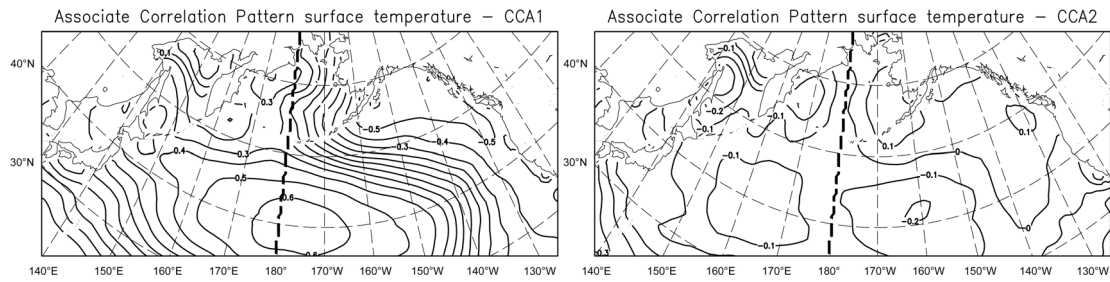


Figure 4.16 Associated Correlation Pattern between time series of ocean surface temperature over 62 PLS and time coefficient of the Polar Low occurrence from the first two CCA patterns (1st CCA pair, left column, 2nd right column). All variables are averaged across a PLS, i.e., from October to April. The surface temperature was taken from the NCEP 1 re-analysis data, over the ocean. In case of no ice it indicates the SST, else it indicates the ice surface temperature.

Both Associated Correlation Patterns of SST are consistent with the flow patterns of the CCA result. Temperatures tend to be lower, where more cold air is advected, and higher than on average, when the flow advects less cold or more warm air. Previous modeling studies have shown that the mechanism behind these patterns is that of an oceanic response to anomalous flow (Luksch et al. 1990; Luksch and von Storch 1992), first suggested by (Bjerknes 1964) for the Atlantic. We conclude that anomalous mean flow is responsible for both, the formation of anomalous SST as well as the formation of more, or less Polar Lows, in the North Pacific.

4.5 Long term correlation analysis

The detected Polar Low number for the last 62 PLSs has been presented in the first section of this chapter. On the one hand, we have found that there is an increase trend during the last 6 decades over the North Pacific. But the mechanism of this increase trend is still unclear. In order to investigate the mechanism of the increase Polar Low trend we discuss the correlation between the time series of detected Polar Low number and several climate change phenomenon, such as Pacific Decadal Oscillation (PDO), Pacific-North American tele-connection pattern (PNA) and El Niño/La Niña-Southern Oscillation (ENSO). For PDO, the mean global average SST anomalies are removed to separate the pattern of variability from any global warming signal.

4.5.1 Pacific Decadal Oscillation

The Pacific Decadal Oscillation (PDO) is a pattern which describes the Pacific climate variability on a long time scale. The shift phases are represented as warm or cool surface waters in the Pacific Ocean north of 20°N. For the warm or positive phase, the sea surface temperature (SST) shows a relative

negative anomaly over the west Pacific and part of the eastern ocean warms with a positive SST anomaly. It is represented as an opposite pattern during the cool or negative phase (Figure 4.17).

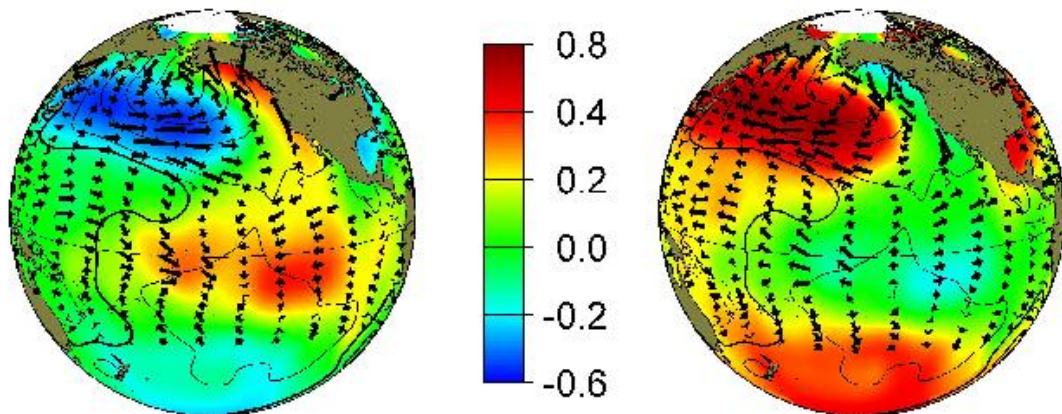
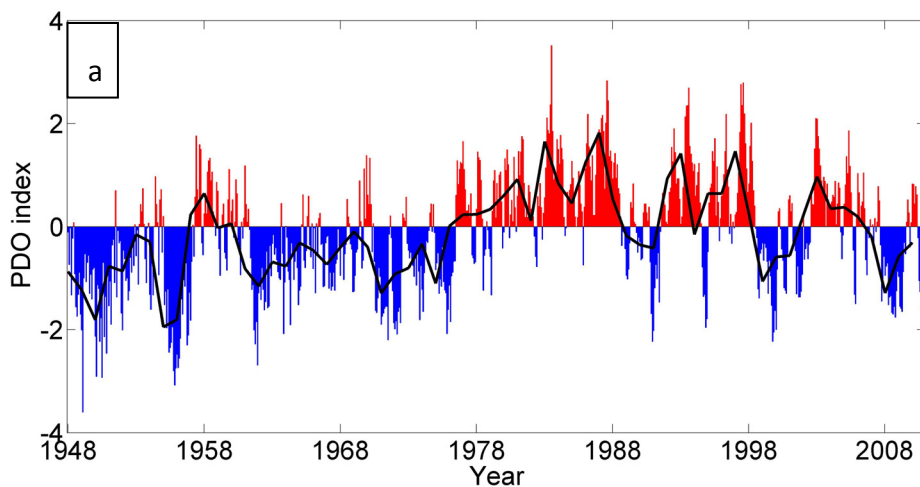


Figure 4.17 The anomaly of typical wintertime sea surface temperature (SST) (colors), sea level pressure (contours) and surface windstress (arrows) during the warm and cool phases of PDO. (Mantua 2000)

The PDO is in terms of the spatial patterns is similar to the El Niño-like pattern, but behaves totally different in time. The PDO persists in a positive or negative phase for about 30 years. Four such phases of the PDO pattern have been found in the last 20th century. The cool PDO pattern lasted from 1890-1924 and 1947-1976, while the warm PDO pattern prevailed from 1925-1946 and 1977 until the late 1990s.

The PDO index is offered as monthly SST anomalies. As we discussed at the beginning of this chapter, we have investigated the Polar Low issue under the definition of “PLS”. So the corresponding PDO index in every PLS is calculated by the sum of PDO indices from October to next April (Figure 4.18).



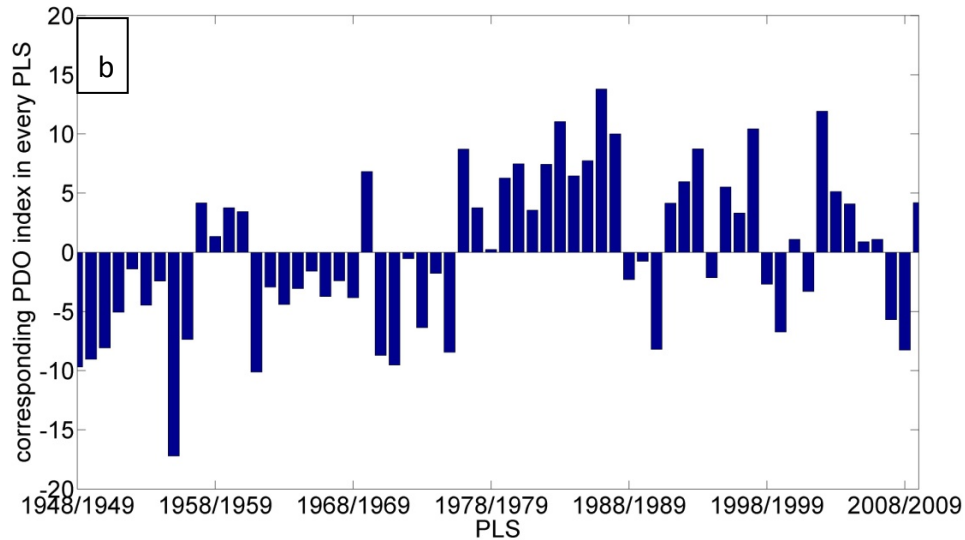


Figure 4.18 Time series of PDO index. a) monthly PDO index from 1948 to 2010 by Mantua(2000), solid line represents the yearly mean PDO index, blue and red bars represent the monthly PDO index, blue for negative and red for positive; b) corresponding PDO index in every PLS.

Polar Low is a product caused by the air-sea interaction. As we argued before, when a cold flow outbreaks from the polar region, cold air meets the warm ocean water in the south, and the resulting instability leads to the cyclo-genesis of Polar Lows. So, when the sea surface temperature (SST) is warmer, it is more favorable for Polar Low formation which indicates the frequency of Polar Low formation should be increase. On the opposite side, lower SST may be associated with a decrease of Polar Low formation.

By the discussion about the different PDO pattern in the last 20th century from last paragraph, we have found that most region of the northwest Pacific was dominated by a relatively cool sea surface temperature (SST) during 1947-1976. On the other hand, after 1976, the positive phase took part during 1976 until late 1990's. The SST in the west region of west Pacific is warmer. All the regions with high frequency of Polar Low cyclo-genesis had been covered except the Gulf of Alaska. This might be one of the reasons for the increase Polar Low frequency over the North Pacific. It will be discussed in detail in section 4.5.4.

4.5.2 Pacific – North American tele-connection

The Pacific-North American tele-connection pattern (PNA) is a climatological term to describe an important large-scale weather pattern over the Pacific Ocean and the North American Continent. It represents different states of the atmospheric circulation over the Pacific-North American continent region.

For the positive mode of the PNA pattern, relatively higher air pressure surrounds the vicinity of Hawaii and the intermountain region of North America, while below-average values have been found south of the Aleutian Islands and over the southeastern American. This pressure pattern associated with an enhanced East Asian jet flow. Conversely, the negative pattern is associated with a westward retraction of the jet stream towards eastern Asia. The activity over the high latitude region of the North Pacific is blocked and there are strong split-flow forms over the central North Pacific.

The PNA index is presented as normalized monthly mean geo-potential height values (Figure 4.19a). As we discussed at the beginning of this chapter, we have investigated the Polar Low issue under the definition of “PLS”. So the corresponding PDO index in every PLS was calculated by the sum of PNA index from October to next April (Figure 4.19b).

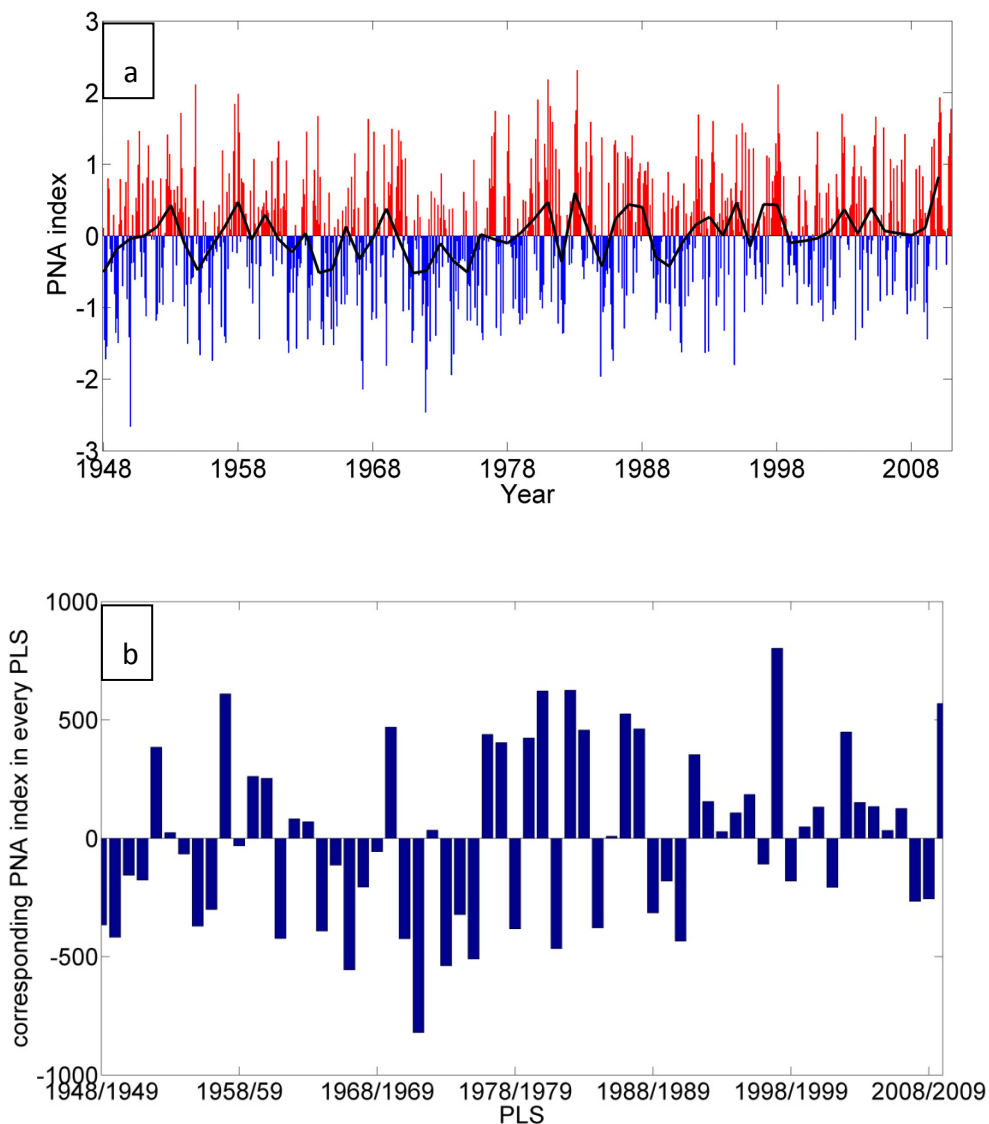


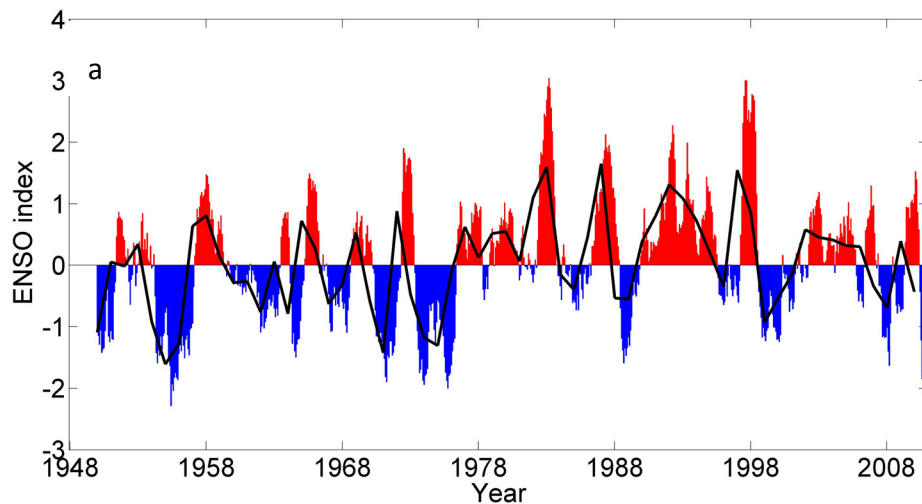
Figure 4.19 Time series of PNA index. a) normalized monthly PNA index from 1948 to 2010 (Wallace and Gutzler

1981), solid line represents the yearly mean PNA index, blue and red bars represent the monthly PNA index, blue for negative and red for positive; b) corresponding PNA index in every PLS.

The circulation of atmosphere in the upper level over the North Pacific is also important for the formation of Polar lows. When the eastward flow dominates the North Pacific, more cold air will be brought from Siberia, Eurasia continent, more Polar Lows cyclo-genesis over the North Pacific. When the negative mode takes place, blocking activity over the high latitudes would be an unfavorable condition for Polar Low formation. The investigation of long term variability of atmosphere circulation over the North Pacific is very helpful to understand the trend of Polar Low frequency on a multi-decadal time scale. It will be discussed in detail in the coming section.

4.5.3 El Niño-Southern Oscillation

The El Niño-Southern Oscillation is a global climate pattern which mostly forms over the tropical Pacific Ocean. An El Niño event, as well as the opposite, a La Niña event, extends normally across one year. The SST exhibits as a warming pattern in El Niño events and cooling for La Niña events over the tropical eastern Pacific Ocean. The air surface pressure is higher than normal in the western Pacific during a warm event, and lower in a La Niña cold phase. The monthly ENSO index MEI is shown during 1950 – 2100 in Figure 4.20a. We calculated the responding MEI for every PLSs (Figure 4.20b).



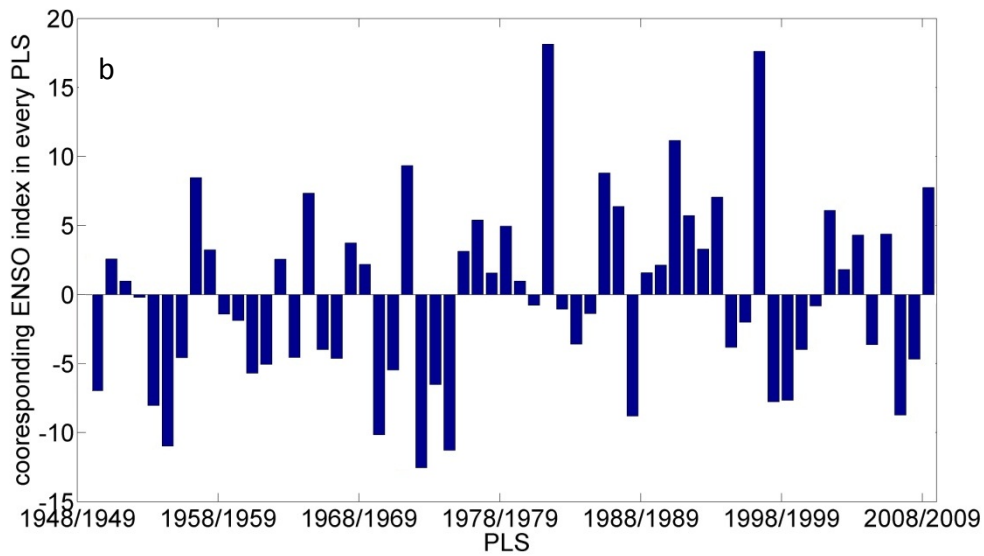


Figure 4.20 Time series of ENSO index. a) normalized ENSO index from 1950 to 2010 (ENSO: Multivariate ENSO Index, see <http://www.esrl.noaa.gov/psd//people/klaus.wolter/MEI/table.html>), solid line represents the yearly mean MEI, blue and red bars represent the monthly MEI, blue for negative and red for positive b) cooresponding MEI index in every PLS

4.5.4 Discussion

In order to investigate the large scale dynamical environment of changing Polar Low occurrences, we analyze the correlation between the time series of detected Polar Low number and several climate variability indices, namely the PDO, PNA and ENSO.

The normalized time series of detected Polar Low number and three indices are presented in Figure 4.21. Firstly, the correlation coefficient of detected Polar Low number with PDO index is 0.39, with PNA index is 0.45, with ENSO index is 0.22. It indicates that the Polar Low formation over the North Pacific has a highest relationship with PNA and PDO. There is limited influence by ENSO. As the Polar Low is a weather phenomenon caused by the air-sea interaction, the coupled SST and atmosphere circulation over the North Pacific both plays important role for the formation of Polar Lows. We are going to discuss the variability of SST and upper circulation over the last 6 decades. The potential relationship between them will be investigated. The SST variability will be discussed related to the PDO pattern. The atmosphere circulation is associated with PNA index series.

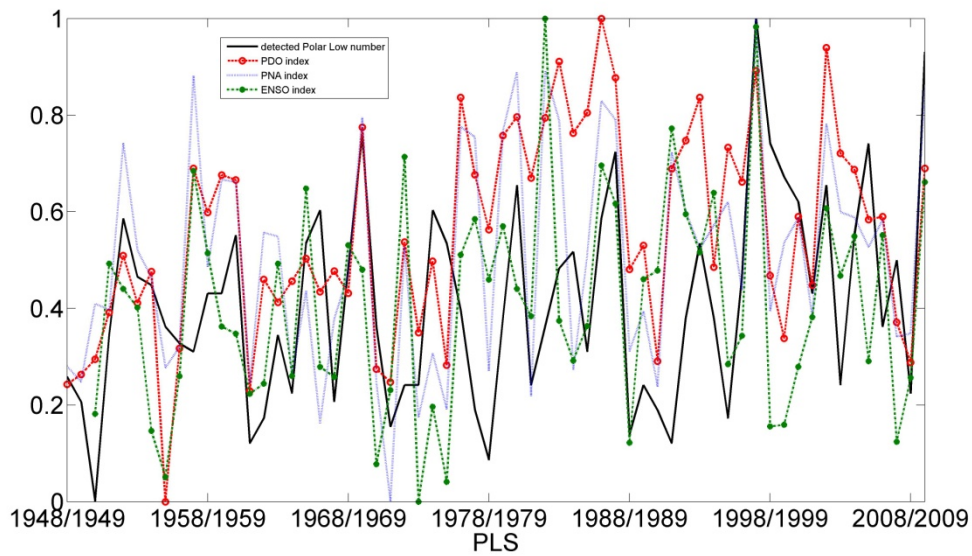


Figure 4.21 Time series of normalized detected Polar Low number (black line), PDO index (red, with mark o), PNA index (blue, dash) and ENSO index (green, with mark *)

The overall trend for the time series of PDO index (Figure 4.18b) is positive. It indicated that the general SST anomaly over the North Pacific is increasing. The Polar Low was caused by the vertical instability induced by the air-sea temperature difference. The background of increasing trend of SST anomaly is probably a favorable condition for Polar Low formation.

We have also determined the trend from time series of PNA index (Figure 4.19b). It exhibits also a positive trend which indicates a favorable condition for Polar Low formation in the upper level. The atmosphere circulation brings more cold air from the polar region to the open ocean.

The ENSO did not have too much correlation with the Polar Low formation over the North Pacific. It is probably due to the ENSO did not give its influence so far to the sub-polar regions in the North Pacific, especially the Japan Sea, the Bering Sea and the Gulf of Alaska.

A multiple regression analysis of the number of Polar Lows in the 12 sub-regions (Figure 4.5b) with the time-mean circulation indices for PDO, PNA and ENSO reveals which regions are mostly affected by the state of the three circulation systems. The regression results are listed in Figure 4.22 for every sub-region. Obviously, the indices are not independent, so that there is no strict separation of the effect of the circulation systems. As an example, the result of the regression is shown for two sub-regions in Figure 4.23 – one is R1 in the North close to the date line, with a very low correlation of only 15%, and the other R4 south of R1 in the central part of the North Pacific, with the largest correlation, namely 55%. Obviously, the circulation indices cannot be associated with year-to-year variability in R1, while the skill of the indices in describing this variability is remarkable in R4.

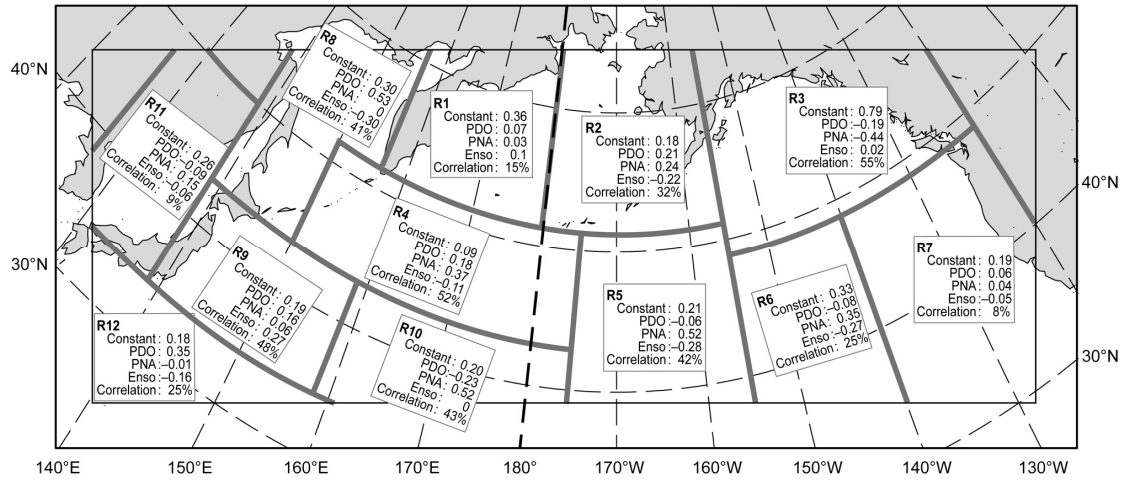
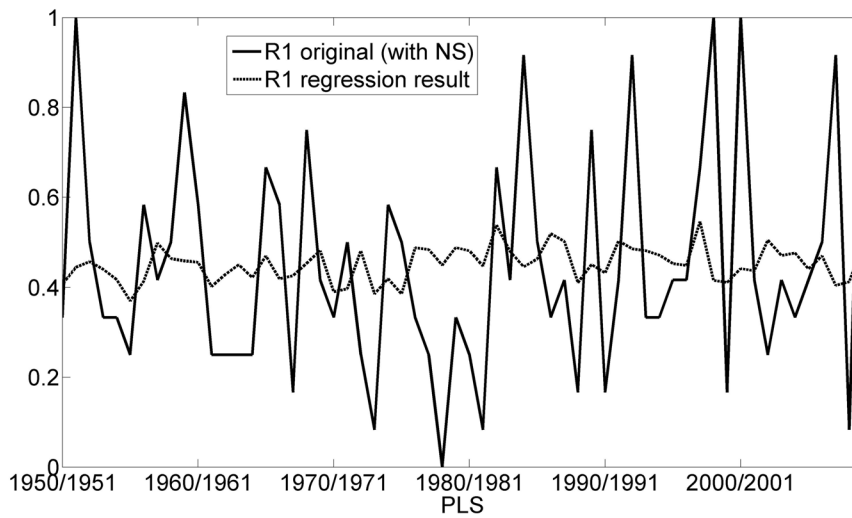


Figure 4.22 Result of multiple regression analysis of number of Polar Low sub-regions R1-12, as given in Figure 3b, and of PLS-time mean circulation indices PDO, PNA and ENSO.



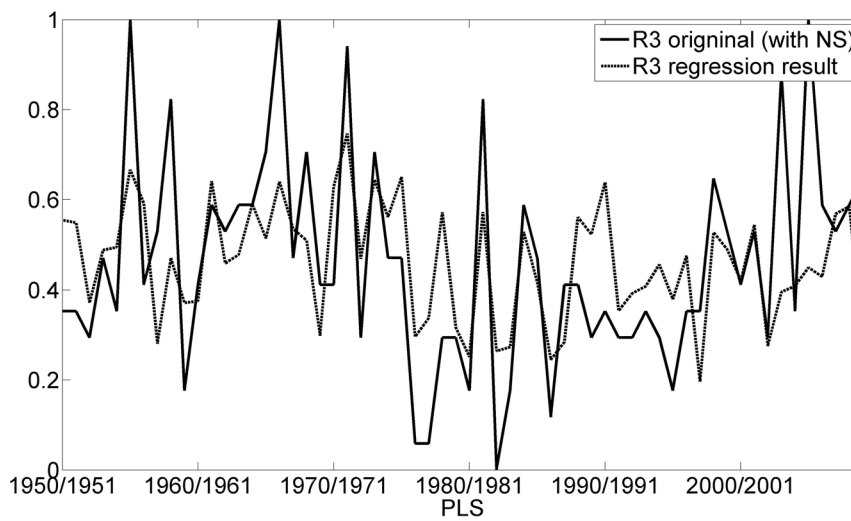


Figure 4.23 The original time series of detected Polar Low numbers (shown in solid lines) and reconstructed time series of Polar Low frequency from multiple regression results of PLS-time mean circulation indices PDO, PNA and ENSO (shown in dashed lines) in two sub-regions, top: R1, and bottom: R3.

We find only two regions, R3 and R4, where the total influence of the indices amounts to a correlation of more than 50%. R3 is in the Northeast, south of Alaska, while R4 at middle latitudes west of the date line; in both cases PNA is associated with the largest coefficient, which is consistent with the pattern of PNA (not shown). A weak link, as expressed by a correlation of 30% or less, is found for R1, R6, R7, R11 and R12, all sub-regions except R1 at the boundaries of the model domain.

To characterize the variability of the CCA patterns and the large scale state indices of PDO, PNA and ENSO we have established regression models. They relate the time series of the PMSL pattern (the CCA has pairs of pattern, one representative for the occurrences of Polar Lows, the other for the PMSL distribution) with the three indices. The success and relative importance of the three indices is summarized in Table 4.3. Additionally the correlation between the time series of PMSL pattern and the one estimated through the regression is listed.

Table 4.3 Result of multiple regression analysis of first two time series of PMSL-patterns from the CCA results, and of PLS-time mean circulation indices PDO, PNA and ENSO.

	Constant	PDO	PNA	ENSO	Correlation
CCA1	0.07	0.19	0.54	-0.01	71%
CCA2	0.48	-0.03	0.36	-0.37	26%

The first CCA pattern is strongly linked to, primarily, PNA but also PDO (which are of course not

independent), but hardly to ENSO; this is different for the second pattern, which is described as being negatively linked to ENSO, equally strongly linked to PNA but hardly to PDO. The overall link is much stronger for the first pattern (as indicated by a correlation of 71%), while the link for the 2nd pattern is weak (correlation of 26%).

Chapter 5

Projection under different scenarios

As shown by the comparison we presented in chapter 3 between NCEP 1 re-analysis data and our regional simulation results, it is hard to investigate the Polar Lows in global coarse grid products. So it is impossible to study the future climatology of Polar Lows under the coarse spatial resolution global climate products.

Therefore we applied the downscaling technology which we introduced in chapter 2 on a set of global simulation results for different emission scenarios from the Intergovernmental Panel on Climate Change (IPCC) developed for the Assessment Reports 3 and 4.

The scenarios we applied here are designed by the IPCC in 2000 (Nakicenovic et al. 2000) known as the Special Report on Emissions Scenarios (SRES). The SRES scenarios consider a wide range of factors, such as population, industrialization, urbanization, social and economic developments to estimate the greenhouse gas emission. Detailed information of the global climate model products for the scenarios is presented in section 2.1. This data set has been applied for various studies of climate phenomenon change under different scenarios in the future, such as: investigating the changes of storm and cyclone activity under different SRES scenarios (Pinto et al. 2007) and increased precipitation intensity (Meehl et al. 2005). Various characteristics which reflected the response of the climate system to different scenarios are also investigated and described by the scientists. Such as: the air temperature, precipitation, sea level raise, sea ice melting, ocean current circulation change, extremely weather phenomenon, aerosols and carbon dioxide cycle variability in climate (Stocker and Schmittner 1997; Boer et al. 2000; Cox et al. 2000; Friedlingstein et al. 2001; Yonetani and Gordon 2001).

Using the global model output, we ran the regional COSMO-CLM result with higher spatial and temporal resolution. By applying the tracking algorithm which we used before for the climatology study of North Pacific Polar Lows from NCEP 1, the climatology of Polar Lows under different scenarios in the next century is derived.

In this chapter, firstly we are going to give a short introduction of the three different scenarios A1B, A2

and B1 for the different story lines and greenhouse gas emissions. Then the downscaling and tracking results for the Polar Lows over the North Pacific under these scenarios are discussed. A brief conclusion for the long time climatology of Polar Low cyclo-genesis related to the global warming is presented at last.

5.1 General information of scenarios and data prepared

There are four different storylines of scenarios given by the IPCC and illustrated in Figure 5.1 by Nakicenovic et al. (2000). All scenarios describe a general development situation of societies on the global level compared to the reality in the coming 100 years. Various kinds of factors which lead to climate change have been considered. Such as: the environmental protection by the governments, the economic growth and high technology development; population increase all over the world; land-use change like forest and farm land; the industrialization; the production of fossil fuel and greenhouse gas pollution.

The primary purpose of investigating different scenario storylines is to explore the uncertainties behind potential trends and greenhouse gas emissions, as well as the influence of driving forces. In short, the different scenario stories can be summarized as (Nakicenovic et al. 2000):

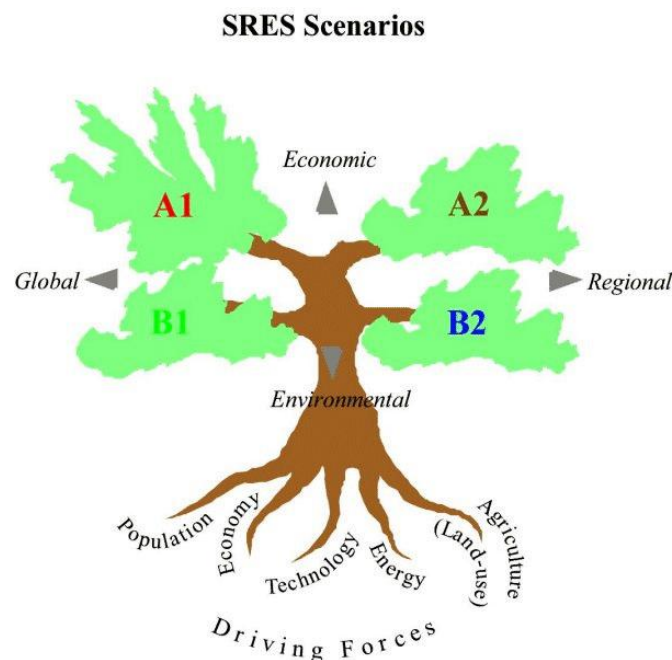


Figure 5.1 Scheme of the storylines for the four scenarios (Nakicenovic et al. 2000).

A1 describes the future society developed with highly developed economy and efficient technologies. The population increases very fast correspondingly to the economy and reaches the top around 2050, then decreases till the end of next century gradually. The number of population should be around 9 billion for the peak. A worldwide communication and interaction is spread through the different regions of the world. Economic, social and cultural issues are widely dealt with in international collaboration. There are several sub-topics for the hypothesis of technological development under A1. We take A1B in our simulation, which represents structure development of society, in which economy, industry and technology are served by fossil fuels. There is no excessive or tiny depended on petroleum and natural gas.

A2 is a scenario also with continued development of economy and population. But the speed of developing is slower compared to the other storylines because of the unbalance development and less communication over the different regions of the world. The nations all over the world are self-reliant. So not only the economy are developed regionally but also the industry, forest, farm and such land-use are isolated and independently.

B1 has a same global population as the storyline of A1, which peaks in mid-century around 2050 and decrease thereafter. Meanwhile the humankind society is developing with reasonable planning and paying more attention to the ecology. Generally, the economic growth is as strong as A1 but focus on service and information industries. There is less greenhouse gas emission because of less industrialization. The clean and high efficient resource technology is highly developed. It is kind of ideal situation of the future for our planet.

B2 is similar to B1 but with more divided behavior for the politics all over the world. We are not going to pay more attention to this scenario.

All the scenario simulations start at 1990 with the similar global background and initial conditions by a 20th century simulation 20C with anthropogenic forcing. As time progresses, the different storylines drive the global situation and variables differ from each other by their characteristic features. Different amount of greenhouse gas emissions are set for different scenarios. Four different greenhouse gases emissions are presented under different scenarios for the next 100 years (Figure 5.2). The anthropogenic emissions of CO₂, CH₄, N₂O and sulfur dioxide under different scenarios are given by the SRES report of IPCC. It is based on various previous studies over the greenhouse gas emission in the past (Akimoto and Narita 1994; Davidson and Kingerlee 1997; Delmas et al. 1997).

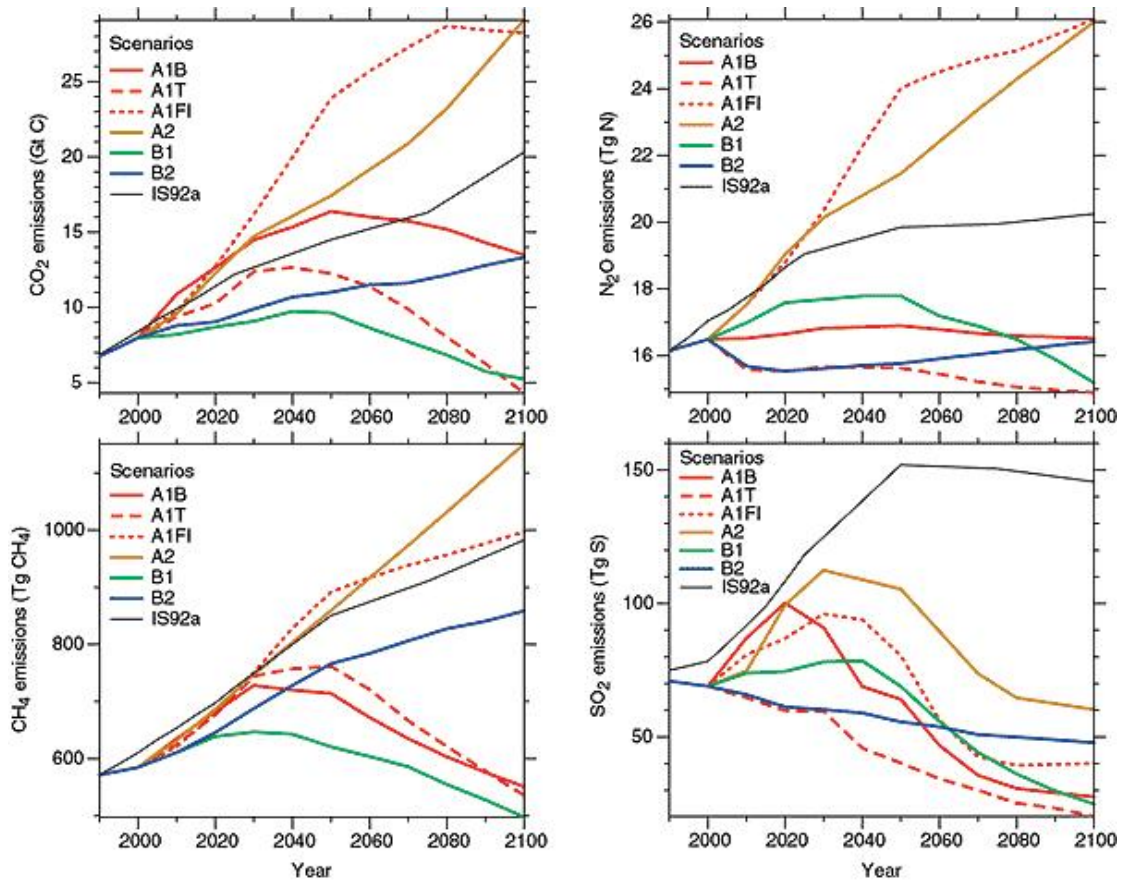


Figure 5.2 Anthropogenic emissions of CO_2 , CH_4 , N_2O and sulphur dioxide for the six illustrative SRES scenarios (Nakicenovic et al. 2000).

We can get the general idea from this figure that the A2 has the strongest increase trend of greenhouse gas emissions in the next 100 years out of the used three scenarios. The scenario of A1B shows an increasing trend in the first half of next century and a decrease in the last 50 years. The general amount of greenhouse gas emission is less than A2. A decreasing emission story is described by the B1 scenario, there is a slow and tiny increase trend for the first 50 year, then a significant reduction. With the same initial condition of 20C at the beginning of the simulation, namely a CO_2 concentration of 367 ppm in year 2000, the concentrations increase to 703 ppm for A1B, to 836 ppm for A2 and 540 ppm for B1 hundred years later (Nakicenovic et al. 2000).

5.2 Simulation and tracking result

In order to describe the effect of the changing CO_2 concentrations to the frequency of forming North Pacific Polar Lows, we take A1B as example. Figure 5.3 presents the time series of detected Polar Lows per PLS and the corresponding trend over the next century under the three realizations of A1B. They

all share a negative trend, for A1B_1 is -0.29 cases/PLS; for A1B_2 is -0.24 cases/PLS and for A1B_3 is -0.25 cases/PLS.

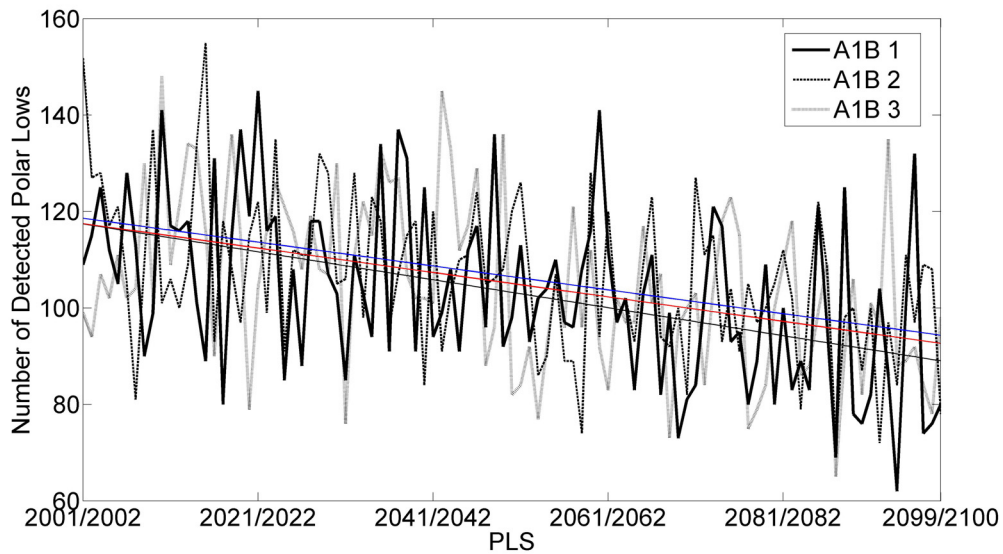


Figure 5.3 Number of Detected Polar Lows per PLS from 2001/2002 to 2099/2100 under the scenario of A1B. 1 – 3 indicate the numbers of realization experiments.

The mean values, standard deviations and overall trends are summarized in Table 5.1. The mean value of detected Polar Lows in a PLS is 103.24 for A1B_1, 106.47 for A1B_2 and 105.07 for A1B_3.

Table 5.1 Mean value, standard deviation and overall trend of detected number of Polar Lows under the three realizations of A1B.

	Mean value	Std. Dev.	Trend (case/PLS)
A1B_1	103.24	18.19	-0.29
A1B_2	106.47	16.12	-0.24
A1B_3	105.07	17.49	-0.25

There is no major difference between the three realizations of A1B, they all share very similar numbers of the mean value of detected Polar Lows, the corresponding standard deviation and of the trends. Therefore we take A1B_1 for further discussion. All the other scenarios presented below indicate the first realization results, namely A2_1, B1_1 and 20C_1.

The density of Polar Low cyclo-genesis and the characteristic over the 12 sub-regions in the next century are presented in Figure 5.4. The region of highest Polar Low density is located to the east

ocean of Japan Island (R9). The highest weighted mean value of Polar Lows cyclo-genesis for each grid point is found in this sub-region with 2.23 cases per grid point and hundred years. In the last 6 decades R9 showed the second highest value of North Pacific (Figure 4.5). The sub-regions R1, R8 and R11 take the second class of the maximum value, which means the Polar Low activity there is relatively higher than the other sub-regions (e.g. R2, R3 and R4). By checking the density distribution for every PLS, we found that there is always relatively high density and weighted mean value located in these sub-regions compared to others, even for the first 10 PLSs of this century (2001/2002 – 2010/2011) (not shown). This is different to the last 62 PLSs (Figure 4.5). R1, R3, R4 and R9 are the highest frequency sub-regions of Polar Low distribution, lower frequency exhibits in R8 and R11. This situation is mainly due to the different status of forcing data NCEP 1 and ECHAM5.

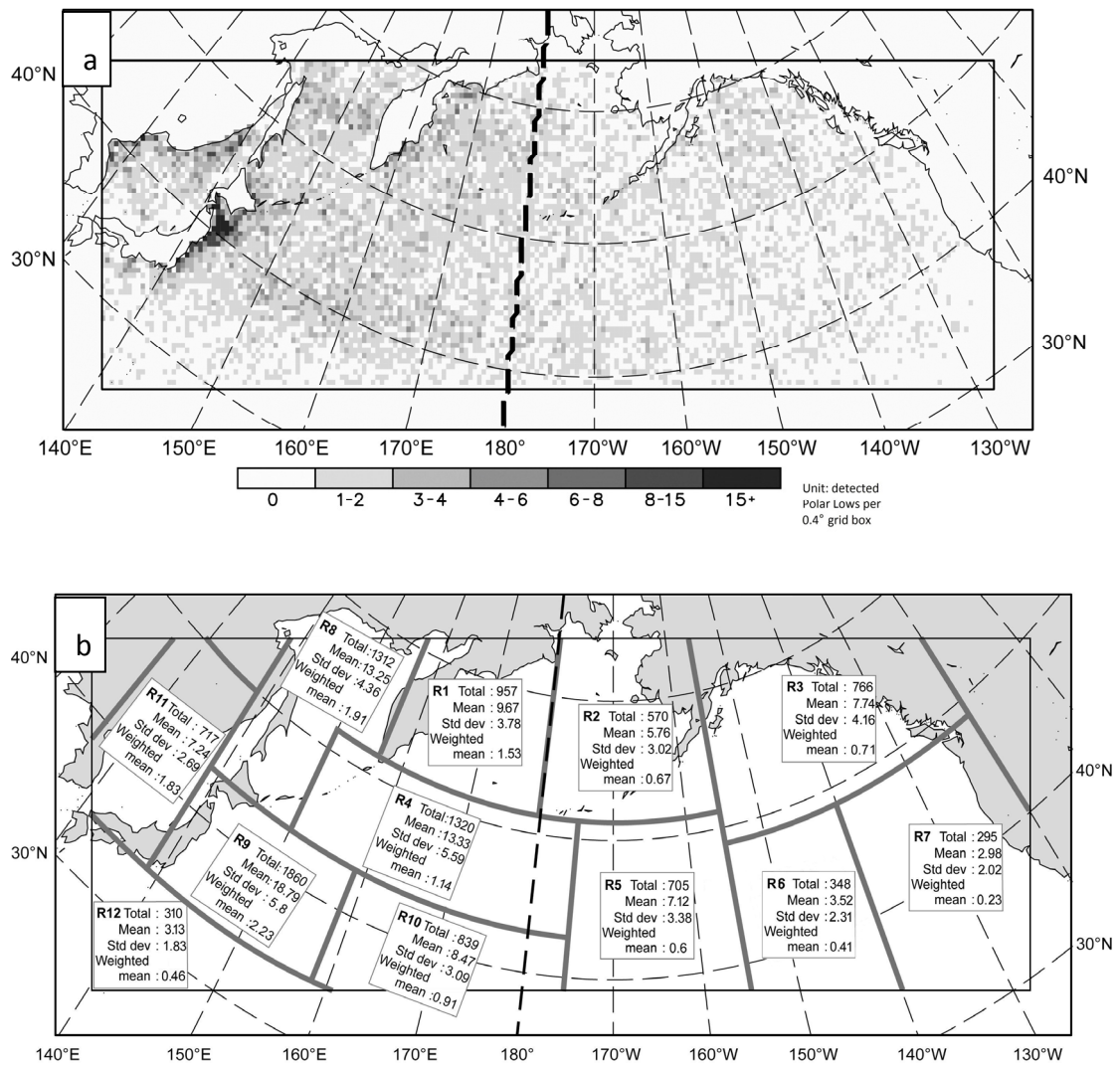


Figure 5.4 a) Polar Low frequency distribution under A1B_1. Unit: detected Polar Lows per 0.4° grid box. b) Sub-regions, for which the numbers of detected Polar Lows were aggregated (R1-R12) and respective number of detected Polar Lows (see text). Also given for each region are mean number of Polar Lows per PLS (Mean), standard deviation (Std dev) and Polar Lows per area unit (Weighted mean). The latter number is divided by the

sea grid points of corresponding sub-region.

We are interested in this phenomenon of Polar Low distribution over North Pacific under the A1B_1 scenario. The variability of Polar Low density in the different sub-regions over the 100 years is also an interesting topic. By checking the proportion of detected Polar Low numbers over the highest frequency sub-regions (R1, R4, R8, R9 and R11) for the first and last 20 PLSs, we found that there is an increased proportion of detected Polar Low numbers in R1 and R8 at the end of 21th century (Table 5.2). For the first 20 PLSs, R1 takes 9.2% of the total Polar Lows and increases to 10.1% for the last 20 PLSs. Meanwhile, R8 increases from 11.5% to 14.3% through the century. The proportion is decreasing for R4 (13.7% to 12.4%) and R9 (19.0% to 18.3%). R11 is nearly stable. Generally, the sub-regions in the north (R1 and R8) have an increase proportion of Polar Lows through the century compared to the sub-regions in the south. The distribution of Polar Lows is moving northward in the 21th century under the A1B scenario.

For comparison the strength of the trends between the sub-regions, we took area weighted mean of their trends. The trends are divided by the corresponding sea grid points for each sub-region. The overall trend of detected Polar Lows is negative with -0.29 cases/PLS, namely -2.7×10^{-5} cases per PLS per grid point. But the trend in different sub-regions is not uniform. R8 takes the weakest decreasing trend compared to others. R1, R4 and R11 take the second weak class of decrease trend. R8 takes the weakest decreasing trend of -0.9×10^{-5} cases per PLS per grid point while R9 takes the strongest decrease trend of -8.3×10^{-5} cases per PLS per grid point. This is an evidence for the northward shift of Polar Low distribution through the next 100 years.

Table 5.2 Detected number of Polar Lows, corresponding proportion in the sub-regions of highest Polar Low density, overall and weighted mean trend during 2001/2002-2099/2100 (R1, R4, R8, R9 and R11) for the first and last 20 PLSs under A1B_1. PL represents the detected number, % represents the proportion. The weighted mean trend value is the trend for the sub-region divided by the corresponding number of sea grid points.

	Total region	R1		R4		R8		R9		R11	
		PL	%	PL	%	PL	%	PL	%	PL	%
2001/2002 – 2020/2021	2211	203	9.2	302	13.7	254	11.5	421	19.0	155	7.0
2080/2081 – 2099/2100	1753	176	10.1	218	12.4	251	14.3	321	18.3	121	6.9
Overall Trend (case/PLS)	-0.29	-0.020		-0.048		-0.006		-0.069		-0.019	
Area weighted mean of trend (10^{-5})	-2.7	-3.2		-4.1		-0.9		-8.3		-4.8	

In order to investigate why there is a northward shift for the Polar Low cyclo-genesis, we checked the proportion of ice time during every PLS (October to next April) over the North Pacific for the last 50 years of 20C_1 and A1B_1. In order to show the 150 years conditions in brief, the mean proportion for the PLSs during 1950s and 1990s of 20C_1, 2000s, 2030s, 2060s and 2090s of A1B_1 are presented

(Figure 5.5).

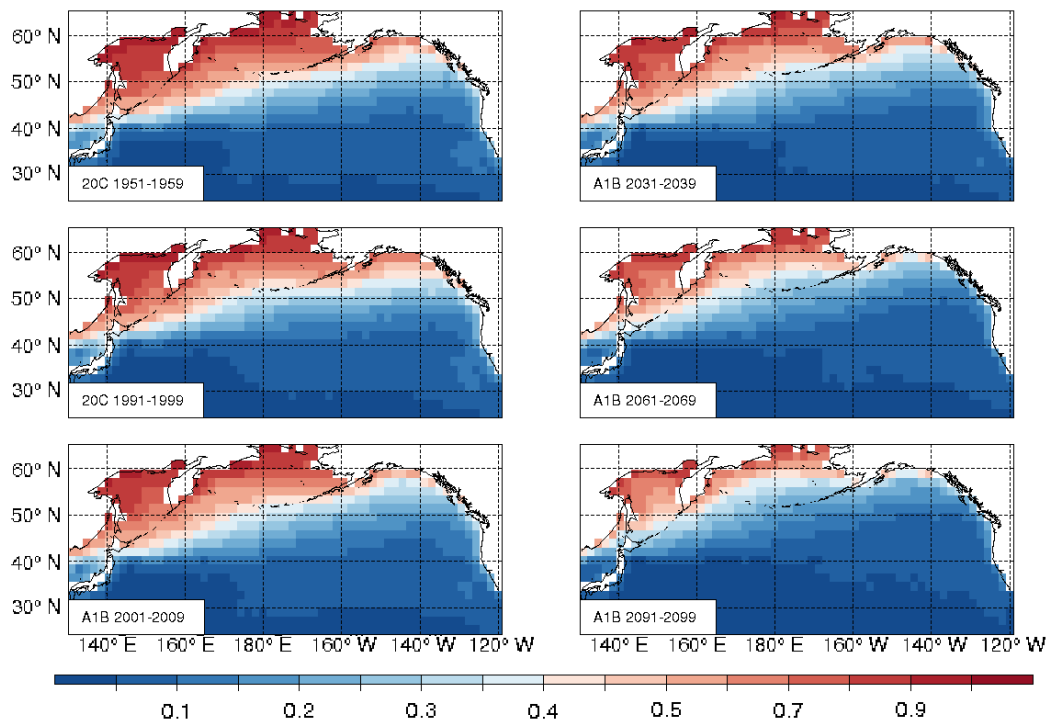


Figure 5.5 Mean proportion of ice covered time over the North Pacific Ocean during the PLS for different time periods, 1951-1959 and 1991-1999 are calculated from the ECHAM5/MPI-OM1 of 20C_1; 2001-2009, 2031-2039, 2061-2069 and 2091-2099 are calculated from the ECHAM5/MPI-OM1 of A1B_1. To be brief, the number of year represents the first half year of the PLS, for example: 1951 represents the PLS 1951/1952.

For the first 60 PLSs during 1950 – 2009, the ice edge did not change much. The ice dominates over 70% of the PLS time over most part of the sea of Okhotsk and Bering Sea. The Gulf of Alaska also takes nearly 50% of the time frozen along the north coast. But for the last 70 PLSs during 2031 – 2099, the proportion of ice time during winter is significantly decreasing. The frozen time over these three regions is dropped by 55% around to the end of next century. It indicates that the ice edge is melting under the scenario of more greenhouse gas emission and global warming. As the barrier is melting, the cold flow from the polar region faces the relatively warm SST more directly than before. More Polar Lows would be formed over the ocean to the north where the ice edge melts. These regions (sea of Okhotsk and Bering Sea) are represented as R1 and R8 in the sub-region map, while there should be less Polar Lows in the south region (R4 and R9). There is no obvious change for the sea ice cover over the Japan Sea through the 150 years (represented as R11); consistently the proportion of R11 is stable.

Furthermore, we are interested in how the greenhouse gas emission and the global warming affected the frequency of Polar Lows over the North Pacific in the next hundred years. A potential relationship between the increasing air temperature and the dynamical process of Polar Low cyclo-genesis are

discussed below.

As Zahn and von Storch (2010) pointed for the Polar Low frequency over the North Atlantic in the next century, even the SST of the Atlantic is getting warmer, the air temperature over the troposphere is increasing relatively higher compared to the SST. The relatively slower warming ocean makes the air-sea temperature difference lower, which means that the vertical stability is getting higher. The increased stability is less favourable for Polar Low cyclo-genesis. Here we calculated the temperature difference between SST and air temperature on 500 hPa level for both 20C and A1B when there is no ice over the ocean, then count the number of grid points fulfilling the third Polar Low criterion (air-sea temperature ≥ 39 K) for every PLS (Figure 5.6). We get a confirmation for the decreasing trend in Polar Low activity for the next 90 years compared to the positive trend for the last 60 years.

There is a tiny positive trend during 1948/1949 – 2009/2010 (13.10/PLS, represents as blue dashed line). It is very close to the trend during 1948/1949 – 1999/2000 (13.02/PLS), so only the trend of 1948/1949 – 2009/2010 is presented. The number of grid points fulfilling the third criterion in PLS 2001/2002 is almost same to the number of 1999/2000 in 20C, with nearly 36000 points per PLS. But since 2000 the A1B has an obvious decreasing trend for this favourable condition. The mean value of grid points for this favourable condition is 31426 per PLS, and the trend is -91.19/PLS. In general, the grid points decreased 9028 in 100 years. Compared to the mean value, this favourable condition for Polar Low cyclo-genesis decreased nearly one third since the beginning of this century. The frequency of Polar Low cyclo-genesis has decreased consistently.

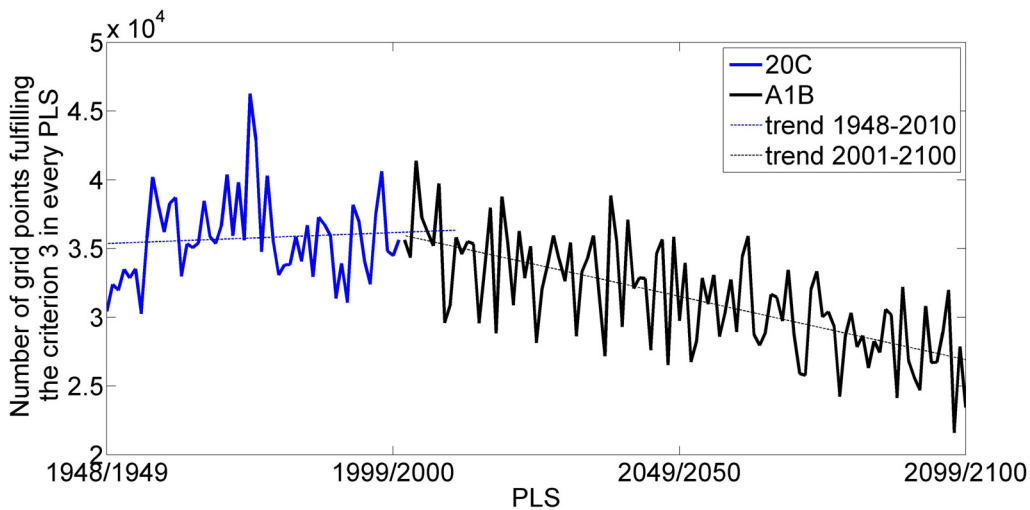


Figure 5.6 Time series of grid point number fulfilling the third Polar Low criterion during 1948/1949 – 1999/2000 from 20C, 2001/2002 – 2009/2100 from A1B, dashed lines with corresponding color represent the trend. Blue dashed line represents the trend during 1948/1949 – 2009/2010, black dashed line represents the trend during 2001/2002 – 2099/2100.

As shown in Figure 5.3 and Table 5.1, there is no obvious difference between the different realizations of one story line. Therefore and for reasons of computational cost and time we only take the first realization for the different scenarios such as A2_1 and B1_1. Figure 5.7 presents the different tracking results for the next 100 years under the three scenarios. The mean value, standard deviation and overall trend are presented in Table 5.3.

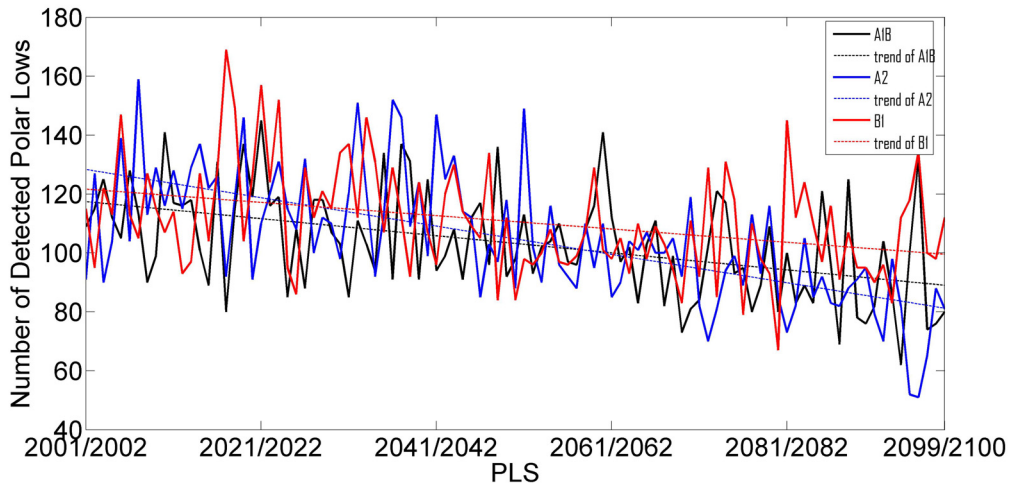


Figure 5.7 Number of Detected Polar Lows from 2001/2002 to 2099/2100. Black line represents the scenario of A1B_1, Blue line represents the scenario of A2_1 and red line represents the scenario of B1_1, dashed lines with corresponding color represent the overall trends.

Table 5.3 Mean value, standard deviation and overall trend of detected number of Polar Lows under the three different scenarios A1B_1, A2_1 and B1_1.

	Mean value	Std. Dev.	Trend (case/PLS)
A1B_1	103.24	18.19	-0.29
A2_1	104.82	21.64	-0.49
B1_1	110.63	18.45	-0.2

We have found that with a higher greenhouse gas emission, the frequency of Polar Low occurrence has a correspondingly stronger decreasing trend. The trend of A1B_1 is negative with -0.29 case/PLS. For the scenario of A2_1, which has a much higher greenhouse gas emission, the trend is as more negative with -0.49 cases/PLS. The corresponding standard deviation is also higher which indicates a higher year-to-year variability. For B1_1 the trend is much less, it is negative with -0.2 case/PLS.

We have inferred that there will be a lower trend of Polar Low occurrence frequency over the North Pacific in the next century under a global warming situation with a higher greenhouse gas emission.

The higher air temperature raise, the lower air-sea temperature differences drop. This is similar with what Zahn and von Storch (2010) get for the Polar Low frequency over the North Atlantic under different scenarios.

5.3 Conclusion

We applied global climate model products under different scenarios of societal development in the future, which go along with different greenhouse gas emissions and global warming developments. Corresponding spatial distribution of cyclo-genesis and the trend of Polar Low occurrence frequency are calculated by the technology we applied for the hindcast of the last 62 years simulation results.

A general idea is that the frequency of Polar Low occurrence has a close relationship with the global warming and corresponding greenhouse gas emission. With a stronger increase of the CO₂ emission the frequency is decreasing much more rapidly than with smaller increases. The spatial distribution shows a northward shift through next century under the scenario of A1B_1. The explanation is mainly related to the raised atmosphere temperature and the melting sea ice cover around the polar region which caused by the global warming. The decrease of air-sea temperature difference leads to weaker vertical instability. With weaken favourable condition, the frequency of Polar Low occurrence is decreasing; with melting sea ice and northward ice edge, the Polar Lows forms more northward compared to the past.

We have to point out that our regional simulation is only a scenario just related to greenhouse gas emissions and not a prediction of what will happen in the coming 90 years.

Chapter 6

Conclusion and outlook

Here we are going to discuss the main results from the previous chapters. The hypothesis, technique and conclusion will be discussed step by step. Finally the outlook pointed out how to improve our work and further development.

Generally, we are looking for a technical way to construct statistics of Polar Low formation over the North Pacific during the last 6 decades. The variability of Polar Low frequency under different scenarios in the future is also an interesting scientific issue. Here we employed the dynamical downscaling technology in a regional climate model called COSMO-CLM to make use of the NCEP 1 re-analysis of GCM output data. A tracking algorithm which detects and records the Polar Lows over the North Atlantic has been applied to the simulation result. Data about the start position, time, PMSL and wind speed has been recorded.

The climatology characteristic of Polar Low formation during the last 62 PLSs were investigated based on the tracking result. The variability of multi-decadal trend has been analyzed against the background of large-scale climate change, such as PDO and PNA. A predication to the next hundred years has also been deduced from the simulation result forced by the IPCC different scenarios.

The tendency of Polar Lows under assumed greenhouse gas emission in the 21st century has been estimated.

In the first step of our work, we set up the model and run several cases to verify the effect of the dynamical downscaling technique and the regional climate model. We produced higher quality data both in spatial and temporal compared to the NCEP 1 forcing data. More meso-scale features have been produced which could not be observed from the original re-analysis data. As a preparational analysis for the feasibility of simulating of Polar Lows in the North Pacific, we have examined the performance of a dynamical downscaling system, which makes use of the NCEP 1 re-analysis data as forcing of the COSMO-CLM limited area model. The objective is to generate sub-synoptic scale descriptions of Polar Lows, without making use of high-resolution initial fields. In three case studies of Polar Low formation and life cycle, we found that due to the higher spatial resolution considerably more detail in the simulation compared to the re-analysis description. Also the hourly output turns out to be helpful compared to the routine 6 hourly output from NCEP 1 re-analysis.

In one case the spiral structure of Polar Lows has been observed both on the presented mean sea

level pressure and wind field. By comparing the simulation result with literature, we have found most of the cases can be reconstructed.

Then we applied a tracking algorithm to the cases we have produced. The tracking algorithm had already been tested and applied on multi-decadal climatology analysis of Polar Lows over the North Atlantic. For 10 cases we checked, half of them have been detected by the default setting of the tracking algorithm without modification. The tracking results were very similar to the satellite observations and the literatures. Other half cases are reproduced with a relatively weak signature on PMSL, air temperature or wind speed. They are too weak to be reliably detected or recorded by the default tracking method. Therefore we changed some of the threshold values of the criterion. Finally the 40% cases have been detected and recorded by the modified tracking algorithm. There left 10% of the cases could not be tracked by the algorithm. As the aim of our work is focused on the issue of change in time, this statistical error is acceptable.

From the two steps above, we concluded that the model set-up and the tracking algorithm are suitable for the investigation of changing Polar Lows statistics in the North Pacific. Then we launched a continuous simulation with COSMO-CLM, forced by six decades of NCEP 1 re-analyses. For the first time a multi-decadal RCM downscaling result has been presented with the purpose of deriving the climatology study of Polar Lows in the sub-polar North Pacific.

The 1948-2010 climatology shows large inter-annual variability and positive long-term trend of Polar Low cyclo-genesis in the North Pacific. The distribution of Polar Low formation over the North Pacific shows there are three sub-regions with the highest density of cyclo-genesis: the east of Japan Island, the southwest of Bering Sea and the Gulf of Alaska. This is consistent to the previous results from satellite observation. Most of the Polar Lows over the North Pacific have a life cycle of less than two days and the highest frequency for Polar Low outbreak in December, January and February. By examining the corresponding trend of Polar Low numbers in different sub-regions over the 62 PLSs, we have found that the sub-region east of Japan Island (R9 in Figure 4.5b) dominates the trend over the whole North Pacific. It has a positive trend, while the Gulf of Alaska shows a slightly negative trend.

The results of CCA shown there is a close relationship between the time-mean PMSL patterns and the Polar Low density. Anomalous flows from cold surfaces were found to support the large-scale synoptic environment of Polar Low formation. The associated correlation patterns indicate the correlation structure between the Polar Low occurrence and the geo-potential height and the air temperature on different pressure level. Generally, the Polar Low formation has a close relationship with the atmosphere circulation on all levels.

Then we related the Polar Low formation against the background of large-scale climate change. The PDO and PNA tele-connection relate part of the variability of Polar Low formation, including the trend during the last 6 decades mainly to a large scale shift both on spatial and temporal of SST and atmospheric circulation over the North Pacific.

The simulation results under different scenarios from IPCC indicate that the frequency of Polar Low occurrence has a close relationship with greenhouse gas emission and global warming. Melting ice edge and decrease air-sea temperature difference is the main reason for the northward shift of Polar Low formation and decreasing cyclo-genesis frequency.

Here we also have to point out that our work is not perfect. The spatial resolution is not high enough and the tracking algorithm can be improved by detecting the position of Polar Lows on 500 hPa pressure level. The simulation for different scenarios from IPCC only related to 4 realizations (A1B_1, A1B_2, A1B_3, A2_1 and B1_1). More realizations should be introduced to further analyze and discussion such as 20C and B2.

Acknowledgments

First I would like to appreciate the China Scholarship Council (CSC) and the Helmholtz-Gemeinschaft Zentrum. The Junior Scientist Exchange Program organized by the CSC and Helmholtz-Gemeinschaft supported the three years scholarship fund to pursue my study in Germany as a PhD student.

Then I would like to thank Prof. Dr. H. von Storch for the appraisal of the work. He offered me the opportunity to work at Helmholtz-Zentrum Geesthacht and University of Hamburg. He trained me patiently and gave me lots of opportunity to present my work on international academic exchanges conference. I further have to thank Dr. Beate Geyer and Dr. Matthias Zahn for the readiness of my work as the second supervisor. They give me great help both for my modeling problems and Polar Low knowledge. Dr. Beate Geyer guided me during the three years not only with the scientific research but also for the manuscript and writing. Thanks a lot to Dr. Burkhardt Rockel, he guided me for the model programing and script problems. He also helped me to prepare the ECHAM5 scenario result.

Special thanks are given to Ms. Beate Gardeike. She helped me a lot with my figure issues.

I am also great appreciated to the Deutsches Klimarechenzentrum (DKRZ), especially for the blizzard super computer group. They helped me a lot with the region climate model simulation and data storage. Dr. Jens Meywerk helped me with the local solaris computer and matlab problems.

Thanks a lot to the Chinese colleagues at the Helmholtz-Zentrum Geesthacht. We have spent 3 years together in Geesthacht's foreign life here.

At last many thanks to my family for the moral support.

谨以此文献给我的父母和亲人.

Reference

Akimoto H, Narita H (1994) Distribution of SO₂, NO_x, and CO₂ emissions from fuel combustion and industrial activities in Asia with 1°x1° resolution. *Atmospheric Environment* 28(2): 213–225

Akkermans T, Lauwaet D, Demuzere M, et al. (2012) Validation and comparison of two soil-vegetation-atmosphere transfer models for Tropical Africa. *Journal of Geophysical Research* 117: G02013

Bjerknes J (1964) Atlantic air-sea interaction. *Advances In Geophysics* 10: 1–82

Blier W (1996) A numerical modeling investigation of a case of polar airstream cyclogenesis over the Gulf of Alaska. *Mon. Wea. Rev.* 124: 2703–2725

Boer GJ, Flato G, Ramsden D (2000) A transient climate change simulation with greenhouse gas and aerosol forcing: projected climate to the twenty-first century. *Climate Dynamics* 16: 427–450

Bond NA, Shapiro MA (1991) Polar Lows Over the Gulf of Alaska In Conditions of Reverse Shear. *Monthly Weather Review* 119: 551–572

Bresch JF, Reed RJ, Albright MD (1997) A Polar-Low Development over the Bering Sea: Analysis, Numerical Simulation, and Sensitivity Experiments. *Monthly Weather Review* 125: 3109–3130. doi:10.1175/1520-0493(1997)125<3109:APLDOT>2.0.CO;2

Businger S (1985) The Synoptic Climatology of Polar Low Outbreaks. *Tellus Series A-dynamic Meteorology and Oceanography* 37: 419–432

Businger S (1987) The synoptic climatology of polar-low outbreaks over the Gulf of Alaska and the Bering Sea. *Tellus* 39A: 307–325

Businger S, Walter B (1988) Comma Cloud Development and Associated Rapid Cyclogenesis Over the Gulf of Alaska - A Case-study Using Aircraft and Operational Data. *Monthly Weather Review* 116: 1103–1123

Carleton AM (1985) Satellite Climatological Aspects of the Polar Low and Instant Occlusion. *Tellus Series A-dynamic Meteorology and Oceanography* 37: 433–450

Cavicchia L, von Storch H (2011) The simulation of medicanes in a high-resolution regional climate model. *Clim Dyn.* Available at: Cavicchia2011.pdf. doi:10.1007/s00382-011-1220-0

Champeaux JL, Masson V, Chauvin R (2005) ECOCLIMAP: a global database of land surface parameters

at 1 km resolution. *Meteorological Applications* 12: 29–32

Chen F, Geyer B, Zahn M, von Storch H (2012) Toward a Multi-Decadal Climatology of North Pacific Polar Lows Employing Dynamical Downscaling. *Terr. Atmos. Ocean. Sci.* 23: 291–301. doi:10.3319/TAO.2011.11.02.01(A)

Condron A, Bigg GR, Renfrew IA (2006) Polar Mesoscale Cyclones in the Northeast Atlantic: Comparing Climatologies from ERA-40 and Satellite Imagery. *Mon. Wea. Rev.* 134: 1518–1533

Cox PM, Betts RA, Jones CD, Spall SA, Totterdell IJ (2000) Acceleration of global warming due to carbon-cycle feedbacks in a 3D coupled climate model. *Nature* 408: 184–187

Davidson EA, Kinglerlee W (1997) A global inventory of nitric oxide emissions from soils. *Nutrient Cycling in Agroecosystems* 48(1/2): 37–50

Delmas R, Serea D, Jambert C (1997) Global inventory of NO_x sources. *Nutrient Cycling in Agroecosystems* 48(1/2): 51–60

Denis B, Jean C, René L (2002) Spectral Decomposition of Two-Dimensional Atmospheric Fields on Limited-Area Domains Using the Discrete Cosine Transform (DCT). *Mon. Wea. Rev.* 130: 1812–1829. doi:10.1175/1520-0493(2002)130<1812:SDOTDA>2.0.CO;2

Dobler A, Ahrens B (2008) Precipitation by a regional climate model and bias correction in Europe and South Asia. *Meteorol. Z.* 17: 499–510

Dobler A, Ahrens B (2011) Four climate change scenarios for the Indian summer monsoon by the regional climate model COSMO-CLM. *Journal of Geophysical Research* 116: D24104, 13pp. doi:10.1029/2011JD016329

Douglas MW, Fedor LS, Shapiro MA (1991) Polar Low Structure Over the Northern Gulf of Alaska Based On Research Aircraft Observations. *Monthly Weather Review* 119: 32–54

Feser F (2006) Enhanced detectability of added value in limited-area model results separated into different spatial scales. *Monthly Weather Review* 134: 2180–2190

Feser F, von Storch H (2005) A spatial two-dimensional discrete filter for limited-area-model evaluation purposes. *Monthly Weather Review* 133: 1774–1786

Feser F, von Storch H (2008) A dynamical downscaling case study for typhoons in SE Asia using a regional climate model. *Monthly Weather Review* 136: 1806–1815

Forbes GS, Lottes WD (1985) Classification of Mesoscale Vortices In Polar Airstreams and the Influence

of the Large-scale Environment On Their Evolutions. *Tellus Series A-dynamic Meteorology and Oceanography* 37: 132–155

Friedlingstein P, Bopp L, Ciais P, et al. (2001) Positive feedback between future climate change and the carbon cycle. *Geophys. Res. Lett* 28: 1543. doi:10.1029/2000GL012015

Fu G, Liu Q, Wu Z (1999) General features of polar lows over the Japan Sea and the Northwestern Pacific. *Chinese Journal of Oceanology and Limnology* 17: 300–307

Fu G, Niino H, Kimura R, Kato T (2004a) A Polar Low over the Japan Sea on 21 January 1997. Part I: Observational Analysis. *Monthly Weather Review* 132: 1537–1551. doi:10.1175/1520-0493(2004)132<1537:APLOTJ>2.0.CO;2

Fu G, Niino H, Kimura R, Kato T (2004b) Multiple polar meso-cyclones over the Japan Sea on 11 February 1997. *Mon. Wea. Rev.* 132: 793–814

Gray SL, Craig GC (1998) A simple theoretical model for the intensification of tropical cyclones and polar lows. *Quart. J. Roy. Meteor. Soc.* 124: 919–947

Guan B, Nigam S (2009) Analysis of Atlantic SST Variability Factoring Interbasin Links and the Secular Trend: Clarified Structure of the Atlantic Multidecadal Oscillation. *Journal of Climate* 22: 4228–4240

Guo J, Fu G, Li Z, Shao L, Duan Y, Wang J (2007) Analyses and numerical modeling of a polar low over the Japan Sea on 19 December 2003. *Atmos. Res.* 85: 395–412

Hare SR, Francis RC (1995) Climate change and salmon production in the Northeast Pacific Ocean. *Can. Spec. Publ. Fish. Aquat. Sci.* 121: 357–372

Harly DG (1960) Frontal contour analysis of a “polar low”. *Meteor. Mag.* 89: 146–147

Heinemann G, Claud C (1997) Report of a workshop on “theoretical and observational studies of polar lows” of the European geophysical society polar lows working group. *Bull. Amer. Meteor. Soc.* 78: 2643–2658

Hotelling H (1936) Relations between two sets of variants. *Biometrika* 28: 321–377

Jungclaus JH, Botzet M, Haak H, et al. (2005) Ocean circulation and tropical variability in the coupled model. ECHAM5/MPI-OM. *J. Climate* 19: 3952–3972

Kalnay E, Kanamitsu M, Kistler R, et al. (1996) The NCEP/NCAR 40-year reanalysis project. *Bulletin of the American Meteorological Society* 77: 437–471

- Kolstad EW (2006) A new climatology of favourable conditions for reverse-shear polar lows. *Tellus Series A-dynamic Meteorology and Oceanography* 58: 344–354
- Kolstad EW (2011) A global climatology of favourable conditions for polar lows. *Q. J. R. Meteorol. Soc.* 137: 1749–1761. doi:10.1002/qj.888
- Kolstad EW, Bracegirdle TJ, Seierstad IA (2009) Marine cold-air outbreaks in the North Atlantic: temporal distribution and associations with large-scale atmospheric circulation. *Climate Dynamics* 33: 187–197. doi:10.1007/s00382-008-0431-5
- Kulkarni A, von Storch H (1995) Monte Carlo experiments on the effect of serial correlation on the Mann-Kendall test of trend. *Meteor. Z.* 4: 82–85
- Lorenz EN (1956) Empirical orthogonal functions and statistical weather predictions. *Statistical Forecast Project Report 1*.
- Luksch U, von Storch H (1992) Modeling the Low-Frequency Sea Surface Temperature Variability in the North Pacific. *J. Climate* 5: 893–906
- Luksch U, von Storch H, Maier-Reimer Ernst (1990) Modeling North Pacific SST anomalies as a response to anomalous atmospheric forcing. *Journal of Marine Systems* 1: 155–168
- Lystad M (1986) Polar lows in the Norwegian, Greenland and Barents Sea. Final Rep. Polar Lows Project, The Norwegian Meteorological Institute 196
- Mailhot J, Hanley D, Bilodeau B, Hertzman O (1996) A numerical case study of a polar low in the Labrador Sea. *Tellus* 48A: 383–402
- Mansfield DA (1974) Polar lows: the development of baroclinic disturbance in cold air outbreaks. *Quart. J. Roy. Meteor. Soc.* 100: 541–554
- Mantua N (2000) Comparison of typical warm PDO/El Niño SST, SLP, and wind anomalies. . Available at: <http://jisao.washington.edu/pdo/graphics.html>
- Mantua NJ, Hare SR, Zhang Y, Wallace JM, Francis RC (1997) A Pacific interdecadal climate oscillation with impacts on salmon production. *Bull. Amer. Meteor. Soc.* 78: 1069–1079
- Marsland SJ, Haak H, Jungclaus JH, Latif M, Röske F (2003) The Max-Planck-Institute global ocean/sea ice model with orthogonal curvilinear coordinates. *Ocean Model* 5: 91–127
- Meehl GA, Arblaster JM, Tebaldi C (2005) Understanding future patterns of increased precipitation intensity in climate model simulations. *Geophys. Res. Lett.* 32: L18719. doi:10.1029/2005GL023680

Moore ID, Grayson RB, Ladson AR (1991) Digital Terrain Modelling: A Review of Hydrological, Geomorphological and Biological Applications. *Hydrological Processes* 5: 3–30. doi:10.1002/hyp.3360050103

Nagata S (1993) Meso- β -scale vortices developing along the Japan-Sea polar-airmass convergence zone (JPCZ) cloud band : Numerical simulation. *J. Meteor. Soc.* 71: 43–57

Nakicenovic N, Alcamo J, Davis G, et al. (2000) Special report on emissions scenarios: a special report of Working Group III of the Intergovernmental Panel on Climate Change. . Available at: <http://www.ipcc.ch/ipccreports/sres/emission/index.php?idp=0>

Noer, Ovsted GM (2003) Forecasting of polar lows in the Norwegian and the Barents Sea. Proc. of the 9th meeting of the EGS Polar Lows Working Group, Cambridge, UK

Nordeng TE (1986) A model-based diagnostic study of the development and maintenance mechanism of two polar lows. *Tellus* 42A: 92–108

Pavlik D, Söhl D, Pluntke T, Mykhnovych A, Bernhofer C (2012) Dynamic downscaling of global climate projections for Eastern Europe with a horizontal resolution of 7 km. *Environ Earth Sci.* 65: 1475–1482. doi:10.1007/s12665-011-1081-1

Pearson K (1902) On lines and planes of closest fit to systems of points in space. *Phil. Mag.* 2: 559–572

Pinto JG, Ulbrich U, Leckebusch GC, Spanghel T, Reyers M, Zacharias S (2007) Changes in storm track and cyclone activity in three SRES ensemble experiments with the ECHAM5/MPI-OM1 GCM. *Clim. Dynam.* 29: 195–210. doi:10.1007/s00382-007-0230-4

Rasmussen E (1981) An Investigation of A Polar Low With A Spiral Cloud Structure. *Journal of the Atmospheric Sciences* 38: 1785–1792

Rasmussen EA, Claud C, Purdom JF (1996) Labrador Sea polar lows. *Global Atmos. Ocean Syst.* 4: 275–334

Rasmussen EA, Turner J (2003) Polar lows: mesoscale weather systems in the polar regions. Cambridge University Press

Rasmusson EG, Carpenter TH (1982) Variations in tropical sea surface temperature and surface wind fields associated with the Southern Oscillation/El Niño. *Mon. Wea. Rev.* 110: 354–384

Reed RJ (1979) Cyclogenesis in polar airstreams. *Mon. Wea. Rev.* 107: 38–52

Rockel B, Castro CL, Sr. RAP, von Storch H, Leoncini G (2008) Dynamical downscaling: Assessment of

model system dependent retained and added variability for two different regional climate models. *Journal of Geophys. Res.* 113

Rockel B, Geyer B (2008) The performance of the regional climate model CLM in different climate regions, based on the example of precipitation. *Meteorol. Z.* 17: 487–498. doi:10.1127/0941-2948/2008/0297

Roeckner E, G. Bauml, Bonaventura L, et al. (2003) The atmospheric general circulation model ECHAM5. PART I: model description. Max-Planck-Institut für Meteorologie, Hamburg

Roeckner E, Lautenschlager M, Schneider H (2006a) IPCC-AR4 MPI-ECHAM5_T63L31 MPI-OM_GR1.5L40 SRESA1B run no.1: atmosphere 6 HOUR values MPImet/MaD Germany. World Data Center for Climate. Available at: http://dx.doi.org/10.1594/WDCC/EH5-T63L31_OM-GR1.5L40_A1B_1_6H. doi:10.1594/WDCC/EH5-T63L31_OM-GR1.5L40_A1B_1_6H

Roeckner E, Lautenschlager M, Schneider H (2006b) IPCC-AR4 MPI-ECHAM5_T63L31 MPI-OM_GR1.5L40 SRESA1B run no.2: atmosphere 6 HOUR values MPImet/MaD Germany. World Data Center for Climate. Available at: http://dx.doi.org/10.1594/WDCC/EH5-T63L31_OM-GR1.5L40_A1B_2_6H. doi:10.1594/WDCC/EH5-T63L31_OM-GR1.5L40_A1B_2_6H

Roeckner E, Lautenschlager M, Schneider H (2006c) IPCC-AR4 MPI-ECHAM5_T63L31 MPI-OM_GR1.5L40 SRESA1B run no.3: atmosphere 6 HOUR values MPImet/MaD Germany. World Data Center for Climate. Available at: http://dx.doi.org/10.1594/WDCC/EH5-T63L31_OM-GR1.5L40_A1B_3_6H. doi:10.1594/WDCC/EH5-T63L31_OM-GR1.5L40_A1B_3_6H

Roeckner E, Lautenschlager M, Schneider H (2006d) IPCC-AR4 MPI-ECHAM5_T63L31 MPI-OM_GR1.5L40 SRESA2 run no.1: atmosphere 6 HOUR values MPImet/MaD Germany. World Data Center for Climate. Available at: http://dx.doi.org/10.1594/WDCC/EH5-T63L31_OM-GR1.5L40_A2_1_6H. doi:10.1594/WDCC/EH5-T63L31_OM-GR1.5L40_A2_1_6H

Roeckner E, Lautenschlager M, Schneider H (2006e) IPCC-AR4 MPI-ECHAM5_T63L31 MPI-OM_GR1.5L40 SRESB1 run no.1: atmosphere 6 HOUR values MPImet/MaD Germany. World Data Center for Climate. Available at: http://dx.doi.org/10.1594/WDCC/EH5-T63L31_OM-GR1.5L40_B1_1_6H. doi:10.1594/WDCC/EH5-T63L31_OM-GR1.5L40_B1_1_6H

Roeckner E, Lautenschlager M, Schneider H (2006f) IPCC-AR4 MPI-ECHAM5_T63L31 MPI-OM_GR1.5L40 20C3M run no.1: atmosphere 6 HOUR values MPImet/MaD Germany. World Data

Center for Climate. Available at:
http://dx.doi.org/10.1594/WDCC/EH5-T63L31_OM-GR1.5L40_20C_1_6H.
doi:10.1594/WDCC/EH5-T63L31_OM-GR1.5L40_20C_1_6H

Shapiro MA, Fedor LS, Hampel T (1987) Research aircraft measurements of a polar low over the Norwegian Sea. *Tellus* 39A: 272–306

Singh CV (2004) Empirical Orthogonal Function (EOF) analysis of monsoon rainfall and satellite-observed outgoing long-wave radiation for Indian monsoon: a comparative study. *Meteor. Atmos. Phys.* 85: 227–234

Steppeler J, Doms G, Schättler U, et al. (2003) Meso-gamma scale forecasts using the nonhydrostatic model LM. *Meteorology and Atmospheric Physics* 82: 75–96. doi:10.1007/s00703-001-0592-9

Stocker TF, Schmittner A (1997) Influence of CO₂ emission rates on the stability of the thermohaline circulation. *Nature* 388: 862–865

van Engelen VWP, Wen TT (1995) Global and national soils and terrain digital database (STORE). *World Soil Resources Report No. 74 Rev. 1.*, Rome, p 138

von Storch H, Bruns T, Fischer-Bruns I, Hasselmann KF (1988) Principal oscillation pattern analysis of the 30-to 60-day oscillation in general circulation model equatorial troposphere. *J. Geophys. Res.* 93: 11022–11036

von Storch H, Langenberg H, Feser F (2000) A Spectral Nudging Technique for Dynamical Downscaling Purposes. *Monthly Weather Review* 128: 3664–3673

von Storch H, Zwiers FW (1999) *Statistical analysis in Climate Research*. Cambridge University Press

Waldron KM, Peagle J, Horel JD (1996) Sensitivity of a spectrally filtered and nudged limited area model to outer model options. *Mon. Wea. Rev.* 124: 529–547

Wallace JM, Gutzler DS (1981) Teleconnections in the geopotential height field during the Northern Hemisphere winter. *Mon. Wea. Rev.* 109: 784–812

Weare BC, Navato AR, Newell RE (1976) Empirical Orthogonal Analysis of Pacific Sea Surface Temperature. *Journal of Physical Oceanography* 6: 671–678

Wolter K, Timlin MS (2011) El Niño/Southern Oscillation behaviour since 1871 as diagnosed in an extended multivariate ENSO index (MEI.ext). *Int. J. Climatology* 31: 1074–1087

Wright PB (1985) The Southern Oscillation - An ocean-atmosphere feedback system. *Bull. Amer.*

Meteor. Soc. 66: 398–412

Wu LT, Petty GW (2010) Intercomparison of Bulk Microphysics Schemes in Model Simulations of Polar Lows. *Monthly Weather Review* 138: 2211–2228. doi:10.1175/2010MWR3122.1

Xia X, Zahn M, Hodges K, Feser F, von Storch H (2012) A Comparison of Two Identification and Tracking Methods for Polar Lows. *Tellus A* 64: 17196. doi:10.3402/tellusa.v64i0.17196

Yanase W, Fu G, Niino H, Kato T (2004) A polar low over the Japan Sea on 21 January 1997. Part II: A numerical study. *Monthly Weather Review* 132: 1552–1574

Yanase W, Niino H (2007) Dependence of polar low development on baroclinicity and physical processes: An idealized high-resolution numerical experiment. *Journal of the Atmospheric Sciences* 64: 3044–3067. doi:10.1175/JAS4001.1

Yarnal B, Henderson KG (1989a) A Satellite-derived Climatology of Polar-low Evolution In the North-pacific. *International Journal of Climatology* 9: 551–566

Yarnal B, Henderson KG (1989b) A Climatology of Polar Low Cyclogenetic Regions Over the North Pacific-ocean. *Journal of Climate* 2: 1476–1491

Yonetani T, Gordon HB (2001) Simulated Changes in the Frequency of Extremes and Regional Features of Seasonal/Annual Temperature and Precipitation when Atmospheric CO₂ Is Doubled. *Journal Of Climate* 14: 1765–1779. doi:10.1175/1520-0442(2001)014<1765:SCITFO>2.0.CO;2

Zahn M, von Storch H (2008a) A long-term climatology of North Atlantic polar lows. *Geophysical Research Letters* 35. doi:10.1029/2008GL035769

Zahn M, von Storch H (2008b) Tracking Polar Lows in CLM. *Meteorologische Zeitschrift* 17: 445–453. doi:10.1127/0941-2948/2008/0317

Zahn M, von Storch H (2010) Decreased frequency of North Atlantic polar lows associated with future climate warming. *Nature* 467: 309–312. doi:10.1038/nature09388

Zhang Y, Wallace JM, Battisti DS (1997) ENSO-like interdecadal variability: 1900-93. *Journal of Climate* 10: 1004–1020

Zubler EM, Lohmann U, Lüthi D, Schär C, Muhlbauer A (2011) Statistical Analysis of Aerosol Effects on Simulated Mixed-Phase Clouds and precipitation in the Alps. *J. Atmos. Sci.* 68: 1474–1492. doi:10.1175/2011JAS3632.1

Erklärung

Hiermit erkläre ich an Eides statt, dass ich die vorliegende Dissertationsschrift selbst Verfasst und keine anderen als die angegebenen Quellen und Hilfsmittel benutzt habe.

Ort, Datum

Unterschrift